Friction Surfacing of Titanium Grade 1 and Ti-6Al-4V

Vom Promotionsausschuss der
Technischen Universität Hamburg-Harburg

zur Erlangung des akademischen Grades

Doktor-Ingenieurin (Dr.-Ing.)

genehmigte Dissertation

von
Viktoria Fitseva

aus
Naltchik

2016

Gutachter:

Prof. Dr.-Ing. Norbert Huber

Prof. Dr.-Ing. Alfons Fischer

Vorsitzender des Prüfungsausschusses:

Prof. Dr. habil. Michael Morlock

Tag der mündlichen Prüfung:

05. Dezember 2016

Kurzfassung

Das Reibauftragschweißverfahren ist eine relativ neue und vielversprechende Technologie zur Oberflächenmodifikation technischer Komponenten. Hierbei können Beschichtungen zur lokalen Eigenschaftsänderung oder zu Reparaturzwecken erzeugt werden. Das Hauptmerkmal dieses Verfahrens, im Vergleich zu konventionellen Beschichtungsmethoden, ist, dass die Schichten in der Festphase aufgetragen werden. Durch die eingebrachte massive plastische Verformung des Werkstoffes ändert sich die Mikrostruktur und es entsteht ein vollständig rekristallisiertes Gefüge. Die Korngröße der entstandenen Schichten ist im Regelfall kleiner als die des Ausgangsmaterials, was zu verbesserten mechanischen Eigenschaften führt. Weil das Reibauftragschweißen ein relativ neues Verfahren ist, sind einige der möglichen Materialkombinationen in artgleichen und artfremden Paarungen noch unerforscht. Aufgrund dessen, dass Titanlegierungen als Ausgangswerkstoff kostspielig sind, sind neue Technologien, welche die Produktionskosten reduzieren können, von großem Interesse. Mit dem Reibauftragschweißen bietet sich ein Beschichtungsverfahren an, welches auch modernen Ansprüchen an die Umweltverträglichkeit gerecht wird.

Das Ziel der vorliegenden Arbeit war es, Schichten aus Titanlegierungen mittels Reibauftragschweißen aufzutragen. Dafür wurde die Prozessentwicklung für die Werkstoffe Ti-6Al-4V und Ti-Gr.1 realisiert. Titanlegierungen weisen ein komplexes Umformverhalten bei hohen Temperaturen auf, insbesondere, wenn sie sowohl den alpha-beta-, als auch den beta-Phasenbereich beim Umformen durchlaufen. Hierbei sind Dehnratenempfindlichkeit und Fließinstabilität charakteristisch für Titanlegierungen, was die Verarbeitung beim Reibauftragschweißen erschweren kann. Diese Schwierigkeiten wurden durch die systematische Erarbeitung geeigneter Prozessparameter und einer zielführenden Prozesssteuerung überwunden. Es wurde ein breites Parameterfenster etabliert, innerhalb dessen zwei verschiedene Regimes der Drehzahlen gefunden wurden, zwischen denen sich das Materialverhalten deutlich unterscheidet. Das niedrige Drehzahl-Regime weist dabei Veränderungen in der Prozesstemperatur auf, welche die Fließeigenschaften des Werkstoffs beeinflussen, was wiederum zu einer Wulstbildung an den Schichten führt. Die Mikrostruktur in diesem Regime offenbart feine, dynamisch rekristallisierte Körner. Dazu gegensätzlich weist das hohe Drehzahl-Regime eine höhere resultierende Temperatur auf, die in diesem Bereich nicht variiert. Die konstante Temperatur führt zu einem stabilen Materialfließverhalten und ermöglicht damit eine dementsprechend wulstfreie Realisierung von Schichten. Allerdings führen diese hohen Temperaturen zu einem Anstieg in der Korngröße. Die in Bezug auf die Korngröße unterschiedlich entwickelte Mikrostruktur zeigte keinen Einfluss auf das Schwingungsverschleißverhalten der Schichten. Die Verschleißeigenschaften der Schichten und des Grundwerkstoffs erwiesen sich als vergleichbar. Im Zuge von Mikroflachzug-Tests offenbarten die Schichten eine erhöhte Festigkeit mit leichten Einbußen in der Duktilität, was ein charakteristisches Verhalten für dynamisch rekristallisierte Werkstoffe bei Vorhandensein von Restverformung ist. Somit konnte gezeigt werden, dass das Reibauftragschweißen als Reparaturmethode für Titan-Bauteile, grundsätzlich in Betracht gezogen werden kann.

Abstract

The friction surfacing process is a relatively novel and promising surface modification technology, by which coatings can be deposited as a protection or surface repair method. The main feature of this process, compared with other technologies, is that the coatings are deposited in solid state phase. Therefore, the induced massive deformation alters the initial microstructure of the materials, resulting in a fully recrystallised microstructure of the coatings. Typically, the grain size of the coating is smaller than that of the raw material, which leads to improved mechanical properties. Since the process is a relatively new technology, several possible material combinations in similar or dissimilar configurations are unexplored. Titanium alloys are rather expensive. Therefore, new technologies are required to keep the production cost at an acceptable level and offer an additional cladding process that is environmental friendly.

The aim of the current work was to deposit coatings from the titanium alloys by friction surfacing. Process development for Ti-6Al-4V alloy and Ti-Gr.1 as coating materials to be deposited by friction surfacing was carried out. At high temperatures titanium alloys exhibit complex deformation behaviour, particularly when passing through the alpha-beta phase transformation and in the beta phase state. Strain rate sensitivity and flow instabilities are characteristics of Ti-based materials that may hinder the deposition process. These difficulties were overcome by the selection of an adequate process control method and a systematic choice of process parameter combinations. A broad range of parameter sets for titanium depositions has been established, whereby two different acting rotational speed regimes were observed. The low rotational speed regime revealed variations in the process temperature, which influenced the material flow behaviour leading to flash generation at the coating. The microstructure in this regime consists of refined dynamically recrystallised grains. In contrast, the high rotational speed regime revealed a higher resulting temperature, which did not vary in this range. This constant temperature led to stable material flow behaviour and flash-free coatings were deposited. However, the high temperature influenced the grain size of the coatings resulting in coarse grains. Still, these differences in the grain size did not influence the fretting wear behaviour of the coatings. The investigation of fretting wear experiments exposed a similar behaviour of friction surfacing coatings and the base material. In micro tensile tests the coatings exhibited an increase in strength but a decrease in ductility, which is typical for dynamically recrystallised materials, which contain residual deformation. Therefore, it could be shown that friction surfacing can be considered as a repair method for titanium parts.

IV

Contents

Abbreviations

ARB	Accumulative roll bonding
AS	Advancing side
bcc	Body-centred cubic
CM	Confocal microscope
CP	Commercially pure
CRC	Consumption rate control
DRX	Dynamic recrystallisation
EBSD	Electron backscatter diffraction
ECAP	Equal-channel angular pressing
EDM	Electro discharge machining
EDS	Energy-dispersive spectroscopy
EI	Energy input
FS	Friction surfacing
FSW	Friction stir welding
GMAW	Gas metal arc welding
HAZ	Heat-affected zone
HPT	High-pressure torsion
IPF	Inverse pole figure
IR	Infrared camera
MAF	Multi-axial forging
OM	Optical microscope
RS	Retreating side
SEM	Scanning electron microscope
SPD	Severe plastic deformation
SRX	Static recrystallisation
TE	Twist extrusion
TEM	Transmission electron microscope
TIG	Tungsten inert gas

1 Introduction

The investigation of efficient new technologies, that are cost effective and can save resources such as energy and materials, is an urgent challenge in current research efforts worldwide. Friction surfacing (FS) is one such promising technology. As this work will demonstrate, it offers interesting options for various applications and work areas including the medical and aircraft industries. The history of the FS process began in 1941, when it was first patented by Klopstock and Neelands [1]. The technology was then lost for many years until a Russian engineer rediscovered it in 1950. In 1986, the literature finally reported the frequent use of the FS process [2]. Nowadays, FS is becoming more relevant, especially for the surface modification of structural materials [3, 4].

The use of the FS process can be seen as a prevention method to increase the service-life and functional safety of parts by surface modification. Furthermore, the process can be used as a local repair technique with the economic advantage of avoiding the exchange of all prefabricated parts and thus increasing the long-term service-life. Here, the deposition of titanium coatings by FS can be highly promising because it may be used for applications in the aircraft such as turbine blades. Currently, FS is being used by the British Company Frictec Ltd. to modify surfaces of cutting tools for the packing industry [5].

FS technology is known as a deposition process for metallic materials based on thermo-mechanical mechanisms. The process pressure, in combination with severe plastic deformation and high shear strains, allows the materials to experience high temperatures without reaching their liquid phase and form a microstructure with recrystallised refined grains. Additionally, FS may be used to deposit difficult to weld materials or to join dissimilar material combinations that are not easy to join by a conventional process. However, the FS process, as a young and barely examined technique, is still in its infancy. Currently, only a few companies are using FS technique due to the lack of a fundamental understanding of the process and the materials that can be used for deposition. Much work has been published to enumerate the necessity of the FS process, but only little work has been performed to understand the material behaviour within a broad range of process parameters and coating formation. Early papers reported the successful deposition of materials such as steels and aluminium alloys [6, 7]. Despite of the fact that these materials can be deposited successfully by FS, a thorough understanding of this technology is still missing. Previous publications demonstrated the relevance of the process; however findings of possible boundaries of the process and the entire spectrum of resulting mechanical properties are inadequately researched [8]. Generally, due to the different material characteristics and their deformation behaviour, the implementation of the FS process for each new material is complex and must be investigated thoroughly.

Since the first development of titanium and its alloys in 1940, they have offered an alternative to long-used materials such as steel, aluminium and nickel super alloys [9]. Due to the fact that titanium alloys are rather expensive, new technologies are required to keep the production costs at an acceptable level.

Because Ti-6Al-4V and Ti-Gr.1 are being used in the aircraft industry and in the medical field for hip joint replacements, the necessity to provide new technologies for this area of application is increasing. A feasibility study was published as an attempt to deposit titanium onto various substrates (Al, Cu, Inconel, Mg and Ti) and concluded that titanium could not be deposited onto any of these substrates [10]. The process parameters applied during those unsuccessful deposition trials have not been published. From the scientific point of view, no specific reasons for the failure of deposition of titanium alloys have been discussed in the literature. Because titanium alloys could not be deposited by FS, a knowledge gap regarding the needed process employment for coating deposition exists. Hence, neither the process employment nor the metallurgical behaviour is described, and the resulting mechanical properties are unknown. Furthermore, the analysis of titanium behaviour at high strain rates and temperatures as present during FS is also unexplored. In the scope of this thesis two different titanium alloys (Ti-Gr.1 and Ti-6Al-4V) were chosen in order to additionally investigate how the mechanical properties and alloying elements of the consumable materials may influence the process.

In this chapter, a brief introduction and motivation of the current work were presented. The aim of this work is portrayed in chapter 2. The state of the art, chapter 3 of this thesis, deals with the materials and their deformation behaviour, conventional deposition processes as well as the friction surfacing process. In chapter 4 the experimental equipment and materials are presented, covering the investigation methods such as temperature analysis, heat treatment via dilatometer and mechanical testing. Results and discussion of process development, microstructural analysis as well as mechanical characterisation are presented in chapter 5. In the next chapter 6 the conclusions of the current work are presented.

2   The Aim of this Work

One major subject of this work is to clarify the material properties that cause the difficulties in friction surfacing of titanium alloys. Titanium alloys are susceptible to flow instabilities during severe plastic deformation. This attribute is an important factor in material processing by plastic deformation, which must be considered during friction surfacing development. Furthermore, a process study in a wide range of parameters is part of this work to understand material flow, coating dimensions and microstructural development. Titanium alloy coatings deposited by other techniques have revealed insufficient mechanical properties, including low ductility and poor fretting wear behavior [11, 12]. Therefore, an investigation of the mechanical properties of the material deposited by FS is carried out to achieve a comprehensive understanding of the coating properties, which is essential to offer FS as a possible repair technology for components made of titanium alloys.

The objectives of the current work concentrate on technological and scientific subjects as presented in the following:

- Development of the process management strategy to deposit reproducible and high-quality coatings of different titanium alloys.
- Control of coating properties based on the process parameters.
- Analysis of the interaction of process parameters with the microstructural development and mechanical behaviour of the coatings.
- Investigation of high-temperature, high-strain rate behaviour of titanium during friction surfacing.
- Investigation of the microstructure evolution during the fast thermal cycle with and without severe plastic deformation.
- Presenting an alternative technology for the future for the generation of titanium coatings by friction surfacing.

3 State of the Art

The following chapter will give an overview of the material properties of titanium used in the current study. In addition, an overview over other conventional deposition techniques for surface repair or damage prevention will be given. One section will address the FS technique, noting the process benefits and limitations and presenting materials that currently can be deposited by the process.

3.1 Titanium Alloys

After aluminium, iron and magnesium, titanium is the fourth most abundant metal in the crust of the earth. Titanium can be extracted from rutile TiO_2 or ilmenite $FeTiO_3$. In 1791 Gregor first discovered an element that was unknown during that time in dark-coloured magnetic iron sand. Four years later in 1795, a similar finding was made by a German chemist while evaluating a rutile, an oxide of unknown element, which he named "Titanium" [9]. Many years later, between 1937 and 1940, an appropriate process for titanium production was discovered by Kroll in Luxemburg, which was subsequently developed and established and is still being used. The Kroll process is based on the reduction of titanium from tetrachloride with magnesium under inert gas. The resulting product is called a "Titanium sponge" because of its spongy and poriferous appearance. The use of inert gas atmosphere during titanium production increases its price. Due to the high price of titanium, it is only chosen for certain areas of applications [9].

Titanium exhibits a beneficial ratio between strength and density. Furthermore, the high affinity to oxygen leads to the formation of a stable passive film at the surface, which is responsible for its high corrosion resistance against many organic acids and sea water [13].

Titanium alloys are allotropic materials. This allotropy is defined by the phase transformation from the body-centred cubic (β-phase) at high temperatures to the hexagonal close packing (α-phase) at low temperatures. This transformation temperature, better known as the β-transus temperature, depends on the content of the substitutional and interstitial alloying elements and their purity.

Titanium alloys can be divided into alpha alloys with a hexagonal lattice, dual phase α + β alloys with hexagonal and bcc lattices and beta alloys with bcc lattices at room temperature. Alloys that possess a single alpha phase are characterised by their good strength and high oxygen solute resistance with a loss in ductility. In contrast, alloys with a beta phase have far better formability and high cold and warm strength values, but at the same time, they have a high susceptibility to oxygen embrittlement. Moreover, the specific density-to-strength ratio is disadvantageous compared with alpha phase alloys. Dual-phase alloys present a compromise

between good formability and high cold strength values [9]. Because of their high strength-to-density ratio, titanium alloys are widely utilised in structural components in the aircraft industry. The main area of titanium application is in power plants. Primarily, titanium alloys were used for compressor blades and later for compressor discs. Because fan blades and discs are employed exclusively at low temperatures, these components are produced from Ti-6Al-4V alloys. Due to the oxidation behaviour of titanium, the maximum application temperature of these alloys is 315 °C. Therefore, titanium alloys are suitable for the components (blades and discs) of the low-pressure turbine in the first four to five line [9]. Because of the good corrosion resistance of titanium, its application area as a biomaterial is well known [14]. It is mostly used for implants. Moreover, it has been reported that titanium ensures superior bio-adhesion (osseointegration) possibility compared with stainless steel [9].

3.1.1   Commercially Pure (CP) Titanium and Alpha Alloys

The alpha alloys exhibit a hexagonal allotropic structure at room temperature. This structure transforms at the temperature of 882.5 °C into a body-centred cubic β phase that remains stable up to the melting temperature of 1675 °C. The transformation from the α to β phase at high temperatures is reversible and cannot be frozen by quenching [15]. To stabilise the alpha phase at high temperatures, soluble elements in the hexagonal alpha structure such as Al and Sn (substitutional elements) or O, N and C (interstitial elements), can be alloyed.

The processing of the alpha alloys includes the creation of the desired dimensions and the control of the grain size and crystallographic texture. These alloys contain only small quantities of alloying elements, contributing to good weldability. After processing, the microstructure always contains recrystallised alpha grains and a dispersed beta phase. The beta phase is always present in all alpha alloys and is related to the marginal amount of Fe within all CP titanium alloys. As mentioned earlier, the Fe barely dissolves in the alpha phase, either during solidification or cooling, and thus remains as a beta phase element. All CP titanium grades contain a certain amount of Fe, which increases with the grade number. The presence of Fe is required because the beta phase can stabilise the alpha grain boundaries and thereby control the grain size during recrystallisation. A microstructure with an intermediate grain size improves the formability of the alloys by allowing more extensive twinning. A microstructure with a small grain size is required to increase the yield strength, as described by the Hall-Petch relationship, when higher strength is preferred. During the continued annealing after recrystallisation, grain growth can occur, but the beta phase reduces the grain growth rate, enabling a structure with a reproducible grain size to be achieved. Therefore, CP titanium with a low Fe content (0.03 %) can undergo secondary alpha grain growth after an annealing treatment, in contrast to that with a higher (0.15 %) Fe content. Furthermore, Fe as a beta phase stabiliser has high solubility for hydrogen, so its presence enhances the hydrogen tolerance for CP titanium alloys. This is important due to the possibility of hydrogen

absorption, especially because the main applications of this group of alloys are in corrosive environments [13].

The properties of titanium alloys are affected by the addition of elements such as oxygen and the processing route, which constitutes the grain size and preferred texture. The yield strength of the CP titanium from grades 1 through 4 is affected by an increasing oxygen concentration with increasing grade number from 0.18 % (grade 1) to 0.40 % (grade 4) because oxygen is a solid solution strengthening agent of the alpha phase. The combination of both oxygen and iron has a major effect on the strength of the final components in this class of alloys [13].

3.1.2 Alpha-Beta Alloys

The alpha and beta alloys exhibit a dual hexagonal and body-centred cubic microstructure at room temperature. This structure completely transforms into body-centred cubic lattices when transcending a temperature of 995 °C and remains stable under a further increase in temperature.

The $\alpha+\beta$ alloys contain both the alpha and beta stabilising elements, although in different concentrations of the solute atoms. The following elements are known as alpha phase stabilisers: Al, O, N, and C; at the same time, these elements increase the beta transformation temperature while increasing their solute content. The beta phase stabilising elements are grouped into two categories: β isomorphous elements, including V, Mo and Nb and the mainly used β eutectoid elements, including Cr, Fe and Si. A sufficient concentration of these solute atoms can stabilise the β phase at room temperature [13].

The transformation of the alpha-beta alloys from the bcc beta phase into the hexagonal alpha phase can occur by martensitic transformation or by the diffusion and growth process, depending on the alloy composition and cooling rates during the processing route. The crystallographic orientation relationship between alpha and beta was first studied for zirconium by Burgers and was titled the "Burgers relationship". Subsequently, the Burgers relationship has been confirmed for titanium alloys as well. This Burgers relationship was obtained for both martensitic transformation and the nucleation and growth processes. According to this Burgers orientation relationship, a bcc crystal can transform into 12 hexagonal variations with different orientations with respect to the parent beta crystal [13].

The cooling rate is a decisive point for microstructure development by heat treatment. Cooling rates below 2 Ks^{-1} lead to diffusion controlled nucleation and growth of stable α and β phases. These phases occur in the shape of colonies of α-phase lamellae within the primary β-phase grains [16].

The martensitic transformation involves a coactive movement of the atoms, resulting in a homogeneous transformation of the bcc high-temperature phase into the hcp crystal lattice. Martensitic transformation is governed by the atom movement by a shear deformation, resulting in a transformation from the bcc into the hexagonal α' crystal lattice or into the orthorhombic α'' structure [13, 16]. The hexagonal structure of the α' martensite becomes distorted with increasing solute content and hence loses its symmetry and must be described as an α'' orthorhombic structure. The hexagonal martensite α' can exist in two morphologies: as massive martensite or acicular martensite. Both martensitic plates contain high dislocation density and occasional twins. The first occurs in pure titanium, dilute alloys and alloys with a high martensitic transformation temperature. The massive martensite consists of large, irregular areas (50 μm - 100 μm), which contain parallel α' plates or laths with a thickness of around 0.5 μm – 1 μm, having identical variants of the Burgers relationship. Correspondingly, acicular martensite occurs in the alloys with low martensitic transformation temperature. The acicular martensite consists of individual α' plates which have different variants of Burgers relationship. The orthorhombic α'' martensite forms a modulated microstructure derived from a spinodal decomposition in solute-lean α'' and solute-rich α'' regions. Eventually, the beta phase precipitates according to α_{lean}''+ α_{rich}'' → α+β [13].

3.1.3 Beta Alloys

The most important difference between beta alloys and α-β is that the beta alloys can reach considerably higher yield strengths than the dual-phase alloys. Furthermore, the beta alloys do not transform martensitic while quenching. The β alloys, depending on the amount of β stabilising elements, can be retained in their metastable form under high cooling rates to room temperature, so no substantial precipitation of the α phase occurs while cooling. In that state, the alloys can be easily deformed at low processing temperatures compared with the dual-phase alloys. Depending on the alloy, the corrosion resistance is similar or even better than the corrosion resistance of dual-phase alloys [13].

The microstructure of the beta alloys can be divided into three different categories depending on the processing route: beta annealed microstructure, necklace microstructure ("through-transus" deformation process) and bimodal structure. To obtain the beta annealed microstructure, the recrystallisation should occur in the beta phase field, and the aging should occur in the α+β phase, precipitating the α phase in the form of fine α platelets. By creating a necklace microstructure, a "through-transus" deformation process must be applied. After the homogenisation, the material is continuously deformed from the β phase field to the α+β phase until achieving the formation of α as round particles at the deformed β grain boundaries. The processing route for the creation of the bimodal microstructure eventually differs compared with the first one. The deformation step is obtained below the transus temperature. The characteristic for the bimodal structure is that the alpha layers at the beta

grain boundaries can be compensated by creating a small beta grain size. In this case, the alpha layers have a negligible negative effect on the mechanical properties [13].

3.1.4 Flow Stress Instability during Plastic Deformation

Titanium alloys tend to have flow instabilities during plastic deformation because of their sensitivity to temperature and strain rate. An increase in strain rate raises the flow stress, and a rise in temperature substantially degrades the flow stress. The combination of deformation and temperature has a significant effect on the material behaviour. When metals undergo severe plastic deformation, roughly 95 % of the plastic power is converted into heat almost instantly [17, 18]. This prompt conversion of the dissipated energy causes a temperature increase, and the material softens. At high temperatures and high strain rates, thermal softening may weaken the stabilising effect of work hardening and may cause material instabilities. Several processing maps created by hot compression experiments with correlation of temperature and strain with regard to dissipation power are reported in the literature [17, 18]. The processing maps predict regimes of flow instability at various strain rates and temperatures. These flow instabilities are attributed to microstructural features observed at the corresponding range of processing. The microstructure exhibits flow localisation bands at an angle of 45° to the compression axis. The occurrence of these bands is attributed to an adiabatic condition in the material at high temperatures and deformation derived from the low thermal conductivity of titanium. These flow instabilities have been observed in the α-β regime and in the β regime [17-21].

3.2 Conventional Deposition Processes

Because of their high affinity to oxygen, titanium materials must be deposited in an inert gas atmosphere to prevent embrittlement. Basically, pure titanium can be welded more easily compared with the titanium alloys. The weldability depends on the phase composition. In terms of this relation, α alloys are more easily weldable than α+β alloys. Generally, titanium alloys exhibit lower ductility and toughness in a post-deposited condition [9].

Besides friction surfacing, the cladding processes include laser cladding, brazing, diffusion bonding, explosive cladding, spray deposition via osprey and electro-spark deposition [3].

To repair or modify surfaces locally with regard to wear or corrosion resistance, different methods, such as laser cladding or explosive cladding, can be used for different metallic depositions. As the name suggests, the laser cladding process utilises a laser to generate a melt pool of the filler material and the surface of the base material. The filler material induced in the process might be either powder or wire. Laser cladding is generally performed with CO_2, Nd:YAG (neodymium-doped yttrium aluminium garnet), and, recently diode lasers as the fibre [3, 22]. However, this technique features high costs for filler material and gas consumption [23].

Explosion cladding is a solid-state process that ensures a bonding of two or more materials based on explosive detonation forces at high pressures. A high-velocity jet is formed between two metal plates during the achievement of high velocities if the collision angle and collision velocity are in the required bonding range. The process is well applicable to large areas. Because of the explosive detonations employed during the process, this technique is not environmentally friendly [3, 22].

Moreover, titanium depositions can be realised by the cold spraying process and laser metal deposition process. Below, these processes are introduced briefly:

The cold spraying process is a deposition process, in which particles as consumable materials are accelerated and hit the substrate at high velocities. Thus, coatings with high deposition efficiency and a nano-sized structured can be produced [24]. By this process, particles are injected into a high-speed gas jet in the nozzle and accelerated to velocities in the range of 300 – 1200 m/s. The deposition of coatings occurs at temperatures below their melting range. However, the titanium coatings exhibit a porous structure with a porosity up to 22.3 ± 4.7 % depending on the alloy [25]. Therefore, the coatings are heat-pressure treated by hot isostatic pressing. The disadvantages of the process include that not all substrate materials can be coated because high gas flow and consumption is involved, and helium gas is expensive.

Laser metal deposition is used as a repair technology. This technique produces low distortion and low thermal damage in the base material due to the low heat input vis-à-vis TIG and gas metal arc welding [26]. This technique generates coatings in the melting temperature range of the materials. A powder filler material can be deposited onto the repairable part. A high-power laser equipped with shielding gas is used to heat and melt the metal powder, which solidifies on the part, forming a fully dense coating. With the addition of multiple layers, a three-dimensional structure can be built [27, 28]. The energy consumption of the high-power laser may incur high costs. Furthermore, the deposit zone indicates grain growth governed by the heterogeneous nucleation [27]. The deposits affect the substrate enormously, leading to grain coarsening.

3.3 Friction Surfacing Process

As a solid-state process, the friction surfacing is used to deposit layers at process temperatures below the melting range of the coating material, and it allows the deposition of metallurgically incompatible materials. The process involves a rotating, consumable metal rod that is applied onto a substrate under an axial load. The relative motion between the rod and the substrate results in frictional heat generated at the interface that plasticises the rod tip. The plasticised rod material is then deposited onto the substrate as it traverses along the machine platform with excessive softened material ascending around the rod forming a flash. For better understanding, Figure 3.1 shows the process divided into four distinct steps. In the first

step, the consumable rod is positioned at the process initiation site (a). In the next stage, the consumable rod is brought to the defined rotational speed and axial force. Due to the pressure and rotation, frictional heat is generated, and a certain amount of material plasticises at the tip of the rod (b). Once the desired plastification of the rod is achieved, the table traverses underneath the rod, which leaves deposited material behind on the substrate (c). Once the desired end position of the coating is reached, the consumable rod moves up out of contact, thus avoiding being welded onto the substrate (d). The edge of the layer at which the direction of the rotational speed is the same as the deposition direction is denominated as the advancing side (AS), and the edge at which the rotational velocity vector is opposite to the deposition direction is defined as the retreating side (RS). During the initial dynamic contact between the consumable rod and the substrate, the relative motion governed by the axial force produces a scouring action that removes the oxide layer from both contact surfaces [29]. The severe plastic shear deformation and the thermal cycle imposed by the process alter the original microstructure of the consumable rod, leading to recrystallisation, grain refinement and, depending on the processed material, phase transitions [30]. The impact on the substrate is limited compared with the fusion welding processes because of the comparably low heat input [31-33]. The parameters with the strongest impact on the FS process are the deposition speed, the rotational speed of the consumable rod and the axial load. Further relevant factors include the diameter of the consumable rod, the thermal conductivity of the substrate and the joint configuration i.e., either similar or dissimilar. The coating thickness, width and bond quality depend on all of these parameters [34-36].

3.3.1 Materials Deposited by Friction Surfacing

As mentioned previously, some metallic materials that are considered as difficult to weld can be deposited by FS. Materials such as steels, aluminium and magnesium alloys and NiAl bronze were deposited successfully by FS in both similar or dissimilar configurations [4, 37].

Rafi et al. reported on the microstructure of AISI H13 tool steel coatings, which were deposited onto a low-carbon steel substrate. The coatings revealed a refined martensitic microstructure. Due to the high cooling rates, the carbide precipitation was suppressed, and a martensitic structure was formed, causing an increase in hardness [34].

The deposition of several aluminium alloys has been widely discussed by numerous authors, who have noted the presence of the dynamically recrystallised microstructure of the coating. A grain refinement of around 33 % compared with the base material of AA 6082 coatings over an AA 2024 substrate has been observed and reported by Gandra et al. [38]. No increase in hardness could be observed, in this combination. The temperature measurement of AA 5052 coatings during the process has been reported to be around 527 °C. In addition, grain refinement in the microstructure has been observed [7].
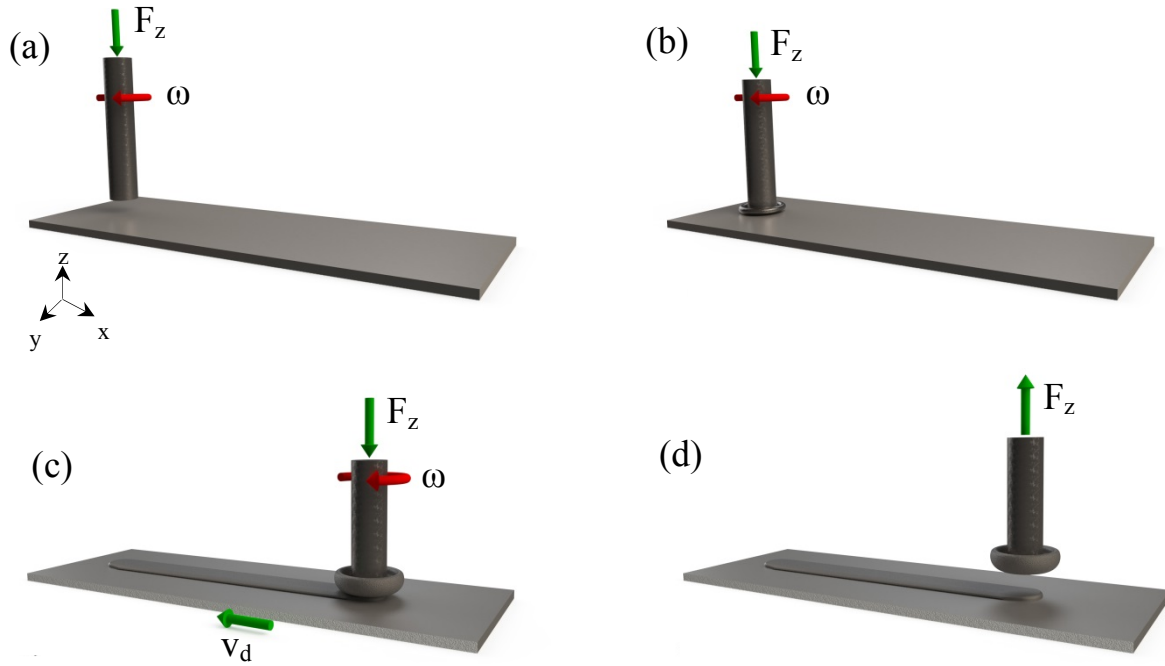
Figure 3.1: Schematic of FS process described in four steps. (a) Positioning of the consumable rod, (b) plastification phase under axial load and rotational speed, (c) coating deposited onto the substrate, (d) lift up of the rod.

Dissimilar magnesium alloys in a configuration of AZ 91 as a consumable rod material were deposited onto an AZ 31 substrate [39]. The coatings were not deposited continuously, and the microstructure at the regions where the coating could be deposited onto the substrate was analysed. The microstructure of the coatings showed refined recrystallised grains resulting in increased hardness and wear resistance as well. The temperature during the experiment was measured as 265 °C.

The Cr60Ni40 alloy is known as an unweldable and non-deformable alloy. The feasibility of depositing Cr60Ni40 alloy onto a Nimonic 80A substrate by FS was reported by Hanke et al. [30]. The microstructure and cavitation erosion behaviour of the coatings was analysed. The coatings presented a phase with the Cr:Ni ratio of the eutectic (52:48). An austenitic fcc lattice of the Ni-rich phase and a high volume fraction of fine precipitates within the Cr-rich constituent were observed. Furthermore, the coatings exhibited one-third the wear rate under cavitation compared with the cast and heat-treated samples because the Cr-rich phase became abundant via the FS process [30].

3.3.2 Process Benefits and Limitations

The FS process is a promising technology for depositing materials that cannot be deposited by conventional fusion welding processes. One of the disadvantages is that the coating geometry (width and thickness) can be contingently controlled only by the process parameters and is

limited due to the restricted diameter of the consumable rod. Voutchkov et al. reported, based on the materials investigated so far, that the coating thickness may lie in the range of 0.2 mm to 3 mm depending on the material [40]. To overcome the width and thickness limitations, several coatings can be deposited in juxtaposition with each other (multi-coating) for increased width or overlapping coatings can be deposited for increased thickness. However, both configurations overlapping and several coating tracks may modify the microstructure of the previously generated deposits and lead to further effect due to the heat generated. With regard to the coating geometry, the maximum integrated length of the deposit is limited by the consumable rod length. The excessive material that forms around the rod tip while depositing must be trimmed by flash cutters to generate long coatings. Otherwise, the excessive material may block the feeding. Furthermore, the flash formed at the rod can be seen as wasted material because it cannot be used for further depositions and must be removed before further use. This drastically affects the deposition efficiency. Moreover, the poorly bonded regions at the coating edge represent a reduction in coating width because they must be removed in post-machining operations [3].

The benefits of the process are that most metallic materials that can be plastically deformed at high temperatures can be deposited by the FS technique. Not only similar combinations of materials can be joined, but dissimilar materials can also be deposited. Moreover, the temperature during the process is generally lower than that of the materials' melting range, so material defects are avoided. The impact on the substrate is limited compared with the fusion welding processes due to a comparably low heat input. The high degree of deformation while processing leads to grain refinement in the microstructure of the coatings, often resulting in improved mechanical properties of the coating material [35]. Furthermore, because FS is a purely mechanical process, it is a clean manufacturing technology, which allows mono-material recycling and smoke generation to be precluded. The process offers several benefits compared with conventional techniques [41]:

- Material deposition in a solid phase state
- No occurrence of arc, laser beam or unshielded flame
- No fumes and splashes
- Operator safety
- Possibility of process automation
- Non-deformable materials considered to be non-weldable can be deposited
- Possibility of joining in a dissimilar configuration without dilution
- Chemical-free process

3.3.3 Process Parameters

The process parameters, such as axial force, rotational speed and deposition speed, required to deposit metallic coatings differ significantly depending on applied material combinations. It has been reported that for titanium and aluminium alloys, a proper ratio between the axial

force and rotational speeds must be considered. The main process parameters and their function while depositing the coating by FS are introduced below:

- The rotational speed and deposition speed control the energy input into the system and in the sheared processing zone.
- Axial force is needed for an appropriate amount of plasticised material to be deposited.
- The deposition speed strongly influences the coating width and thickness; the higher the deposition speed is, the thinner the coating; an increase in deposition speed leads to short heat exposure periods and thus high cooling rates of the deposit [3].

Axial Force

The axial force (F_z) can be seen as a forging force in the plastification step. An alteration of the axial force has an impact on the heat-affected zone depth of the substrate. It was demonstrated that by increasing the axial force, the depth of the substrate heat-affected zone increases [41]. Furthermore, high forces result in wider coatings with decreased thickness [42].

Consumption Rate Control

The consumption rate control (v_{CR}) control can be chosen instead of the axial force control mode, which is most commonly used. Here, the velocity, at which the stud is fed into the process in axial (z-) direction, can be set, and the axial force will be an output parameter. The use of the consumption rate control mode has been reported for friction surface cladding [43].

Rod Rotational Speed

The rotational speed (ω) may affect the coating width and the coating surface roughness. Rafi et al. reported that for steel, the coating width and surface roughness decrease with rising rotational speed [34]. An increase in rotational speed while depositing aluminium alloys leads to decreased coating width and thickness [7]. When depositing austenitic stainless steel, an increase in rotational speed results in wider coatings at the expense of the coating height [35]. Although the effect of the rotational speed on the coating geometry was observed by various authors, no conclusive explanation was proposed. This topic will be addressed in the current work for titanium alloys.

Deposition Speed

The deposition speed (v_d) is the velocity, at which the stud travels across the substrate (in x-direction) during the deposition stage. This parameter can influence the cooling rate of the coating and therefore reduce the grain size by static recrystallisation for certain materials such as aluminium and copper. Furthermore, it was reported that an increased deposition speed leads to thinner coatings when depositing stainless steel and aluminium coatings [7, 35, 44, 45].

3.3.4   Evolution of Severe Plastic Deformation by Friction Surfacing

Severe plastic deformation (SPD) as a metal forming technique is applied to enhance the mechanical properties of materials by significant grain refinement. SPD covers several irreversible massive deformation processes, which impose high strains at hydrostatic pressure to a bulk material at certain temperatures to alter its microstructure. The SPD technique can be divided into the different mostly used related processes, such as the following:

- Equal-channel angular pressing (ECAP)
- High-pressure torsion (HPT)
- Accumulative roll bonding (ARB)
- Multi-axial forging (MAF)
- Twist extrusion (TE).

After processing by one of those methods, the originally microcrystalline material exhibits a submicron microstructure with grain sizes in the range of 100 nm to 1 μm, or it can even be transformed into a nano-crystalline material with a < 100 nm grain size [46-48].

The Friction Surfacing process can be seen as a type of SPD technique, despite the fact that in conventional SPD processes, the materials are usually deformed in a confined volume. Severe plastic deformation during the FS process was compared with the conventional SPD process in [49]. In the case of FS, a certain amount of the material (consumption rod) is deformed stepwise at high strain and force and is transferred into the shape of a deposition bead (also known as a welding bead) onto a substrate to clad it.

3.3.5   Static and Dynamic Recrystallisation

Plastic deformation of metals above their recrystallisation temperature is described as a hot deformation process, and that below the recrystallisation temperature is called a cold working process. Recrystallisation is a process by which new, stress-relieved and equiaxed grains with low dislocation density are formed, and it is characterised by reduced strength and increased ductility [50, 51]. A prerequisite for recrystallisation is a deformed structure with nuclei formation followed by grain growth. Recrystallisation occurs via the formation and movement of high-angle grain boundaries, eliminating the deformed structure.

There are two different variants of recrystallisation depending on the processing stage at which they occur. The variant that exists during the deformation is termed dynamic recrystallisation (DRX). The variant exists after the plastic deformation of the material has been completed is termed static recrystallisation (SRX) [52]. Recrystallisation can occur discontinuously and continuously. The formation of a new structure without the movement of high-angle grain boundaries is denoted by continuous recrystallisation. When dislocation movement is fast or the grain boundary movement is hindered e.g. by precipitation a massive recovery occurs, forming additional low-angle grain boundaries. Therefore, the formation of a

completely new structure is present without high-angle grain boundary migration. This variant results in a homogeneous microstructure that, because it requires no nuclei, is called continuous recrystallisation.

When applying a heat treatment to a cold deformed material, it can be observed that small grains form first, which then grow until they collide and thoroughly consume the deformed structure. This process is characterised by nucleation and growth. Thus, the dislocation density is diminished discontinuously by discrete grains, so, this process is defined as discontinuous recrystallisation [15, 52].

3.4 Wear Behaviour of Titanium Alloys

Despite their good mechanical properties, titanium alloys exhibit high susceptibility to wear damage. The physical and crystallographic properties account for the susceptibility of titanium alloys, especially to fretting wear. The wear behaviour and friction coefficient of metals with a hexagonally packed structure are dependent on the *c/a* ratio. The *c/a* ratio is defined as the relationship between the interatomic distances of the elementary cell. The *c* is defined as a long edge length (in the direction of the z-coordinate axis), and *a* is defined as a short edge length (in the direction of the abscissa) of the elementary cell. The plastic deformation occurs predominantly along the basal plane in metals with an ideal *c/a* ratio. However, titanium exhibits a low *c/a* ratio, so plastic deformation appears beside the basal plane and along the prism planes. Therefore, plastic deformation of the surfaces in contact is facilitated. In a metallic contact, the roughness differences of titanium surfaces can be levelled out easily, leading to an increase in the contact area followed by increasing adhesion affinity to the counter body [53]. Furthermore, it has been observed by many authors that titanium frequently transfers material while in contact with dissimilar materials. To increase the wear resistance of titanium, elements such as Al and Zn can be alloyed to increase the *c/a* ratio, making it closer to the ideal value and, allowing plastic deformation only along the basal planes [53-57].

In principle, many tribological systems may be compromised by the interaction of the different wear mechanisms. The appearance of the worn surfaces can specify the acting wear mechanism. Depending on the involved tribosystem and kinematics, several types of wear, such as sliding-, rolling-, impact-, and fretting wear can occur. Four main wear mechanisms may be involved in one system [53] [58]:

- Abrasion (formation of grooves and cracks and embedding of hard abrasive particles in a soft matrix of the wearing material)
- Adhesion (material transfer from one body to the other)
- Surface fatigue (formation of surface pits and cracks on the grounds of oscillating mechanical stresses)

- Tribochemical reaction (mixed chemical reactions from the body and counter body with lubricant or ambient medium, which result in surface layers that may delaminate).

3.4.1 Fretting Wear

This section focuses on fretting wear. Fretting wear is a detrimental type of wear that can accelerate crack initiation in components under oscillating loads, leading to premature failure [59].

The test configurations to investigate the wear mechanisms appearing in a certain material combination can be designed, for instance, which a cylinder-on-flat or a sphere-on-flat setup. The fretting wear is caused when the contact bodies perform an oscillating relative motion in the direction of the velocity vector with oscillation amplitude that is smaller than the dimensions of the nominal contact area. Moreover, a part of the contact area is always in contact and never open to the ambience. In contrast, a higher amplitude results in deterioration, which is referred to as reciprocating sliding wear. Fretting wear is often barely visible, and the damage occurs by fatigue mechanism due to the formation of surface or sub-surface cracks. The appearance is divided into three conditions [53] [58]:

- Stick regime (sticking with elastic deformation of the micro contacts without slipping)
- Mixed stick-slip (partial slipping at the micro contacts)
- Gross slip regime (complete sliding between micro contacts).

Generally, the wear as a progressive material loss at the material surfaces can be seen as a consequence of debris formation and debris ejection, whereas the wear rate is determined by the balance between them. Fretting wear, appearing in hip joint and blade disc (blisc) configurations, tends to maintain the wear debris at the interface between the contact bodies, allowing third body accommodation. The flow of debris ejection in those conforming geometry configurations is low, so it controls the wear rate and indirectly monitors the debris formation. For the contacts with less conforming geometries, such as a sphere/plane setup, the debris can be more easily ejected from the interface, and the contact behaviour is less dependent on the third body accommodation. Thus, the wear rate is controlled by the debris formation rate [60].

3.4.2 Increase of Wear Resistance by Different Coating Technologies

The wear behaviour of titanium alloys can be improved by different cladding or surface treatment processes with the aim to increase the surface hardness. Via processes such as ion implantation, physical and chemical vapour deposition or gas-plasma nitriding, hard coatings can be generated to harden the titanium surface [54]. The coating thicknesses basically lie within micrometre range; only by the gas-plasma nitriding process thicknesses up to 1 mm can be generated. Application of one of these processes may lead to an eggshell effect with a

hard clad on a soft matrix. Therefore, further treatment at the diffusion zone is required to increase the load-bearing ability of the top coating. Furthermore, the application of PVD coatings leads to a reduction of the fatigue strength [54, 61].

4 Experimental Procedure and Materials

This chapter gives a concise overview of the experimental equipment and materials used in this work. Furthermore, the specimen preparation for the microstructural analysis and mechanical testing and the employed experimental equipment are described in detail.

4.1 Friction Surfacing Equipment

The friction surfacing equipment used in the present work was custom-designed for high process loads and robustness for comprehensive process parameter development. This equipment is capable of delivering a 60 kN axial force, 6000 min^{-1} rotational speed and 200 Nm torque (Figure 4.1). It can operate in force or rod consumption rate (RCR) control modes (i.e., a shortening of the rod per unit of time, also denominated as burn-off rate). The machine is equipped with sensors for the simultaneous monitoring and recording of forces in three directions and with a torque sensor assembled in the spindle. The axial force can be fully controlled by an electrically driven ball screw. The dynamic electric motor for the spindle provides a constant rotational speed while processing. The working space is equipped with a profiled table, which allows simple plate clamping at the desired position. The profiled table is made of aluminium alloy, and its high thermal conductivity enhances heat transfer. The working space of 0.5 m in width and 1.5 m in length enables the coating of larger components. For this purpose, a long rod length is needed that can be effortlessly adopted into the FS equipment. The maximum usable rod length is 500 mm. The production of long coatings leads to the generation of plasticised material around the rod tip, also denominated as flash, which builds up directly at the consumable rod. For this reason, the machine is equipped with a flash cutting device to trim excessive plasticised material off the rod, which would otherwise block rod feeding. The flash cutting device is mounted at the feed part, which is directly located below the spindle. Because this component of the equipment does not move during the process, the excessive plasticised material (flash) can be simply cut during the process.

Materials, that have a high affinity to atmospheric gases, such as oxygen, must be protected by shielding gas during deposition of the coatings. For this purpose, a shielding gas cup is required. This shielding gas cup was mounted at the same feed part near the flash cutters (Figure 4.2).
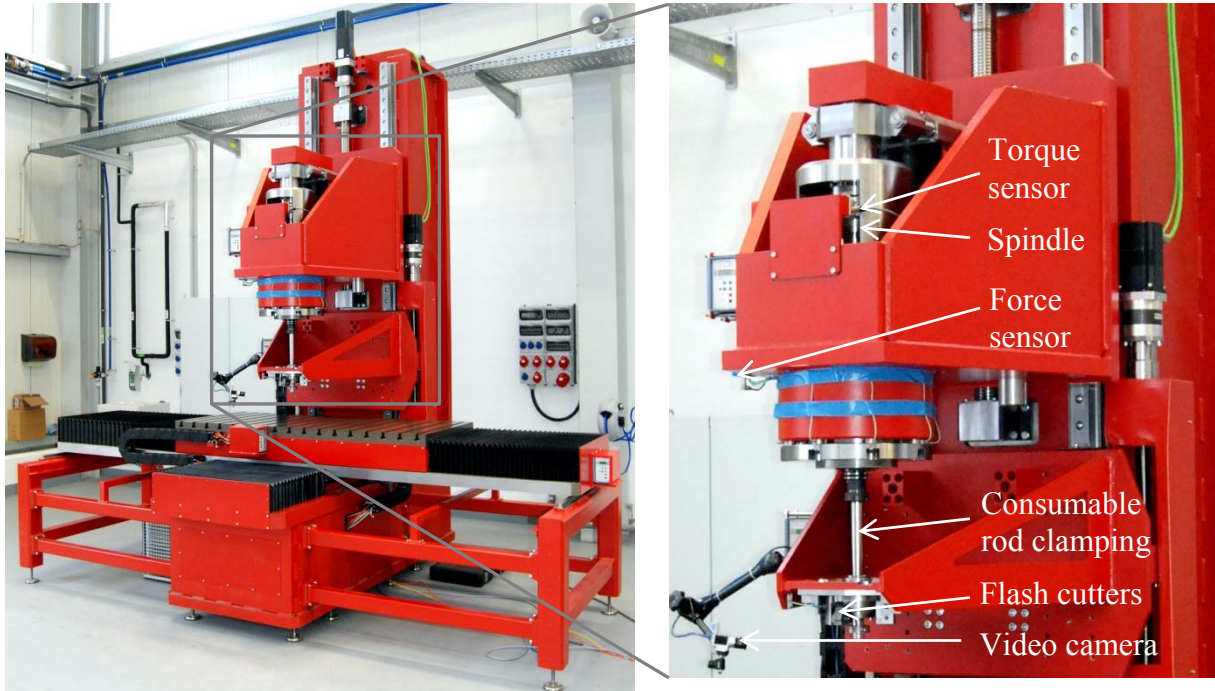
Figure 4.1: Friction surfacing machine used in the current work.

Figure 4.2: Custom-designed shielding gas cup.

4.2 Materials

In this work, two different titanium alloys were investigated: commercially pure titanium (CP) Grade 1 (ASTM B 348) and Ti-6Al-4V (ASTM B 348) alloy in round bar form as the consumable rods. Both Ti-Gr.1 and Ti-6Al-4V 20 mm diameter rods were used for this work with a length of 500 mm. The rods were delivered in hot-rolled condition. Ti-6Al-4V (ASTM F 136-08) hot-rolled plates measuring 300 mm × 100 mm × 10 mm were used as substrate for the depositions. Chemical analysis of the base materials was carried out. For the

chemical composition, three specimens of each material were analysed. Elements such as O, H and N were analysed by carrier gas hot extraction. Because other elements, such as C, Al, Fe and V, cannot be detected, they were analysed using spark spectrometry. Chemical composition analysis for the consumables and substrate is given in Table 4.1 in accordance with the specifications for these materials. To obtain the mechanical properties, tensile testing specimens were machined from the round bars according to DIN 50125-A 12 × 60 and from the plate specimens according to DIN 50125-E 5 × 16 × 50.

Table 4.1: Chemical composition of the base materials (wt. %).

	Material	Fe	C	N	H	O	Al	V	Ti
Consum. rod	Ti-6Al-4V	0.11	0.03	0.023	0.0039	0.15	6.6	3.5	Bal.
Consum. rod	Ti-Gr.1	0.28	0.01	0.0047	0.0011	0.089	0.26	0.03	Bal.
Plate	Ti-6Al-4V	0.11	0.02	0.007	0.0049	0.049	6.2	3.9	Bal.

4.3 Temperature Measurement

FS is well known as a solid-state process that achieves temperatures below the melting range of the deposited materials. It is essential to measure the temperature involved in the process to correlate it with the microstructural evolution for instance, to associate it with phase diagrams of the materials. Moreover, the temperature distribution might be affected by the employed process parameters. Therefore, thermal monitoring was conducted using thermocouples and an infrared camera during depositions.

4.3.1 Temperature Measurement using Thermocouples

For the placement of the thermocouples during the process, bore holes of 1.2 mm in diameter were drilled into the substrate. The thermocouples were passed through those holes with a thermocouple tip protruding beyond the substrate by 0.5 mm. The consumable rod was placed directly above the thermocouple tip, enabling the beginning of the deposition. The thermocouples were embedded between the coating and the substrate after deposition, recording the cooling rates at the coating/substrate interface.

Two different thermocouple types were used: types K and B. The first allows temperature measurements in the range of -270 °C to 1320 °C. Type B is designed for high-temperature measurements up to 1810 °C. To ensure that the complete temperature range was recorded, type K thermocouples were additionally employed to record cooling rates down to room temperature. The measurements were taken at a frequency of 10 Hz.

4.3.2 Temperature Measurement by Infrared Thermography

Infrared thermography is a contactless temperature measurement technique. The temperature determination of an infrared (IR) camera is based on the electromagnetic waves transmitted from every object. This technique is linked to the correlation of the emission factor for each object. The infrared camera uses the emission wavelengths at room temperature in the spectral range of 3.5 μm - 15 μm. This spectral range can also be used for high temperatures if the emission factor is known. The emission factor is dependent on the material and surface condition and lies in the range of 0.012 - 0.98. The emission factor varies with temperature [62].

Since the surface condition during processing is unknown, the appropriate emission factor at various temperatures must be defined for titanium coating surfaces. Because the specific emission factors for titanium at different temperatures cannot be found in the literature and the surface condition during the process is undefined whether it is polished or oxidised individual tests were carried out to determine the emission factor of titanium coatings. For this purpose, the deposited layers were heated in a furnace to temperatures encountered during FS in the range from 800 °C to 1300 °C in 100 °C increments, recording the thermal images with the IR camera (InfraTec, ImageIR 8300, Germany) to set the appropriate emission factor for each temperature. The defined emission factors were then applied for the temperature analysis during the FS experiments. The rod heating rate at the beginning of the deposition and the temperatures in the process zone were measured. The IR camera was placed in front of the FS table to record the temperatures from the side, collecting temperature values at the process zone and immediately behind the rod. Because the camera was focused at a given position on the consumable rod the temperature evolution in the process zone during the entire coating length has been recorded.

4.4 Dilatometer Experiments

The dilatometer equipment is commonly used to apply a thermal cycle, a given deformation or the combination of both to precisely measure the alteration in dimensions of the tested materials and investigate the effects of temperature and deformation on the resultant microstructure. A Quenching Dilatometer DIL 805 (Bähr-Thermoanalysis GmbH, Hüllhorst, Germany) was used to simulate a thermal cycle, which was recorded during deposition by friction surfacing. In this way, only the thermal history was applied to the rod material without any deformation. The equipment enables heating rates up to 2500 Ks^{-1} depending on the material and the specimen geometry. For some materials, such as titanium, the required heating rate of 404 Ks^{-1} cannot be achieved with a standard sample dimension, therefore the specimen size was minimised. For this purpose, hollow samples must be used with a length of 10 mm and external and internal diameters of 4 mm and 2 mm, respectively. This sample geometry permits a reliable temperature distribution through the entire sample thickness. The specimens are clamped between two ceramic capillary tubes in the chamber and set into a coil

(Figure 4.3). The coil is cooled by water and argon gas. The thermocouples can be welded onto the sample surface to control the thermal cycle imposed onto the sample. All samples were heated with identical heating rates to those measured during the actual FS process. The cooling rate was varied accordingly.
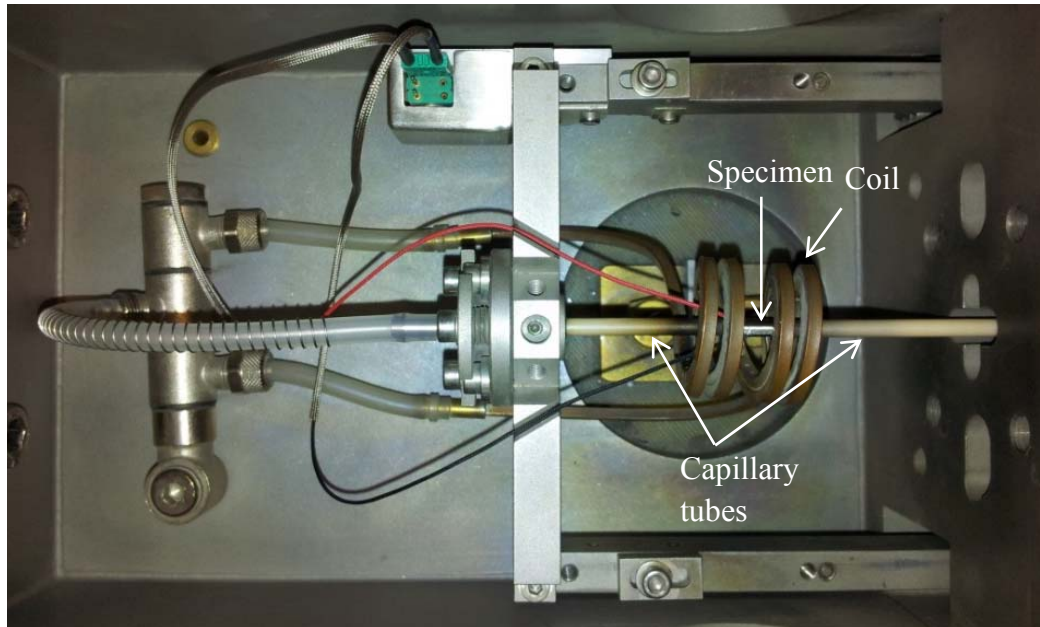

Figure 4.3: Top view of the dilatometer equipment used to apply the thermal cycle determined by the FS process.

4.5 Metallographic Analysis

To characterise the coating quality and the microstructure, metallurgical analysis was performed. Optical microscope investigation carried out on cross sections enabled coating geometry measurements. Scanning electron microscopy and transmission electron microscopy were used to thoroughly investigate the microstructure of the coatings.

4.5.1 Sample Preparation Procedure

The generated coatings were visually analysed, and overview images of the entire length of the coatings were recorded using a digital camera. From each coating, three cross sections were taken, from the start, middle and end of the coating, and were prepared according to standard metallographic practice, as described later. Initially, the specimens were mounted using hot mounting equipment (CitoPress-20, Struers, Denmark). Subsequently, the samples were ground and polished on a polishing machine (Tegramin-30, Struers, Denmark), the detailed procedure of which is presented in Table 4.2. After metallographic preparation, the specimens were etched using Kroll solution (5 ml of hydrofluoric acid, 5 ml nitric acid and 90 ml of distilled water) to reveal the microstructure.

Table 4.2: Grinding and polishing procedure.

Base pad	Suspension	Process time	Force [N]	Disc rotational speed [min^{-1}]	Rotation direction
320 SiC	Water	1 min	15	150	Co-rotation
600 SiC		1 min			
800 SiC		40 s			
1200 SiC		30 s			
2500 SiC		30 s			
MD-Mol (Struers GmbH)	3 µm diamond	5 min			
MD-Chem (Struers GmbH)	0.05 µm OPS (Struers GmbH)	5 min	20		Counter-rotation

4.5.2 Optical Microscopy

As mentioned earlier, the prepared specimens were analysed under an optical microscope (OM) (Leica Microsystems DM IRM). The OM observation was performed to determine the coating geometry on cross-sections of specimens.

4.5.3 Vibratory Polisher

A vibratory polisher, a device for the preparation of high-quality polished specimens for electron backscatter diffraction (EBSD) analysis, was used. The use of this equipment enables the achievement of deformation-free and flat specimen surfaces, which are required for proper EBSD analysis. Specimens, prepared according to 4.5.1, were polished using the vibratory polisher (VibroMet 2, Struers). The specimens were mounted on the holder without any additional load and placed onto the polishing disc wetted with OPS (Struers, Germany) polishing solution. The machine vibration was set to 30 %, and samples were exposed for 12 h.

4.5.4 Cross Section Polisher

A cross section polisher (CSP) (JEOL IB-09010CP) was used for the current work and was designed for the preparation of cross sections based on the ion fine milling technique. Cross section samples measuring $10 \times 5 \times 3$ mm were prepared and mounted in the chamber to mill a middle part of the coating. The required milling parameters depend on the material and must be individually chosen. After some attempts to mill the specimens, the suitable milling parameters for titanium were established as a voltage of 6 kV and a gas flow of 5.2, and a milling duration of 6 h was found to be an adequate time.

4.5.5 Scanning Electron Microscopy

Microstructural analysis was conducted using scanning electron microscopy (SEM) (Quanta^{TM} 650 FEG), equipped with an OIM^{TM} high-resolution electron backscatter diffraction (EBSD) system. Furthermore, SEM was used to investigate the microstructure of the base materials and coatings and for observation of fracture surfaces. Moreover, the surfaces and cross sections of fretting wear tracks were also investigated by SEM using various modes depending on the requirements. For this purpose the specimens were mounted by using an electrically conductive resin (Demotec 70). The samples for SEM analysis were not etched to avoid the topographic differences in the surface height.

4.5.6 Electron Backscatter Diffraction Analysis

Electron backscatter diffraction (EBSD) is a technique suited for observation of the crystal structure and crystal orientation. This technique has been used to investigate the phases and grain size evolution.

Specimens prepared by CSP were mounted in the proper holder and fixed with a screw to avoid any shift of the samples when using high magnification. The sample was clamped in the holder with a side angle of 70°, which is required for the EBSD measurement. Specimens that were too large for the screw sample holder were directly clamped onto the specimen stage with conductive double tape. For this configuration, the specimen stage was tilted to 70° to enable the inclined position. The EBSD images were taken from the centre of the coatings. Grain size reconstruction was performed using EBSD mapping.

Grain Size Measurement

The grain size of base materials was calculated based on the EBSD images by using the linear interception length method adapted in the OIM analysis software package. However, the grain size of the microstructures containing martensite or needles cannot be determined by that method. Therefore, a manual measurement method based on the linear interception length was implemented for the martensitic microstructure to determine the grain size.

4.5.7 Transmission Electron Microscopy

Transmission electron microscopy (TEM) is a specific microscopy technique by which thin specimens can be examined by electron beam transmission. Thereby, the electron diffraction pattern images can be obtained from the specimens, enabling the determination of the crystal structure. Furthermore, this technique enables identification of dislocations, stacking faults, twins and precipitates.

TEM (Philips Electronics Nederland B.V., Eindhoven, The Netherlands) analysis was conducted on cross-sections of the coatings and the base material of Ti-6Al-4V. The specimens were prepared in a disc shape of 3 mm in diameter with a thickness of 90 μm. The specimens were glued with a molten epoxy onto a steel sample holder, followed by grinding

and polishing steps. Thinning of the sample was performed by an electrochemical method to generate a hole in the centre of the sample. The surrounding of the generated hole should have a thickness of $\approx$ 100 nm - 200 nm to ensure penetration of the electron beam. To eliminate the residues of the electrolyte the specimens were additionally ion milled by a precision ion polishing system (PIPS).

4.6 Mechanical Testing

Micro hardness and micro flat tensile testing and fretting wear examination of the base materials and generated coatings were conducted in this work. Details of the experimental procedures and equipment are presented below.

4.6.1 Micro Hardness Test

Micro hardness measurements according to the Vickers method (DIN EN ISO 6507) were taken using hardness testing equipment (Zwick Roell Indentec ZHV 2). Indentation lines were drawn horizontally within the coating and vertically to the coating to evaluate the hardness through the heat-affected zone and the unaffected substrate. The measurements were carried out at a distance of 200 μm between each indentation with a load of 2 N (HV 0.2) and a 10 s indentation dwell time.

4.6.2 Tensile Test

The round specimens of the base materials CP titanium Grade 1 and Ti-6Al-4V were machined according to the standard DIN 50125-A 12 × 60. The flat tensile specimens of the Ti-6Al-4V plates were machined according to the standard DIN 50125-E 5 × 16 × 50. The tests were performed using a tensile testing machine (Zwick/Roell, Type: BZ-MM14780.ZW01, Ulm, Germany) and were conducted at room temperature. The testing was accomplished by displacement control with a testing velocity of 1 mm/min.

4.6.3 Micro Flat Tensile Test

Due to the limitation of the coating thickness, conventional tensile test samples cannot be machined out of the current coatings. The micro flat tensile testing method allows the determination of tensile properties in conditions under which insufficient material is available to extract a standardised test sample. The specimen geometry was designed according to the standard (DIN EN ISO 6892-1:2009-12) [63]. The required specimen geometry is 27 × 5 × 0.5 mm with a surface roughness R_t of 25 μm. The specimen geometry and dimensions are shown in (Figure 4.4). Based on the small sample geometry, this tensile testing method has been chosen as an adequate analysis for investigation of the tensile properties of the coatings.

Micro flat tensile tests were also carried out on the base material samples extracted in the rolling direction. The coating samples were tested in the deposition direction. Rod base

material specimens were electro-discharge machined directly from the round bars. Specimens from the coatings were electro-discharge machined from the coating centre and at a height distance of 0.1 mm above the substrate to ensure that the substrate material was not also sampled (Figure 4.5). Micro flat tensile testing equipment (Zwick, Germany) was used to perform the micro tensile tests at ambient temperature with a constant testing velocity of 0.2 mm/min. The displacement was measured with a laser extensometer.
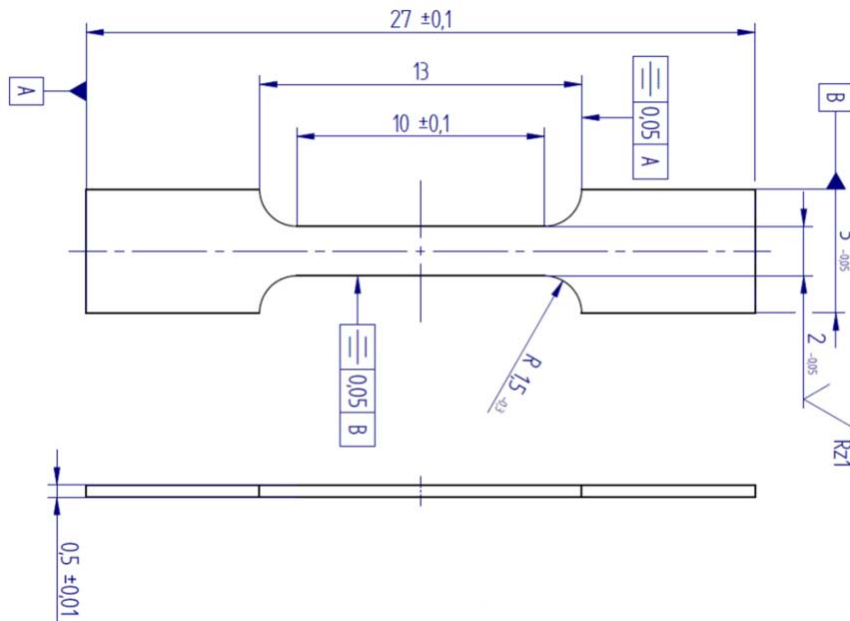
Figure 4.4: Drawing of the micro flat tensile specimen.
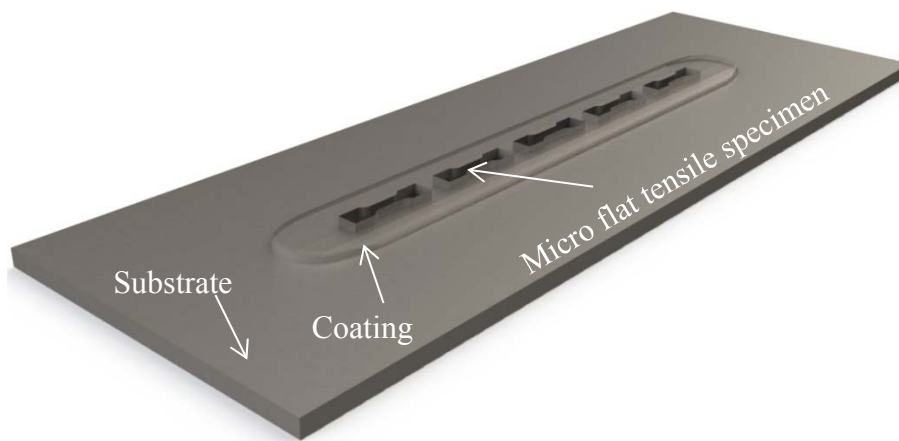
Figure 4.5: Schematic of positioning of micro flat tensile specimens within the coating.

4.6.4 Fretting Wear Test

The fretting wear tests were conceived to investigate the wear behaviour of titanium under oscillating motion. A custom-designed testing machine (University Duisburg-Essen, Germany) at the desired specification was used for testing. The tests were carried out in ball-

on-plane configuration at a frequency of 10 Hz under a normal force of 35 N and a displacement of 180 μm.

Force monitoring was carried out in three directions, measured in-situ with a 3-axis dynamometer (Type 9257A, Kistler Instrumente AG, Switzerland). During the experiments, the set and actual displacements and the testing time were recorded to control the movement of the counter body [64].

The desired load of the experiment can be set by weights, and the test duration is established by the number of cycles. The testing installation includes two components: the testing material, defined in tribology as the base body, and a component to enforce the wear evolution, defined as the counter body. High-precision spheres from high-performance ceramics (ZrO_2), which are usually made for gears, were used in the experiments with a diameter of 32 mm and a surface roughness of 0.032 μm as a counter body. The ceramic sphere with high wear resistance was chosen to evaluate the wear of the tested material. The mechanical and physical properties of the ceramic sphere are displayed in Table 4.3. The coatings and base materials were used as the base body. Samples measuring 10 × 10 × 15 mm were prepared for the testing. The coating samples were separated from the middle of the deposit. Cross section samples have been prepared from the base material. The sample top surface was ground and polished according to the metallographic preparation presented in subsection 4.5.1. For the tests, the sample was clamped in the movable table and fixed with a screw and the ZrO_2 sphere as a counter body was clamped in the upper mechanism and eventually lowered to the sample until contact. The experiments were carried out without lubrication at uncontrolled ambient conditions. The normal force was set to 35 N. The number of cycles was varied from 100 to 10^6 the stepwise variation and duration of the experiments are presented in Table 4.4. Table 4.5 presents the process parameters used to produce coatings for wear experiments.

Table 4.3: Mechanical properties of the high-precision sphere provided by Hartstofftechnik GmbH.

Material	Density [g/cm^3]	Hardness [HV]	Yield strength [MPa]	Bending stress [MPa]	Young's modulus [GPa]
ZrO_2	6	1200	2100	1000	200

The wear behaviour of coatings from both titanium alloys produced under two different conditions was characterised by a fretting wear test in a sphere-plane configuration at constant testing conditions with the exception of the testing time. Among the experimental results, the normal and tangential forces were analysed, and the friction coefficient was determined based

on the measured force results. Furthermore, the generated wear volume and maximum wear depth were measured. Eventually, cross sections of the wear tracks were prepared.

Table 4.4: Number of cycles and duration of the fretting wear experiment.

Number of cycles	Time
100	10 s
500	50 s
5,000	8 min 20 s
50,000	1 h 23 min
500,000	13 h 50 min
1,000,000	27 h 40 min

Table 4.5: Material conditions investigated by the wear analysis.

Materials	Ti-6Al-4V Coating		Ti-Gr.1 Coating		Base materials
Rotational speed $[\text{min}^{-1}]$	400	6000	300	6000	-

Confocal White Light Microscopy

Confocal white light microscopy is based on three-dimensional surface topography measurements. The fretting wear scars were analysed using confocal microscopy (CM) (μSurf, NanoFocus AG). The obtained results were evaluated by the μsoft analysis software package. Images taken from the surfaces of the wear tracks by CM enable profile measurement of the wear depths (cavity) of the coating and transferred material from the coating to the sphere (convexity). The fretting wear profile measurements were conducted in the oscillating direction and perpendicular to the sliding direction. Convex profiles of the ceramic spheres were measured.

Cross sections of the coating wear tracks were prepared perpendicular to the sliding direction to compare the wear profile measured using CM with wear depths of cross sections and to investigate the wear mechanisms and their influence on the microstructure. By means of cross section the deformation mechanisms can be investigated. The coatings were ground and polished according to the standard metallographic procedures previously described.

5   Results and Discussion

The following chapter is divided in two main themes. One section deals with the fundamental development of titanium alloy depositions by the FS process because no studies of process parameters are available in the literature and the reasons for the failure to deposit titanium alloy coatings were not reported. The failure reasons are elaborated in this work. This chapter concentrates on the development of the consumption rate control mode to ensure process stability, and on investigation of the temperature distribution within the coating while processing. Furthermore, the essential mechanism of flash formation at the coatings, which was for the first time observed in the current study, will be introduced and discussed. The other section is concerned with the investigation of coating quality, covering layer formation, its geometric features and the complex microstructure development resulting from the thermo-mechanical phenomena characteristic of the FS process. The understanding of the microstructure development is used in the interpretation of the obtained mechanical properties and observed fretting wear behaviour.

5.1   Process Development for Depositing Titanium Alloys

Thermo-mechanical processes, such as Friction Surfacing are affected by the hot deformation behaviour of titanium materials. The hot deformation behaviour depends on the chemical and phase composition, microstructural characteristics and process conditions such as strain, strain rates and deformation temperature. These process conditions exhibit the relationships among the plastic flow stress, temperature and strain rates. An increase in temperature generally reduces the flow stress, and an increase in strain rate at a constant temperature typically increases the flow stress [65, 66].

5.1.1   Preliminary Considerations

The settings of the FS process involve numerous parameters; thus, only the more relevant ones are treated in this study, which consist mainly of deposition speed, axial force and rotational speed. Generally, the process can be divided into two steps: the plastification phase at the beginning of the process before the traversal movement is superimposed and the deposition phase. For both the plastification phase and the deposition phase, different axial force and rotational speed settings can be adjusted by force and rotational speed ramps, which are controlled by the ramp time. A prospective process parameter study will concentrate mainly on the second phase, the deposition phase. Both temperature evolution and acting strain rates during FS can be assumed to mainly dependent on the parameters including rotational and deposition speeds.

As mentioned previously, continuous titanium coatings have not been successfully deposited by FS. Rao et al. [10] published a feasibility study attempting to deposit titanium coatings

onto different substrates, such as Al, Cu, Inconel, Mg and Ti, with the conclusion that titanium coatings could not be deposited successfully onto any substrate. Unfortunately, the process parameters, that were employed in the attempted deposition of titanium coatings have not been published in [10]. The selection of process parameters for any material, in similar or dissimilar configurations, depends on their individual properties such as material strength, physical properties, thermal conductivity etc. [35, 67]. Thus, FS process parameters leading to successful depositions of other materials might not produce the same results when applied to titanium alloys. Due to the different material characteristics and their deformation behaviour, the process implementation must start from scratch every time a new material is investigated. Therefore, parameters to deposit titanium alloys must be explored. Many studies have been published on the joining of titanium alloys by friction stir welding (FSW) [68-75]. The FSW process is, similar to FS, a thermo-mechanical process based on the plastic deformation of materials at high temperatures but without reaching the liquid state. FSW is a solid-state process that uses a non-consumable tool inserted into the abutting edges of sheets or plates to be joined that subsequently traverses along the joint line [76].

Since previous publications have demonstrated the possibility of joining titanium alloys by this technique, the starting point of the current study was based on results achieved with the FSW process. The initial study to develop the process parameters was based on parameters provided in the literature for joining titanium alloys by FSW using a low rotational speed in the range of 300 min^{-1} to 1000 min^{-1}. The employed axial forces during FSW experiments were difficult to find in the literature. The traversal speed (35 mm/min – 50 mm/min) reported for the FSW process was not considered for the initial FS study because the traverse speeds are generally slightly lower in FSW. The use of the low traverse speed in FSW generates a certain amount of heat required for joining two sheets [77]. In FS, the friction between the consumable rod and substrate generates heat in the process zone for sufficient plastification of the rod tip during the plastification phase, so such low deposition speeds are usually not required.

5.1.2 Parameter Development and Implementation of Consumption Rate Control

An initial parameter study for titanium coatings was established with a concentration on the rotational speed values used for FSW investigations for joining titanium sheets. At the beginning of the parameter study for FS of titanium alloys, the deposition speed was kept constant (12 mm/s), and the rotational speed and axial force were varied. Since no axial force parameters were found in the FSW literature, the force values applied by FS for the deposition of steels were employed. These axial force values were chosen because of the similarity of some material properties of steel and titanium alloys such as strength and melting temperature range. The initial experiments (when using 400 min^{-1} and 600 min^{-1} rotational speeds) and axial force in the range of 9 kN to 15 kN did not lead to any titanium depositions. The combination of the chosen parameters did not provide sufficient heat, and the consumable rod

tip did not plasticise. The consumable rod merely traversed along the substrate without leaving any material on it. By analysis of the experimental data, the torque values were found to be extremely low. Moreover, it seemed that the combination of the selected axial force and rotational speed was inadequate, providing insufficient energy by frictional heating. Similar observations have been reported when depositing tool steel (H13) coatings with low rotational speed and 10 kN of axial force [36]. To generate sufficient energy, either the rotational speed or axial force had to be increased. To understand the influence of the individual parameter, only one factor was varied at a time. Therefore, the rotational speed was first increased to 700 min^{-1} and 900 min^{-1}. The consumable rod tip began plasticising at the beginning of the experiment, and once the deposition speed was superimposed, the coating could be partially deposited onto the substrate. Recorded data revealed higher torque values, confirming an appropriate adaptation of parameters. However, further experiments with a variation of process parameters did not provide continuous depositions. Only short sections of the traverse path displayed the deposited material. Considering the discontinuities of the deposits, the axial force data were analysed. The analysis revealed that the employed axial force values could not be held constant during the entire process, resulting in oscillating force peaks in a broad range. Discontinuous deposited coatings produced at 700 min^{-1} and 900 min^{-1} rotational speeds with a respective record of the axial force data are presented in Figure 5.1. It can be seen that the desired force values (20 kN for (a) and 2 kN for (b)) could not be kept constant, oscillating in the range of 15 kN to 35 kN (a) and 1 kN to 6 kN (b) resulting in regions with discontinuous material transfer. These fluctuations in the axial force during the process are responsible for discontinuous material transfer onto the substrate. The variation observed in the force is not linked to the force control feature of the FS machine but rather to the behaviour of titanium under the imposed process conditions.

Similar behaviour in terms of force susceptibility has been reported for Ti-6Al-4V alloy during deformation under isothermal forging conditions. It has been demonstrated that the ram rate sensitivity of the forging pressure (ratio of incremental change in stress to the resultant change in strain rate) depends on the developed temperature, as can be seen in Figure 5.2. The sensitivity rises and then declines with increasing temperature [78]. This implies that the force sensitivity at a certain process temperature results in oscillating force values, which might be responsible for the generation of the discontinuous deposited coatings. Similar difficulties for joining Ti-6Al-4V alloys using force control by FSW have been reported by Mishra et al., whereas CP titanium could be joined using load control [79]. In the current study, the force sensitivity was observed for both Ti-6Al-4V and Ti-Gr.1.

Since it has been shown that titanium alloys can be deposited, although only discontinuously, and further variation of the parameters did not provide enhanced coating appearance, additional efforts had to be undertaken to improve the coating continuity. Whereas FS coatings are usually generated using axial force control [6, 35, 45], implementation of a

consumption rate mode in the FS equipment was considered for deposition of titanium coatings. The consumption rate mode controls the amount of material per unit of time being applied onto a substrate, with axial force being an output parameter.
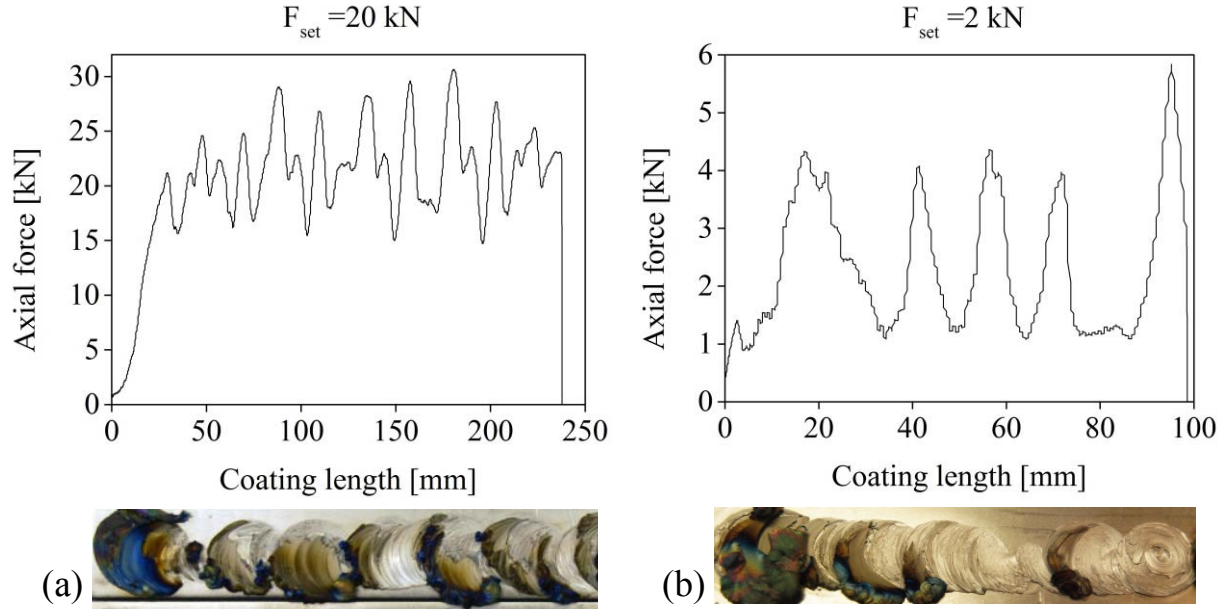

Figure 5.1: Ti-6Al-4V coating top views produced at 700 min⁻¹ (a) and 900 min⁻¹ (b) rotational speeds and a 12 mm/s deposition speed with 20 kN and 2 kN axial forces, respectively. The recorded axial force curves in both experiments demonstrate oscillating behaviour.
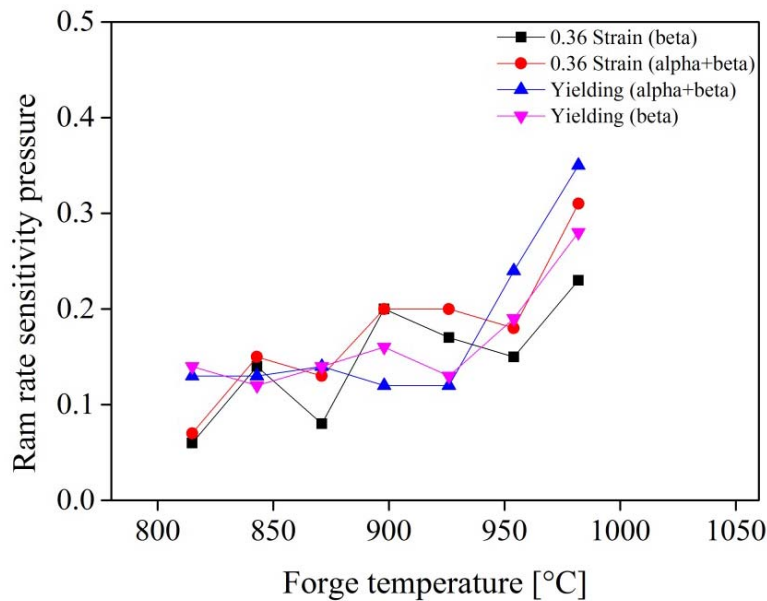
Figure 5.2: Ram rate sensitivity of the forge pressure vs. temperature according to Chen [78].

The calculation of the deposited amount of material per unit of time was necessary for the implementation of the consumption rate control. A coating with partially deposited material is demonstrated in Figure 5.3, which also depicts the fluctuating force curve. To determine the appropriate consumption rate parameter, the regions where the coating was properly deposited (highlighted by white lines) were taken as a basis for the calculations of the respective rod consumption rate (Figure 5.3). It was assumed that at those regions, enough material was fed in force control mode to deposit an appropriate amount of material. The consumed length of the rod in those regions was divided by the time the coating section was deposited. The calculated value for the needed rod consumption rate (1.8 mm/s) was established and was used instead of the axial force control. When using the rod consumption rate control, the axial force is not a setting parameter but a resultant parameter from the rod consumption rate setting. All further experiments were carried out using the consumption rate control. Coatings with continuously deposited material were realised by this method, and the newly employed rod consumption rate control proved to be a suitable operational mode for titanium depositions, ensuring that a given amount of consumable material was deposited. The conclusion of Rao et al. that the instability of titanium at elevated temperature precluded titanium deposition by FS, in general was therefore rebutted [10].

(a)

(b)
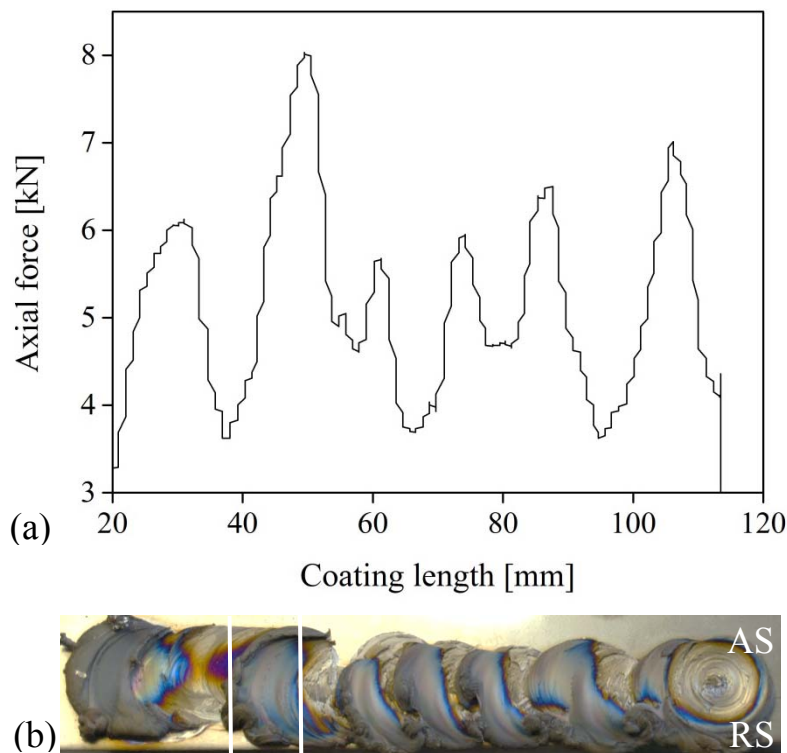
Figure 5.3: Discontinuously deposited Ti-6Al-4V alloy coating when using axial force control; coating region (highlighted by white lines) was taken as a reference region for calculation of the required consumption rate (b) and corresponding fluctuating axial force curve (a).

One of the coatings generated using the newly implemented consumption rate control is shown in Figure 5.4. It can be seen that the process enabled continuously deposited material. However, excessive material accumulation (flash) at the retreating side of the coating was observed (Figure 5.4 b). The resultant force curve still exhibits marginal oscillatory behaviour, but these low fluctuations no longer affect the coating continuity. Both setting parameters, the rod displacement and the rotational speed, were excellently controlled and did not show any instability during the process (Figure 5.4 a).

However, the coating appearance was different compared with the coating appearance reported in the literature for other materials [36, 80, 81], exhibiting formation of the flash at the coating retreating side (Figure 5.4). The mechanism of flash formation at the coating will be detailed in subsection 5.2.1 in detail.
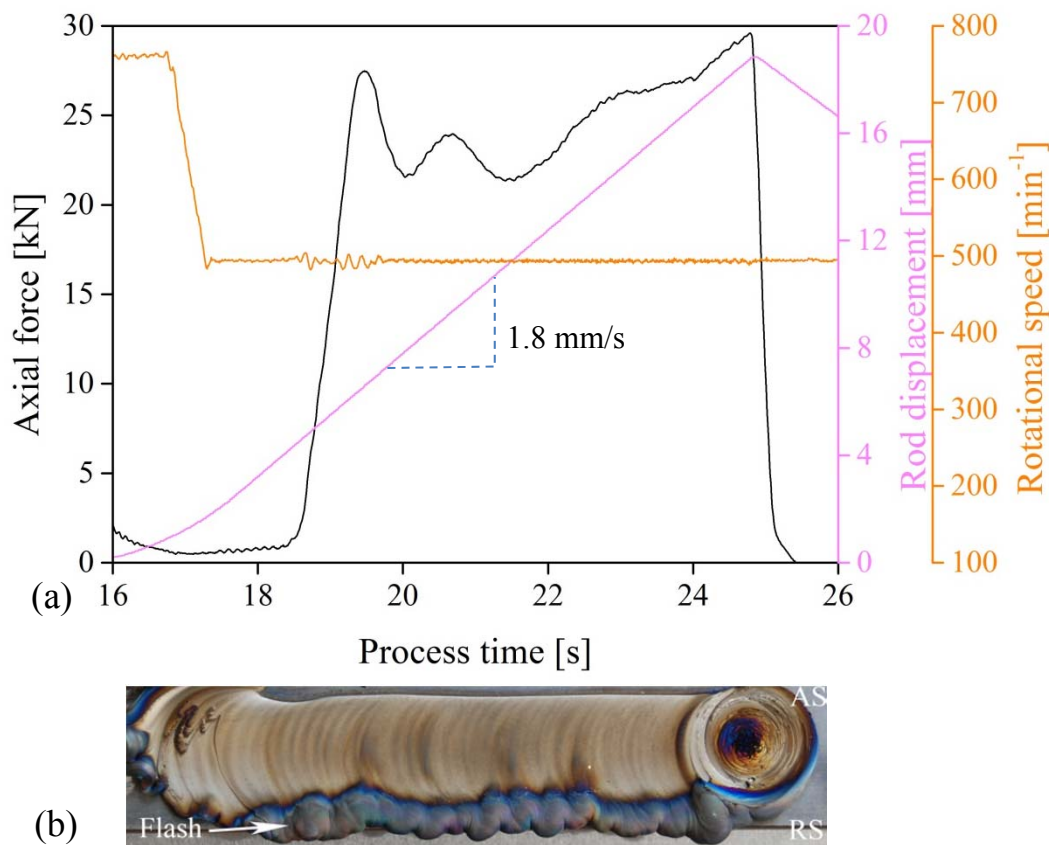
Figure 5.4: Continuous deposition of a Ti-6Al-4V coating (1.8 mm/s CR, 500 min^{-1} rotational speed and 16 mm/s deposition speed) when using consumption rate control (b) and resulting fluctuating axial force behaviour, as well as stable rotational speed and rod displacement (a).

5.2 Process Parameter Study

A systematic process parameter study on the deposition of Ti-6Al-4V and titanium grade 1 coatings was carried out. To investigate the impact of the rotational speed on the coating

formation behaviour, the minimum and maximum values of the rotational speed of the FS machine were selected as threshold values for the current study. Since the maximum allowable torque of 200 Nm was nearly achieved at 300 min^{-1}, the rotational speed could not be further lowered and 300 min^{-1} was taken as the lowest possible rotational speed for the current study. The maximum rotational speed (6000 min^{-1}) that can be realised by the FS equipment has been taken as a maximum rotational speed for the current study. Hence, to thoroughly examine the influence of the process parameters, the investigation was carried out in a wide range of rotational speeds from 300 min^{-1} to 6000 min^{-1} for both titanium alloys. Images of Ti-Gr.1 and Ti-6Al-4V coatings generated at various rotational speeds are presented in Figure 5.5.

Basically, the process development for both titanium alloys regarding the rotational speed can be divided into two parts according to the flash formation. In this context, the rotational speed was varied as mentioned above, and other parameters were held constant with a deposition speed of 16 mm/s and a rod consumption rate of 1.6 mm/s.

As shown in Figure 5.5 a, a part of the investigation of Ti-6Al-4V coatings was accomplished by the use of low rotational speeds in the range of 400 min^{-1} to 1000 min^{-1}, varying in increments of 100 min^{-1}. The second part involved rotational speed from 2000 min^{-1} to 6000 min^{-1} varying in increments of 1000 min^{-1}. Figure 5.5 a exhibits Ti-6Al-4V coatings with smooth surfaces without an oxidation layer at rotational speed of 400 min^{-1} to 600 min^{-1}. When increasing the rotational speed in the range of 700 min^{-1} to 1000 min^{-1}, discontinuous coatings with flash formation and tempering colours at the flash material can be observed. The flash formation at the coatings produced at high rotational speeds (2000 min^{-1} – 6000 min^{-1}) is suppressed, and the surface appearances are rough and oxidised, demonstrating a typical FS welding bead structure.

The images of Ti-Gr.1 coatings produced at various rotational speeds are presented in Figure 5.5 b. Considering that the process parameters for both titanium alloys were identical, the differences in coating appearances can be clearly seen. Flash formation for both materials appears in different rotational speed ranges. The incidence of the flash formation in the Ti-Gr.1 coating occurs in a large range of 300 min^{-1} to 2000 min^{-1}. The wider range of the flash formation here can be related to the absence of alloying elements and thus the lower strength of Ti-Gr.1 leading to higher peak temperatures while processing. This low strength of pure titanium at high temperatures may lead to flash formation in a wide range of rotational speeds.

Considering the final industrial application of the coatings, even coating surfaces are required, which must be machined. The flash formation at the coatings can be seen as a negative factor for machining and might require complex machining work. Therefore, coatings without flash

formation may be of greater interest for the industry. Nevertheless, all presented coatings have been analysed in the current work with regard to the microstructure and mechanical properties to understand whether coatings with flash differ from those without. The presented process parameter study has substantiated that titanium coatings can be deposited successfully by FS in a broad variation of rotational speeds.
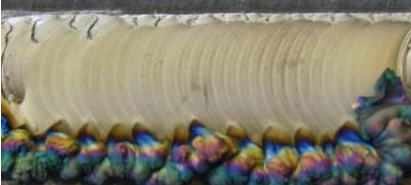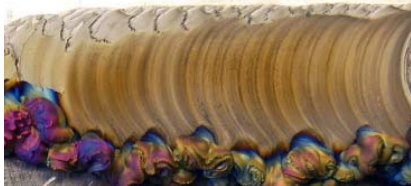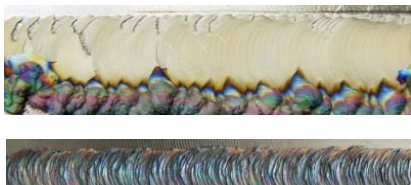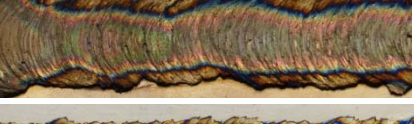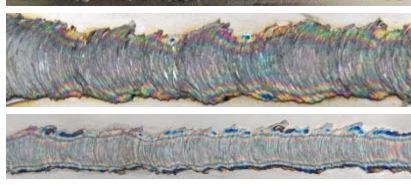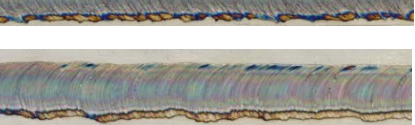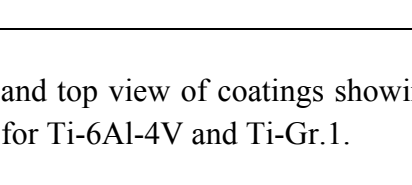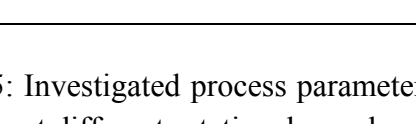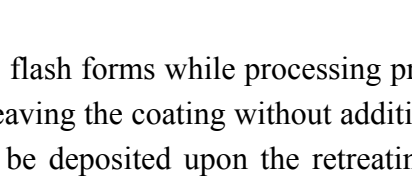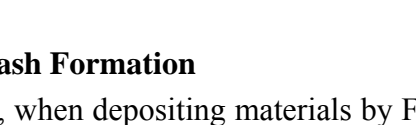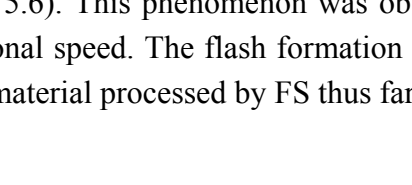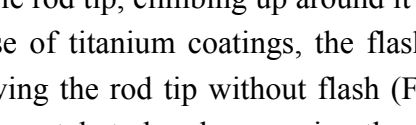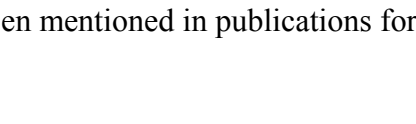
Rot. speed [min⁻¹]	a) Ti-6Al-4V coating top views (16 mm/s dep. speed, 1.6 mm/s cons. rate)	b) Ti-Gr.1 coating top views (16 mm/s dep. speed, 1.6 mm/s cons. rate)	Rot. speed [min⁻¹]
300			300
400			400
500			500
600			600
700			700
800			800
900			900
1000			1000
2000			2000
3000			3000
4000			4000
5000			5000
6000			6000

Figure 5.5: Investigated process parameter sets and top view of coatings showing the typical appearance at different rotational speed regimes for Ti-6Al-4V and Ti-Gr.1.

5.2.1 Flash Formation

Generally, when depositing materials by FS, the flash forms while processing primarily at the consumable rod tip, climbing up around it and leaving the coating without additional material. In the case of titanium coatings, the flash can be deposited upon the retreating side of the layer, leaving the rod tip without flash (Figure 5.6). This phenomenon was observed during the experimental study when varying the rotational speed. The flash formation at the coating has not been mentioned in publications for any material processed by FS thus far.
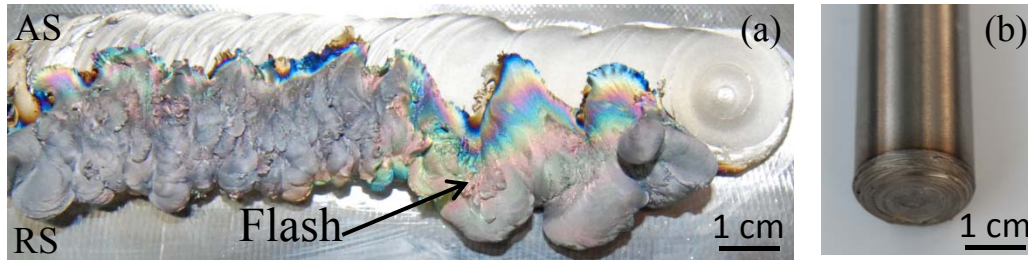
Figure 5.6: Top view of the coating with flash formation at the RS (a) and with corresponding consumed rod consequently without flash (b).

To understand the effect of flash formation at the coating, which was related incipiently to the variation of the rotational speed, additional experiments were conducted. It has been noted that when employing the high rotational speed range (2000 min^{-1} - 6000 min^{-1}), the flash does not generate at the coating but rather forms exclusively at the rod (Figure 5.7). It seems that flash formation at the coating occurs at a certain rotational speed range, suggesting two groups of parameter sets where flash may be formed either at the coating or at the rod. The flash formed at the coatings could only be observed at the rotational speed ranges of 300 min^{-1} – 2000 min^{-1} for Ti-Gr.1 and 300 min^{-1} – 1000 min^{-1} for Ti-6Al-4V. Because the deformation in a certain range affects the flow behaviour of titanium, additional factors may also be involved in flash formation and should be considered.
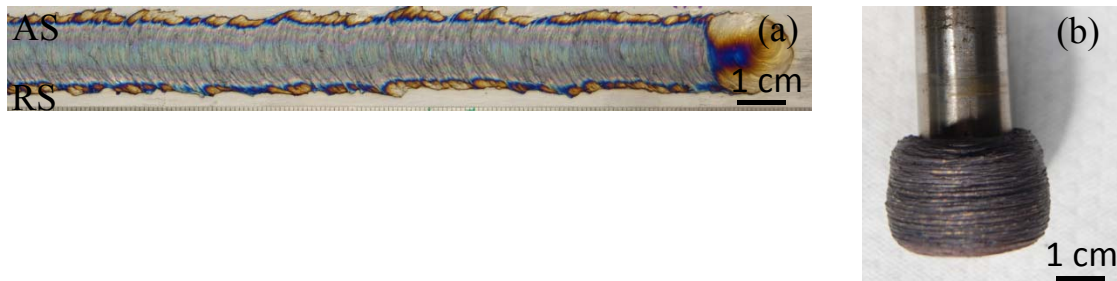

Figure 5.7: Top view of the coating generated at 3000 min^{-1} rotational speed, 16 mm/s deposition speed and 1.8 mm/s consumption rate (a) and corresponding rod with flash formation (b).

To investigate the energy generated by the variation of rotational speed while processing, the energy input per unit length (EI) was determined by the following equation, derived from the FSW process [82]:

$$EI = \frac{2\pi\tau\omega}{v} \quad \text{Eq. (1)}$$

where τ is the torque [Nm], ω is the rotational speed [rev/min], and v is the deposition speed [mm/min].

The effect of rotational speed on the calculated energy input per unit length and maximum temperature at the interface coating/substrate for Ti-6Al-4V is presented in Figure 5.8. It can be observed that at low rotational speeds (300 min^{-1} – 1000 min^{-1}), where the coating flash formation occurs, the energy input per unit length tends to rise. At 2000 min^{-1}, from which on the flash occurs at the rod, a peak value of energy input per unit length is reached (410 J/mm). In the following high rotational speed range, the EI values reach a constant value of approximately 390 J/mm.
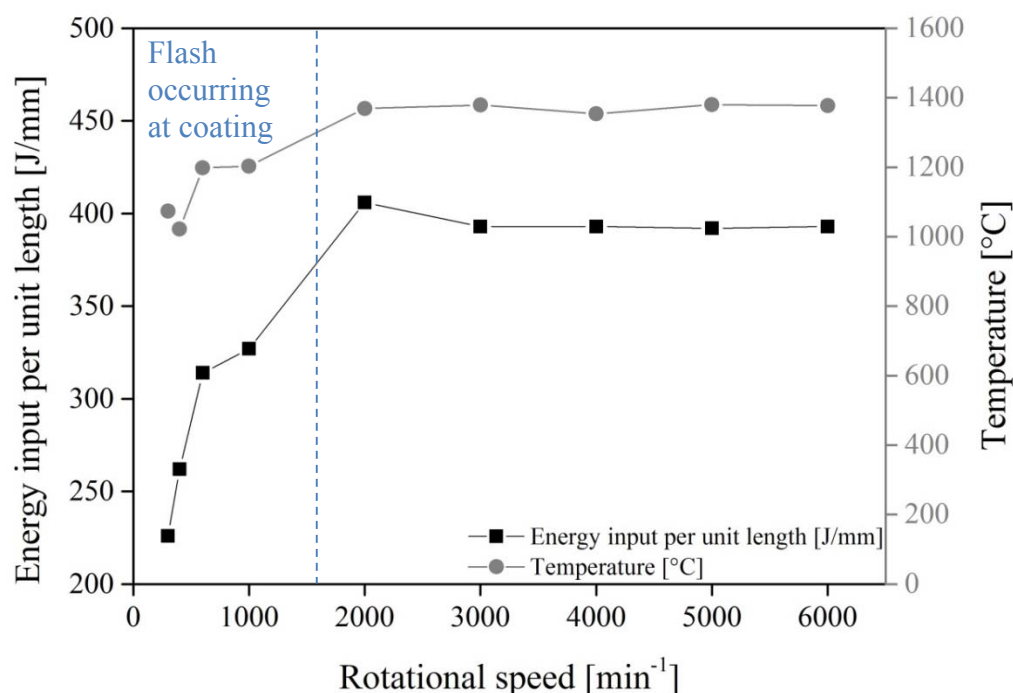

Figure 5.8: Relationship between rotational speed, energy input per unit length and temperature for Ti-6Al-4V coatings.

Moreover, the torque values are displayed as a function of rotational speed in Figure 5.9. A clear decrease in torque with increasing rotational speed can be observed. First, the torque decreases rapidly, followed by lower decay at high rotational speeds, the material reaches a "low viscosity" condition, due to very low shear stresses, which limits the generation of heat, causing a steady-state in the temperature.

The calculated energy input correlates very well with the temperature measured in the coating/substrate interface, also for Ti-Gr.1 coatings (Figure 5.10). The energy input first increases from 133 J/mm at a 300 min^{-1} rotational speed to 510 J/mm at 3000 min^{-1} and then decreases to 471 J/mm at 6000 min^{-1}. For both titanium alloys a peak value of the EI was noticed which led to the coarse grain size discussed in section 5.5. The temperature trend pursues identical behaviour as the energy input, rising up to 3000 min^{-1} (1400 °C) and then declining rapidly with rotational speed up to 6000 min^{-1} (1000 °C). It is noteworthy that for

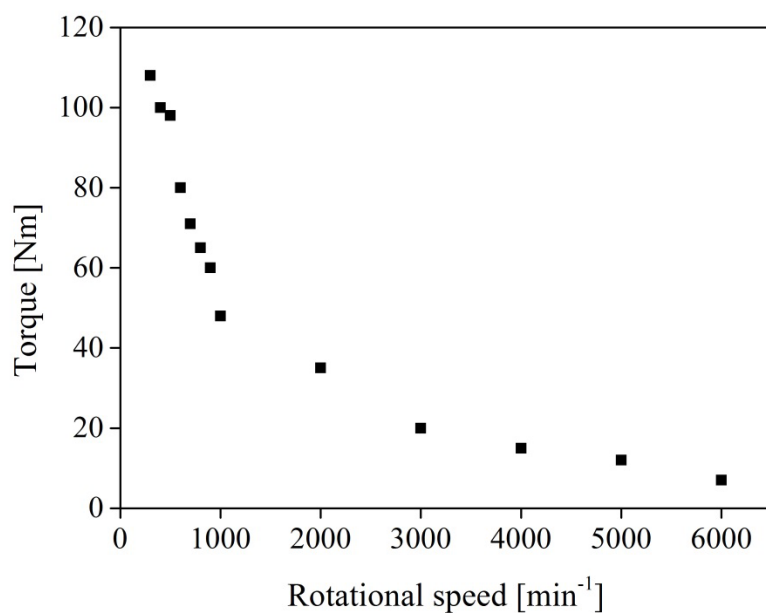deposition of titanium grade 1 coatings, also two different rotational speed regimes are recognisable.

Figure 5.9: Torque evolution as a function of the rotational speed for Ti-6Al-4V coatings.
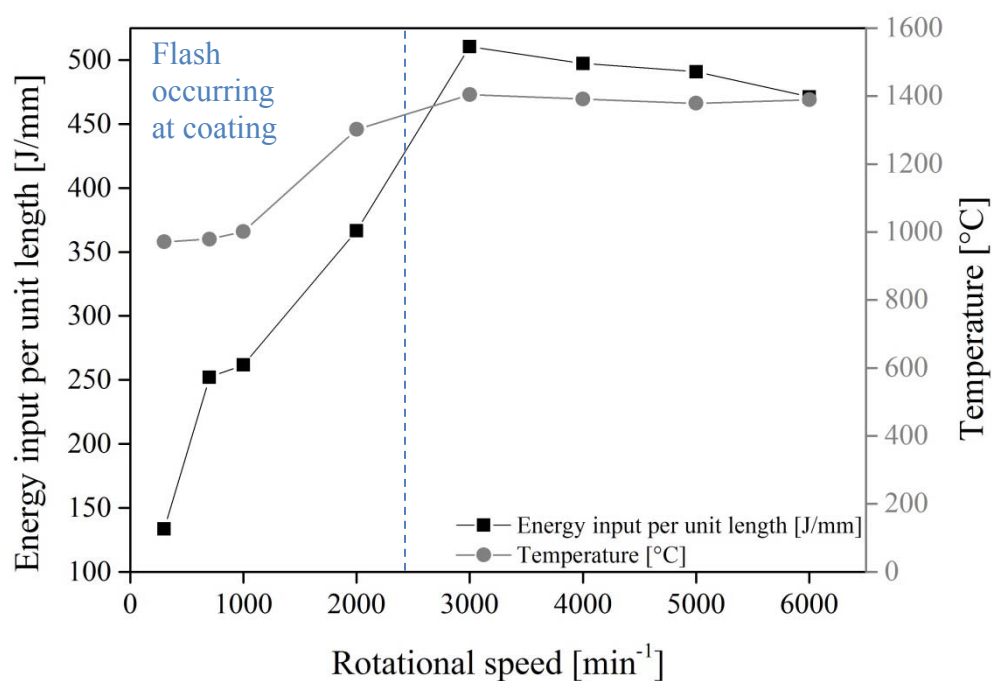

Figure 5.10: Temperature and energy input per unit length depending on the rotational speed in Ti-Gr.1 coatings.

Considering that flash at the coating occurs in a certain rotational speed range, it might be assumed that this behaviour is related to the strain, strain rates and resultant temperature imposed during the process. Therefore, further investigation of the flash formation will concentrate on the strain and strain rates, which are governed by the variation of rotational speed and deposition speed. The results of temperature measurements will be described in more detail in section 5.3. The deposition speed determines how long the consumable rod is in contact with the substrate. A low deposition speed may lead to a high energy input and thus high temperatures. Therefore, further experiments varying rod rotational speed and deposition speed have been conducted to demonstrate their relationships with the energy input and flash formation behaviour.

The rotational speed was varied at 300 min^{-1}, 400 min^{-1} and 600 min^{-1} with deposition speed variation from 8 mm/s to 20 mm/s for Ti-6Al-4V coatings. For the flash investigation on the Ti-Gr.1 coatings, the rotational speeds were varied at 300 min^{-1}, 400 min^{-1} and 600 min^{-1} with deposition speed variation from 8 mm/s to 32 mm/s.

The energy input per unit length, as an indicator for the heat generated in the process has been plotted against the rotational speed; the grey dots indicate flash formation at the coating, and the black ones represent the flash located at the rod (Figure 5.11). When observing coatings generated at a constant rotational speed of e.g. 300 min^{-1} and two different deposition speeds, different EI values can be seen. A high deposition speed in Ti-6Al-4V results in a low EI value (157 J/mm), and a low deposition speed results in higher EI (432 J/mm), resulting in flash formation at the coating (Figure 5.11 a). This trend can be seen for the other two rotational speeds (400 min^{-1} and 600 min^{-1}) as well.
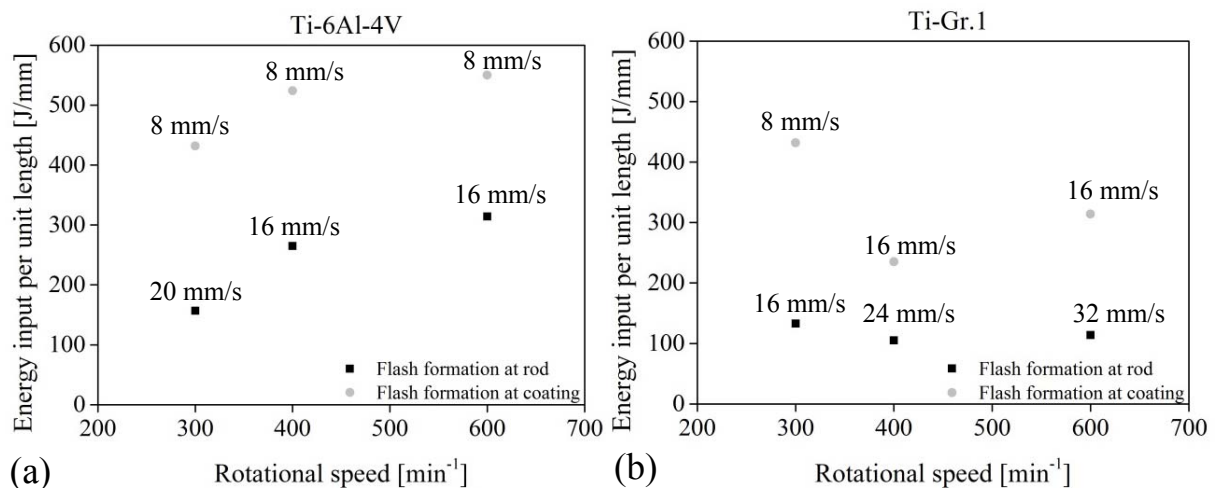

Figure 5.11: Combined effects of deposition speed and energy input on the flash formation of Ti-6Al-4V coatings (a) and Ti-Gr.1 coatings (b) with corresponding deposition speed placed above the dots.

The flash formation on Ti-Gr.1 coatings as a function of the energy input per unit length and rotational speed is demonstrated in Figure 5.11 b for selected parameter sets. The same trend can be seen, as already observed for Ti-6Al-4V, that a high energy input at a given rotational speed leads to flash generation at the coating. Still, the fact that higher deposition speeds are required to reduce the energy input for the same rotational speed can be observed here. When comparing an identical condition (600 min^{-1} rotational speed and 16 mm/s deposition speed) for Ti-Gr.1 and Ti-6Al-4V, at which an equal heat input (314 J/mm) was generated, the same heat input results in flash generation at the coating in Ti-Gr.1 but results in flash-free coating in Ti-6Al-4V. This supports the assumption that flash formation at the coating is generated at a certain combination of rotational and deposition speeds for the individual titanium alloy.

It can be stated that to produce flash-free coatings at a desired rotational speed, the deposition speed must be sufficiently high to limit the energy input.

Since only selected parameters can be compared, as shown in Figure 5.11, an additional, unitless factor x_{flash} was introduced to further categorise the flash formation. This factor includes not only the process parameters such as deposition speed (v) and rotational speed (ω) but also resulting parameters such as torque (τ) and axial force (F):

$$x_{flash} = \frac{\tau\omega}{Fv} \quad \text{Eq. (2)}$$

From this ratio it can be seen that not only a rise in energy input ($\sim\tau\omega/v$) increases the x_{flash} factor, leading to flash formation on the coating. The resultant axial force (F) evidently has a significant effect, too. Figure 5.12 shows the x_{flash} factor as a function of rotational speed, suggesting two different regimes.
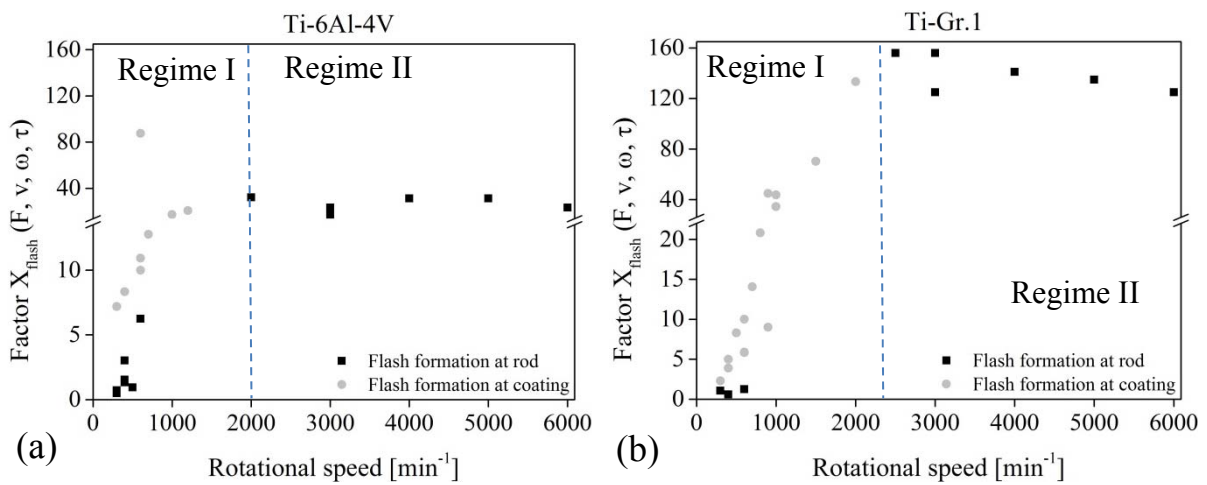

Figure 5.12: Flash formation factor x_{flash} as a function of the rotational speed for Ti-6Al-4V coatings (a) and Ti-Gr.1 coatings (b) for both regimes.

In regime I for Ti-6Al-4V coatings, it can be seen that a sharp threshold exists, between the flash forming at the rod ($x_{flash} \leq 6.25$) and flash formed at the coating ($x_{flash} \geq 7.18$) (Figure 5.12 a). Above a rotational speed of 2000 min^{-1} in regime II, the factor x_{flash} is in a high range from 17 to 32 but the flash is formed exclusively at the rod, supporting the theory of two different regimes acting. For Ti-Gr.1 the transition value from flash formation at the rod to the coating is very low ($x_{flash}=2$) (Figure 5.12 b) compared to Ti-6Al-4V. Also the boundary to regime II is shifted to a rotational speed of 2500 min^{-1}. The x_{flash} values in regime II for Ti-Gr.1 are generally higher than for Ti-6Al-4V coatings.

5.2.2 Process Response in Two Different Regimes

In the following, selected parameter conditions from the low rotational speed regime and from the high rotational speed regime will be discussed in detail.

Seshacharyulu et al. reported flow stress data of titanium at various temperatures, strains and strain rates determined by hot compression experiments. It was shown that an increase in temperature at a constant strain rate leads to lower flow stress. Although this decrease in stress is less pronounced at high temperatures, for a strain rate of 10 s^{-1} it still drops from 98.2 MPa at 1000 °C to 72.6 MPa at 1100 °C, at a strain of 0.5 [83]. When decreasing the deposition speed at constant rotational speed during FS, a similar behaviour may be assumed, since the process temperature rises under a comparable shear rate. This increase in temperature leads to a reduction of the flow stress due to a higher degree of thermal softening (dislocations are annihilated), in relation to strain hardening (dislocations are formed). It must be assumed, that the material flow stress affects the process force and torque (see Figure 5.9) acting during FS. Further, the low flow stresses at low deposition speeds could promote the formation of the flash at the coating, when the plasticised material is too soft to climb up around the rod. Additionally, the appearance of coatings with flash is extraordinarily smooth, without indication of the typical coating bead appearance, which might be an additional indicator of thermal softening (Figure 5.4). Once the deposition speed is increased, the temperature declines, resulting in higher flow stress and the flash formation at the consumable rod and not at the coating.

Somewhat contradictory to the argumentation above is the fact that the highest temperatures are reached for coatings generated in the high rotational speed regime, for which the flash is always formed at the rod. Because several other differences in behaviour are found for the two different regimes, which will be discussed in the following sections, it is obvious that a major change in deformation behaviour and material properties occurs between the rotational speeds of 1000 min^{-1} and 2000 min^{-1} for Ti-6Al-4V and 2000 min^{-1} and 3000 min^{-1} for Ti-Gr.1 (Figure 5.8 and Figure 5.10). As mentioned above, the flash formation at the coatings at a high rotational speed range (2000 min^{-1} – 6000 min^{-1}) was not observed. Several experiments with varying deposition speed were conducted to investigate the flash generation

at the coating. Low deposition speeds (4 mm/s, 8 mm/s and 16 mm/s) were used to achieve a high energy input, which usually lead to flash formation in the low rotational speed range, but this did not result in the flash formation at the coating in regime II (Figure 5.13). It can be seen that the energy input increased with decreasing deposition speed. This observation suggests a division of two rotational speed regimes. A low rotational speed regime is established in which the temperature has potential to increase, leading to low flow stress and therefore to flash formation at the coating. In contrast, a high rotational speed regime is defined where the temperature does not have the potential to rise and flash-free coatings are formed.
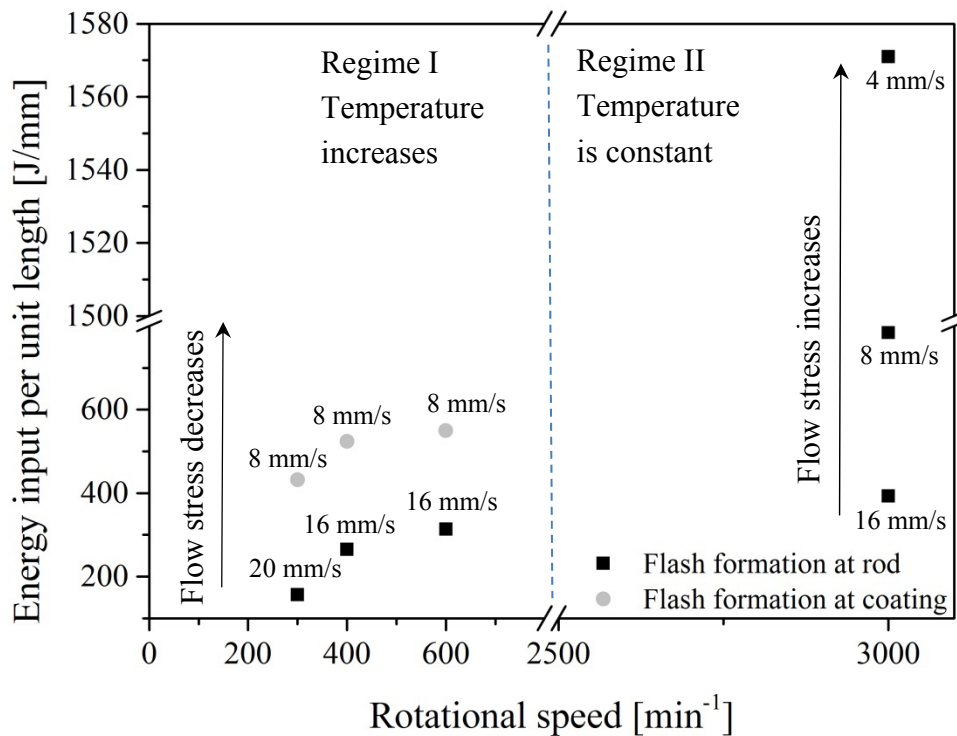

Figure 5.13: Energy input per unit length for various deposition speeds as a function of rotational speed with corresponding deposition speed placed above the dots for Ti-6Al-4V coatings; two different regimes can be identified.

Figure 5.14 demonstrates the influence of the deposition speed on the resultant axial force at a constant rotational speed with corresponding images of the Ti-6Al-4V coatings. It can be observed that the flash was formed at the coating when using an 8 mm/s deposition speed. When increasing the deposition speed to 12 mm/s and 16 mm/s the flash formation was precluded, which might be related to a corresponding decrease in temperature, as mentioned earlier. Moreover, the resultant axial force varies depending on the employed deposition speed. The axial force ascended (from ~ 10 kN to 27 kN) with increasing deposition speed. At the same time, the temperature decreased from 1286 °C to 1052 °C. It can be assumed that a decrease in temperature is caused by the ascent in deposition speed, leading to high flow

stresses, so the required axial force is much higher (26 kN) than at a low deposition speed (10 kN). The high axial forces required at a high deposition speed might be seen as material resistance against the deformation, resulting in flash-free coatings.
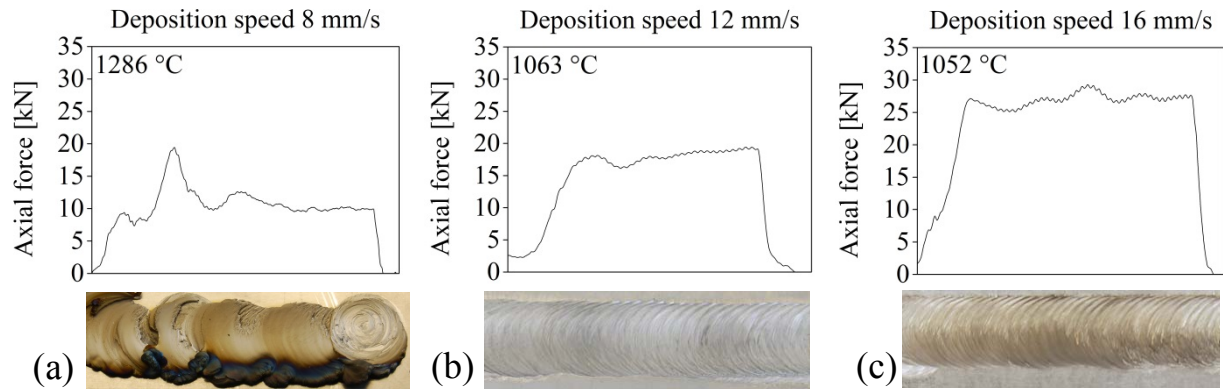

Figure 5.14: Axial force response with variation of the deposition speed when using a 400 min^{-1} rotational speed with corresponding temperature values and images of the produced Ti-6Al-4V coatings.
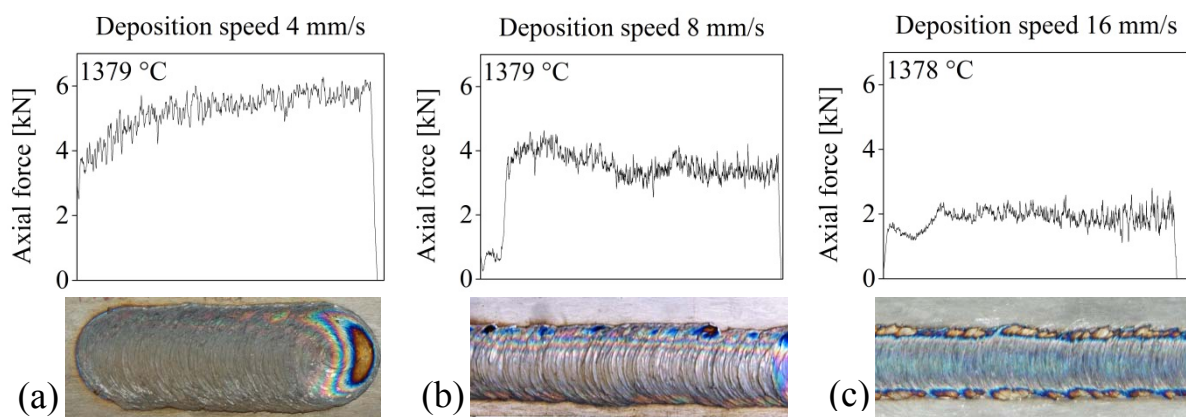

Figure 5.15: Axial force response with variation of the deposition speed when using a 3000 min^{-1} with corresponding temperature values and images of the produced Ti-6Al-4V coatings.

The effect of the deposition speed on the resultant axial force trend at a 3000 min^{-1} rotational speed with corresponding coating images is demonstrated in Figure 5.15. Three deposition speeds of 4 mm/s, 8 mm/s and 16 mm/s were employed to analyse the force behaviour. It can be seen that the force decreases from 6 kN to 2 kN with increasing deposition speed from 4 mm/s to 16 mm/s. This behaviour is contrary to the force evolution at 400 min^{-1} rotational speed which increases with deposition speed (compare Figure 5.14). No further increase in the measured temperature with decreasing deposition speed was observed at 3000 min^{-1}. The temperature remained constant at 1379 °C, 1379 °C and 1378 °C for deposition speeds of 4 mm/s, 8 mm/s and 16 mm/s, respectively. This indicates that the temperature evolution has

already achieved its maximum value for a solid state process, and there is no potential for further increase. However, because the temperature cannot be increased when employing a 4 mm/s deposition speed, the axial force increases due to the high strain applied per unit distance. The material at a constant rotational speed undergoes a higher number of rotations (higher strain) per unit of length at a 4 mm/s deposition speed compared with 16 mm/s. Therefore the material flow stress might increase, resulting in high forces (6 kN) at 4 mm/s compared with 2 kN at 16 mm/s. At a lower deposition speed, the prolonged plastic deformation time causes the formation of a large volume of plasticised material [45]. This prolonged plastic deformation time results in wide and thicker coatings.

The strain rate sensitivity is a crucial factor in the plastic deformation of titanium alloys. Strain rate sensitivity can be defined as the ratio of incremental change in stress (log σ) to the resultant change in strain rate (log $\dot{\varepsilon}$) at a given strain and temperature [51]. Furthermore, it has been reported that the strain rate sensitivity factor rises with increasing temperature and drops when increasing strain rate [84]. It is well known that titanium tends to display unstable flow behaviour during plastic deformation. It was concluded that the temperature and deformation induced by the FS process in the low rotational speed regime influence the flow stress behaviour of the titanium coatings. These instabilities could result in unstable material behaviour, forming flash at the coating.

Park et al. published the stress behaviour of Ti-6Al-4V alloy as a function of temperature (max. 1000 °C) and strain rate in hot forging experiments. The results indicate that the stress increases significantly with the strain rate at temperatures below β-transus. However, in a β-field at a temperature of 1000 °C, the stress values still increase with the strain rate but are much less than at low temperatures (Figure 5.16) [85]. Considering the temperature trend for FS, reaching temperatures up to 1304 °C in the high rotational speed regime, it might be assumed that the stress values are located even closer. Such close values will not significantly influence the flow behaviour at a constant temperature. In the low rotational speed regime, both the temperature and strain rate vary, which may lead to considerable changes of the flow stress values.

In conclusion, it can be said that the deposition of titanium coatings can be divided into two regimes regarding the employed rotational speed (Figure 5.13). In the low rotational speed regime where the temperature has the potential to increase with an increase in rotational speed or decrease in deposition speed, thermal phenomena seem to be a governing mechanism leading to thermal softening once a certain temperature value has been achieved. In the high rotational speed regime, the maximum temperature is achieved and thus cannot be raised by decreasing the deposition speed. The temperature does not have the potential to rise any further and has achieved a saturation state. Instead, the axial force is changing as a function of the deposition speed. Moreover, the combination of the high strain and strain rates and high

temperature may result in "stable" deformation behaviour at constant flow stresses, leading to deposition of flash-free coatings. Seshacharyulu et al. [19] carried out tensile ductility measurements to confirm the occurrence of the superplastic deformation in titanium alloy at 850 °C (Figure 5.17). The figure demonstrates stress values derived from the tensile test but it still gives an indication for titanium behaviour. In this context, it can be seen that the oscillating tensile elongation behaviour of the material depends on the temperature variation. It can be noted that in the temperature range of 1050 °C to 1100 °C (beta field), the ductility declines drastically [19]. This fact indicates that in the β deformation field, the material becomes less ductile with increasing temperature. During FS the rod undergoes process temperatures in the range of 1000 °C-1400 °C, therefore these fluctuations will influence the complex response of material during FS. Moreover, instabilities in flow stress have been reported by Seshacharyulu et al. for hot compression tests at a temperature of 1100 °C at relatively high strain rates. A stable flow stress behaviour at strain rates up to 1 s^{-1} has been reported, and the flow stress at a 100 s^{-1} strain rate oscillates significantly [17]. Furthermore, Meyers et al. reported plastic deformation behaviour of titanium in compression Kolsky bar experiments. The experiments were conducted at ambient temperature at high strain rates (from 900 s^{-1} to 7600 s^{-1}). In these experiments, titanium also exhibited fluctuating stress behaviour [86].
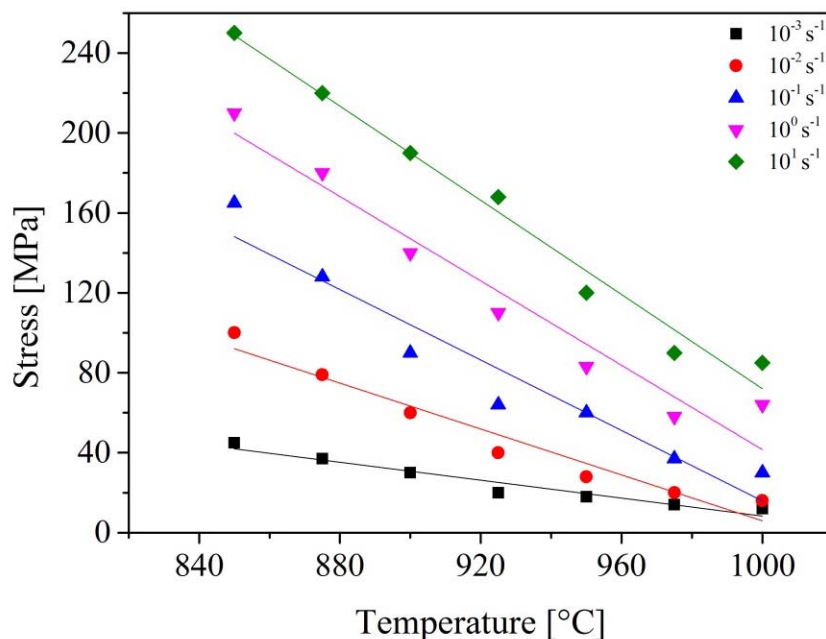

Figure 5.16: Influence of the strain rates and temperatures on the material stress behaviour of titanium according to Park [85].
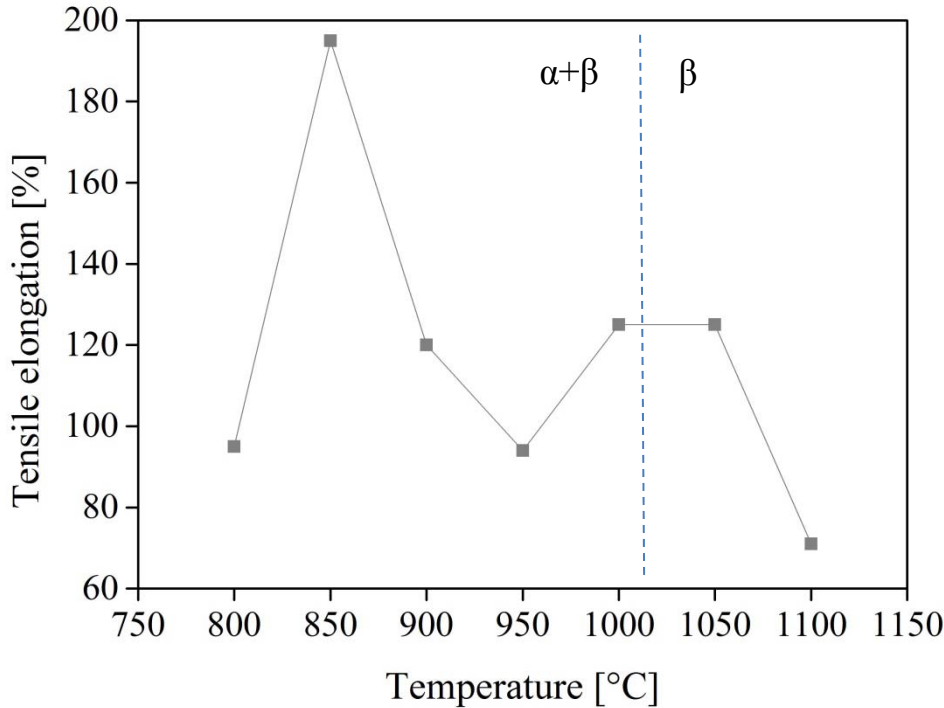
Figure 5.17: Influence of the temperature on the tensile elongation behaviour of Ti-6Al-4V according to Seshacharyulu [19].

Although the strain rates acting during friction surfacing can be assumed to be significantly higher than in the tensile tests, the process temperatures at low rotational speeds lie in the vicinity of 1100 °C. A change in the flow behaviour of the material at this temperature at sufficiently high strain rates seems to occur. No reference in the literature is available on severe plastic deformation of Ti-6Al-4V at the high strain rates and strains that take effect during friction surfacing, and further studies will be required for a comprehensive explanation of the flash formation behaviour observed in the present study.

Ti-6Al-4V and Ti-Gr.1 coatings can be deposited in an identical broad range of rotational speeds. However, the region of flash formation occurrence for Ti-Gr.1 (400 min^{-1}-2000 min^{-1}) is broader than that for Ti-6Al-4V (700 min^{-1}-1000 min^{-1}). Because the flash formation depends on the material flow stress, the reason for the different regions of flash occurrence might be related to the different material strengths of both alloys at the occurring temperatures.

5.2.3   Summary of Two Acting Regimes

It has been demonstrated in the current work that titanium alloys during friction surfacing exhibit two different rotational speed regimes, in which different mechanisms act. In the regime model presented in the following, the mechanisms are schematically demonstrated (Figure 18). To simplify the model a constant value of the rotational speed for each regime is

considered. The most important factor for the model is the resultant temperature, which varies in regime I and remains nearly constant in regime II, affecting the material flow behaviour during friction surfacing.

- In the regime I (low rotational speeds), the temperature (T) changes with rotational speed. The variation of deposition speed (v) at a constant rotational speed also leads to alterations in temperature. Generally, a constant rotational speeds and low deposition speeds (high energy input due to the longer process time) cause an increase in the measured temperature. Such high temperatures consequently result in lower flow stresses (σ), which can be seen from decreasing values of the resulting axial force (F). Still, the axial forces in this regime are rather high, the coatings obtained are relatively thin, and the rod tip after depositing a coating shows that only a thin layer of material was plasticised. Since the rod material is fed into the process zone at a constant rate (1.6 mm/s), the presence of only a small volume of plasticised material results in high axial forces, as this softened material is pushed out from the contact and is deposited behind the moving rod. Increasing the rotational speed or reducing the deposition speed can increase the achieved temperatures and plasticised material volume and thereby decrease the resulting force. At very low deposition speeds, the shear layer at the rod tip can form in such a way, that the flash, which is normally formed and pushed up around the rod, is deposited together with the actual coating layer. This behaviour occurs when the deposition speed is reduced below a certain value, which varies for each rotational speed. The common feature for parameter combinations leading to flash formation at the coatings is that the generated energy input is very high. Possibly, for each rotational speed, a threshold value exists for the deposition speed, below which the shear layer reaches a thickness that includes the position at which the flash material is formed.

- In the regime II (high rotational speeds), the temperature does not alter with varying rotational speed or deposition speed. The torque (τ) values also remain relatively constant for the various parameter combinations investigated in this study. Only axial force values vary, which overall are an order of magnitude lower than those in the low rotational speed regime. Obviously, in this regime, the process temperatures reach a maximum and cannot be further increased by additional energy input. Thus, the constant torque values, which can be assumed to be related to the shear stresses acting in the deforming shear layer, seem to be mainly influenced by the material temperature and not by the deposition speed, which change with varying process parameters. When using a low deposition speed in this regime, the material undergoes a prolonged plastic deformation time and consequently a high strain, which causes the formation of a large volume of plasticised material. The decrease in deposition speed does not lead to a drop in axial force, as is the case in the low rotational speed regime,

but instead results in an increase in axial force. This can be correlated with the fact that the coating thickness also increases significantly, so a larger amount of material is sheared off the rod and deposited onto the substrate. In this regime, the flash is exclusively generated at the rod.
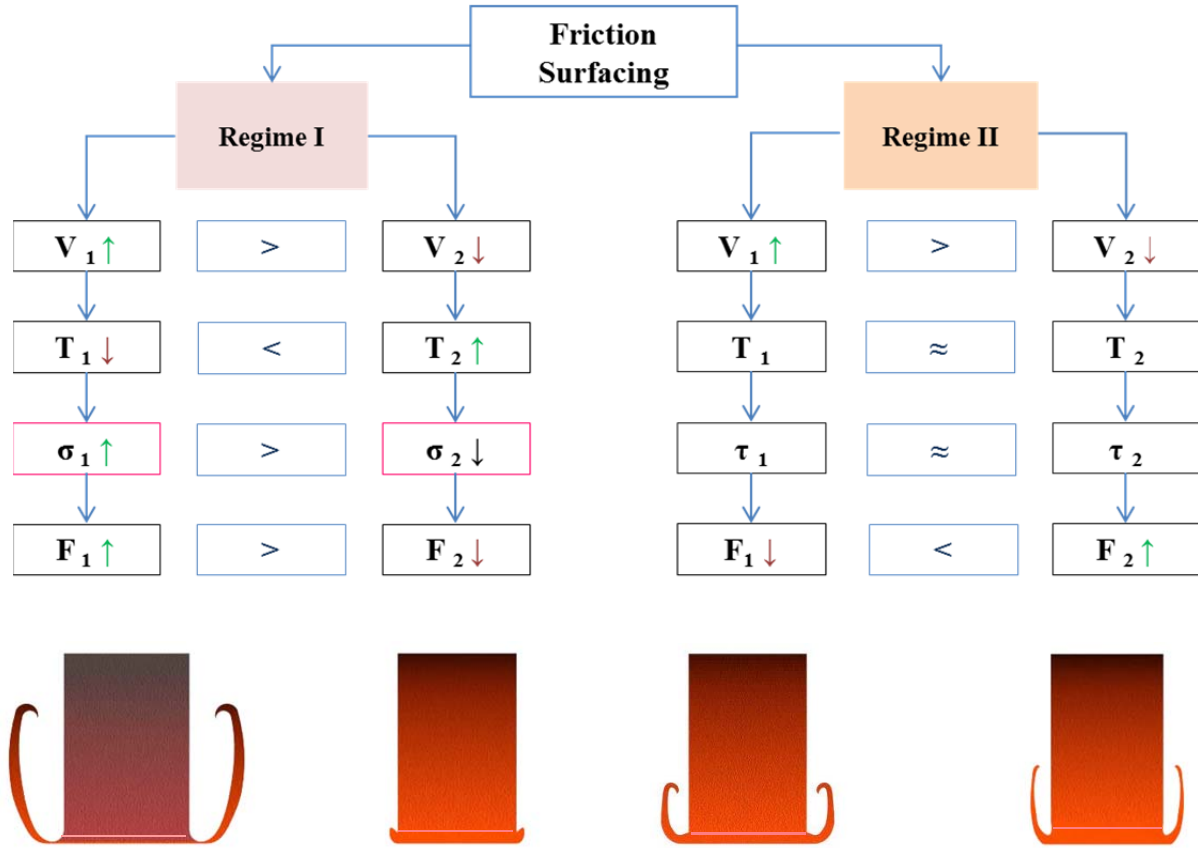

Figure 18: Model of regime I and regime II with the corresponding flash formation. The differences in red contrast of the rods refer to their temperatures. The structure at the rod tip indicates the different shear layer thicknesses.

5.3   Temperature Analysis

Infrared Camera

The emission factor ε was determined to vary between 0.75 and 0.89 for the Ti-6Al-4V and Ti-Gr.1 coatings depending on the individual temperature, in the range of 800 °C to 1300 °C. The IR camera was placed in front of the FS machine and focused at the rod tip, enabling recording of the rod heating rate and the temperature in the process zone, also during cooling. The thermal images were captured at 20 frames per second and at a frequency of 80 Hz.

The heating rate was determined for the conducted experiments. It has been observed that the heating rate varies with rotational speed. The heating rate for Ti-Gr.1 was determined for three different rotational speeds. When a low rotational speed (300 min^{-1}) is introduced, the heating rate is low (216 Ks^{-1} ± 19 Ks^{-1}) and leads to a peak temperature of 971 °C, because a low rotational speed necessitates more time to generate the energy required for the plastification phase. In comparison, when high rotational speeds are employed (3000 min^{-1} and 6000 min^{-1}), heating rates of 404 Ks^{-1} and 389 Ks^{-1} are observed, respectively. This means that the peak temperature during the process at high rotational speeds is rapidly achieved in approximately 3 s. The process temperature exceeded the β-transus temperature in all experiments. The peak temperature achieved the steady-state condition while processing, and no temperature alteration was observed during deposition. A similar temperature distribution has been reported when depositing copper and tool steel. Once the transversal movement is superimposed, the temperature attains a steady-state condition. The heating rate for copper and tool steel is lower than that for titanium alloys [87]. The discrepancies in the heating rate might be derived from different physical properties of the material, particularly the low thermal conductivity of titanium. Furthermore, it can be concluded that the process temperature in FS cannot be suppressed below the β transformation temperature within the wide range of rotational speeds investigated in the current study. A thermal image captured during the process displays the temperature distribution at the rod tip and in the coating (Figure 5.19). The colour scale represents the corresponding temperature level. The highest temperature measured in the process zone was 1377 °C, and the earliest cooling stage of the coating behind the rod exhibited a temperature of 1180 °C.
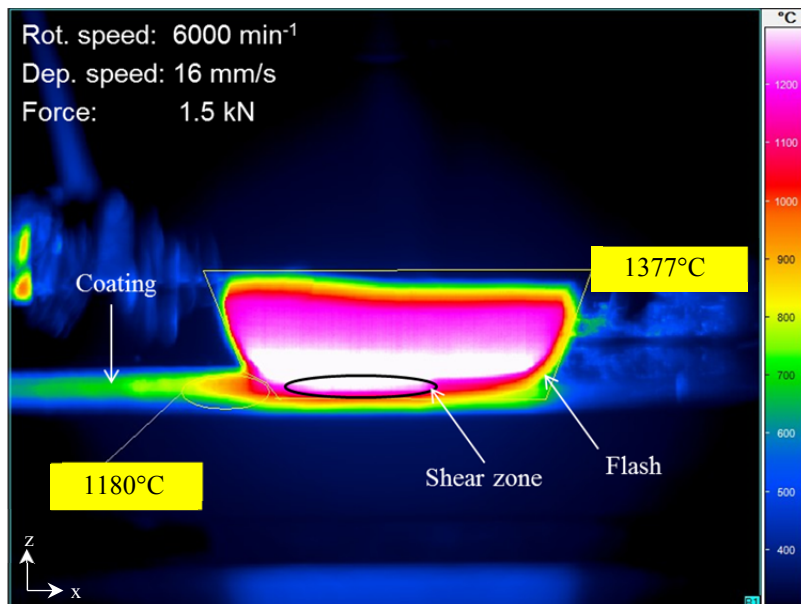

Figure 5.19: Temperature distribution measured by an IR camera during the process indicating the temperature in the process zone and at the coating behind the rod (in the initial cooling stage).

Experiments demonstrating the temperature evolution as a result of the rotational speed for Ti-6Al-4V and Ti-Gr.1 coatings are presented in Figure 5.20. For both alloys, an increase in temperature with rotational speed can be observed first, in which the temperature reaches its maximum at 3000 min^{-1} for Ti-Gr.1 and at 2000 min^{-1} for Ti-6Al-4V. Following this, the temperature reaches a plateau and remains constant with increasing rotational speed. It is remarkable that the temperature for both alloys achieves its maximum at that rotational speed where the flash formation at the coatings is precluded. This fact correlates very well with the flash formation hypothesis presented in section 5.2 showing that a change in deposition speed affects the temperature only in regime I.
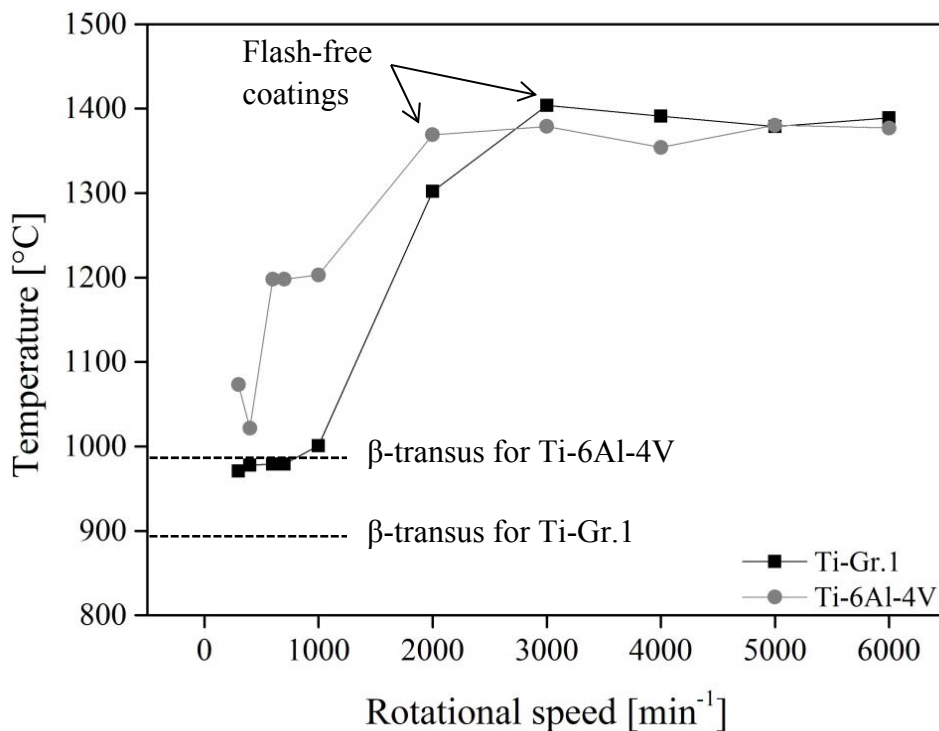

Figure 5.20: Temperature evolution measured at the process zone of Ti-6Al-4V and Ti-Gr.1 coatings as a function of the rotational speed.

Thermocouple Measurements

The maximum temperature and cooling time were recorded at the interface of the Ti-6Al-4V coating generated at 3000 min^{-1} as demonstrated in Figure 5.21. The two thermocouples measured maximum temperatures of 1169 °C and 1239 °C. The cooling rates were calculated from the maximum temperature down to 200 °C. The two thermocouples measured cooling rates of 46.4 Ks^{-1} and 43 Ks^{-1}. At both cooling curves, a kink at approximately 800 °C was observed. This temperature range correlates with the martensite start temperature (800 °C) [9].
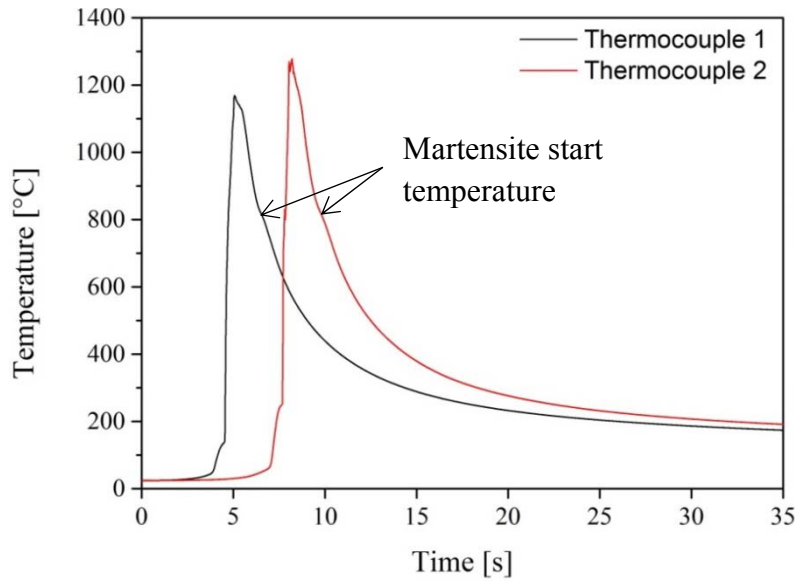
51

Figure 5.21: Maximum temperature and cooling until 200 °C recorded at the interface of Ti-6Al-4V coatings generated at 3000 min^{-1}. A kink in both curves demonstrates the beginning of martensite transformation at ~ 800°C.

The temperature measurements employing thermocouples demonstrated differences compared with those employing the IR camera. Measurements by thermocouples were carried out at the coating interface; during the IR camera investigation, temperatures from the entire process zone were captured. Moreover, the exact location of the measurement point is unknown, which might lead to different values. These temperature differences might also be related to the placement height of the thermocouples on the substrate. To examine the exact position of the thermocouples, cross sections were prepared. Figure 5.22 shows the actual position of a thermocouple at the interface between the substrate and coating in the cross section of a sample after deposition.
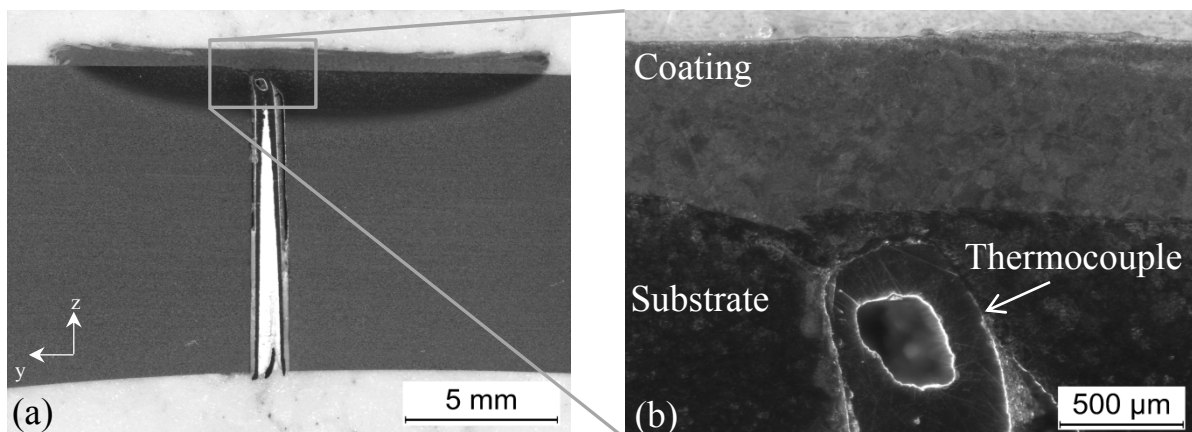

Figure 5.22: A cross section showing the precise thermocouple location at the Ti-Gr.1 coating/substrate interface generated at a 6000 min^{-1} rotational speed, a 16 mm/s deposition speed and a 1.6 mm/s consumption rate (a) and image with high magnification (b).

It can be observed that the thermocouple is located slightly beneath the coating. During the deposition it is pushed into the heated substrate. Moreover, it can be seen that the thermocouple tip was not covered directly by the coating but rather by the deformed substrate material.

5.4   Characterisation of the Deposited Coatings

In this section the coating geometry and deposition efficiency of Ti-6Al-4V and Ti-Gr.1 will be presented and discussed. Each section presents results for Ti-6Al-4V and Ti-Gr.1 coatings separately.

5.4.1   Coating Geometry

As previously discussed the coatings can be deposited in a wide range of process parameters, which can be divided into two groups corresponding to the rotational speeds. Compared with other materials [45], titanium coatings can be deposited with relatively low axial forces (1 kN) in a high rotational speed range and with a wide range of process parameters. However, the process parameters have an influence on the layer quality and geometry [36]. To further analyse the effect of rotational speed on the coating geometry, coatings without flash formation are exclusively discussed herein.

Ti-6Al-4V Alloy Coatings

The surface appearance of four selected coatings deposited at rotational speeds of 400 min^{-1}, 600 min^{-1}, 3000 min^{-1} and 6000 min^{-1} is presented in Figure 5.23. At low rotational speeds (300 min^{-1} and 600 min^{-1}), smooth layers without oxidation were produced (Figure 5.23 a, b), whereas at high rotational speeds (3000 min^{-1} and 6000 min^{-1}, Figure 5.23 c, d), layers with a rough surface were deposited, displaying annealing colours.

The widths of some coatings vary along the layer. Figure 5.23 c demonstrates a coating generated at 3000 min^{-1}, which exhibits fluctuations in the width at regular intervals of 3 mm along the coating length. These width fluctuations are linked to the simultaneous occurrence of oscillations in the resultant axial force, as shown in Figure 5.24 a, b. High force peaks result locally in a wide coating width and low force peaks result in a narrow coating width.

The layer geometry was investigated by cross section macrographs. Several cross section images of the coatings that were generated at different rotational speeds are presented in Figure 5.25. It can be noticed that the coating thickness differs from the advancing side to the retreating side. The cross sections also show an inhomogeneous coating thickness, with an insufficient amount of material deposited at the RS compared with the AS, when low rotational speeds were utilised (Figure 5.25 a, b).

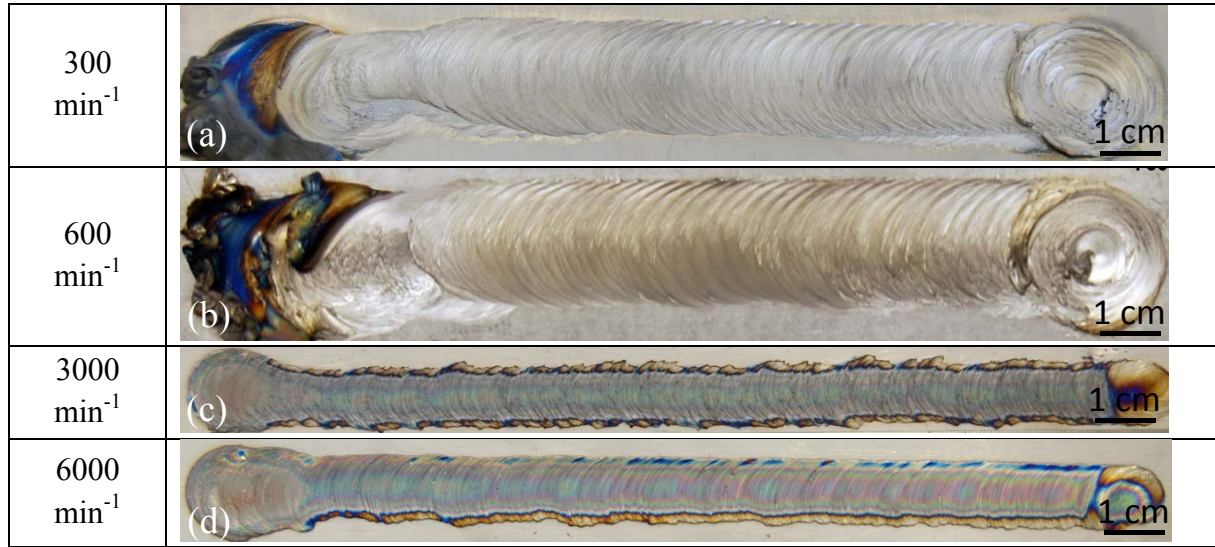| 300 min^{-1}	
600 min^{-1}	
3000 min^{-1}	
6000 min^{-1}	

Figure 5.23: Surface appearance of the Ti-6Al-4V layers when using a deposition speed of 16 mm/s and a consumption rate of 1.6 mm/s in conjunction with four different rotational speeds.
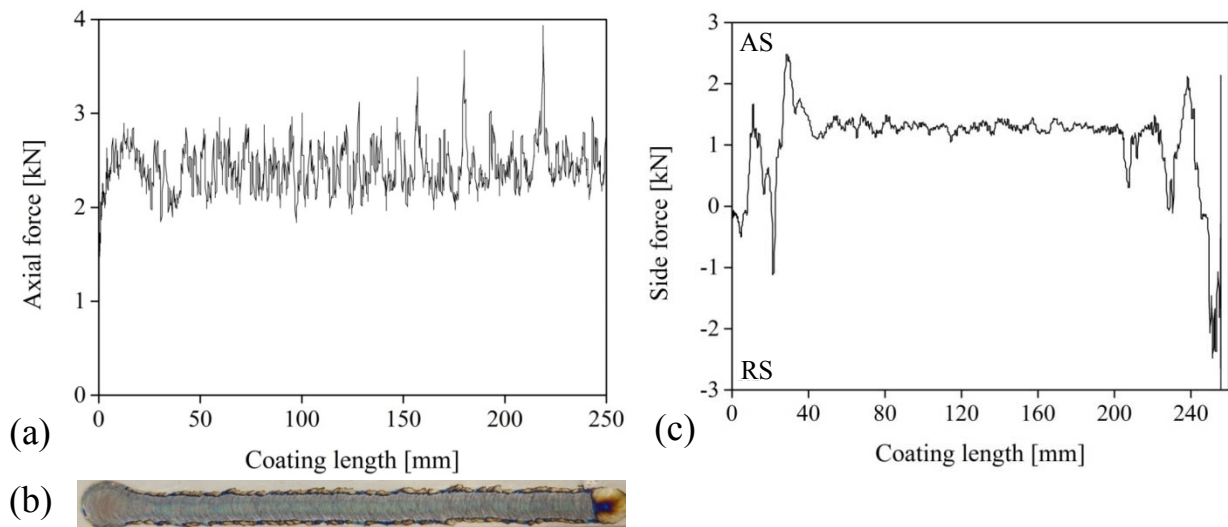

Figure 5.24: Homogeneous layer deposited with consumption rate control (3000 min^{-1} rotational speed, 16 mm/s deposition speed and 1.6 mm/s consumption rate) with variations in the layer width (b) that are attributed to fluctuations in the axial force (a). Record of the side force (F_y) data implying a rod displacement to the advancing side (c).

Figure 5.25 a shows the thinnest measured coating with a minimum layer thickness of 478 µm. It can be seen that coatings are not perfectly bonded at the edges. This is a result of the inhomogeneous pressure applied between the centre and the edges of the rod. This effect is typical for the coatings produced by FS [29]. No voids were observed in the centre of the

layer. It must be pointed out that the selection of low rotational speeds for deposition leads to rather thin coatings with a marginal amount of material at the RS. When observing the force data in the direction of the coating width, it can be seen that force values are displaced in the direction of the AS (Figure 5.24 c). This means that the consumable rod was tilted to the AS with 1.5 kN, which can be related to the material behaviour (high flow stresses) at low rotational speeds with high required axial forces (26 kN), as discussed in subsection 5.2.2. In contrast, coatings produced at high rotational speeds present a homogeneous coating thickness at both sides (AS and RS) (Figure 5.25 c, d).
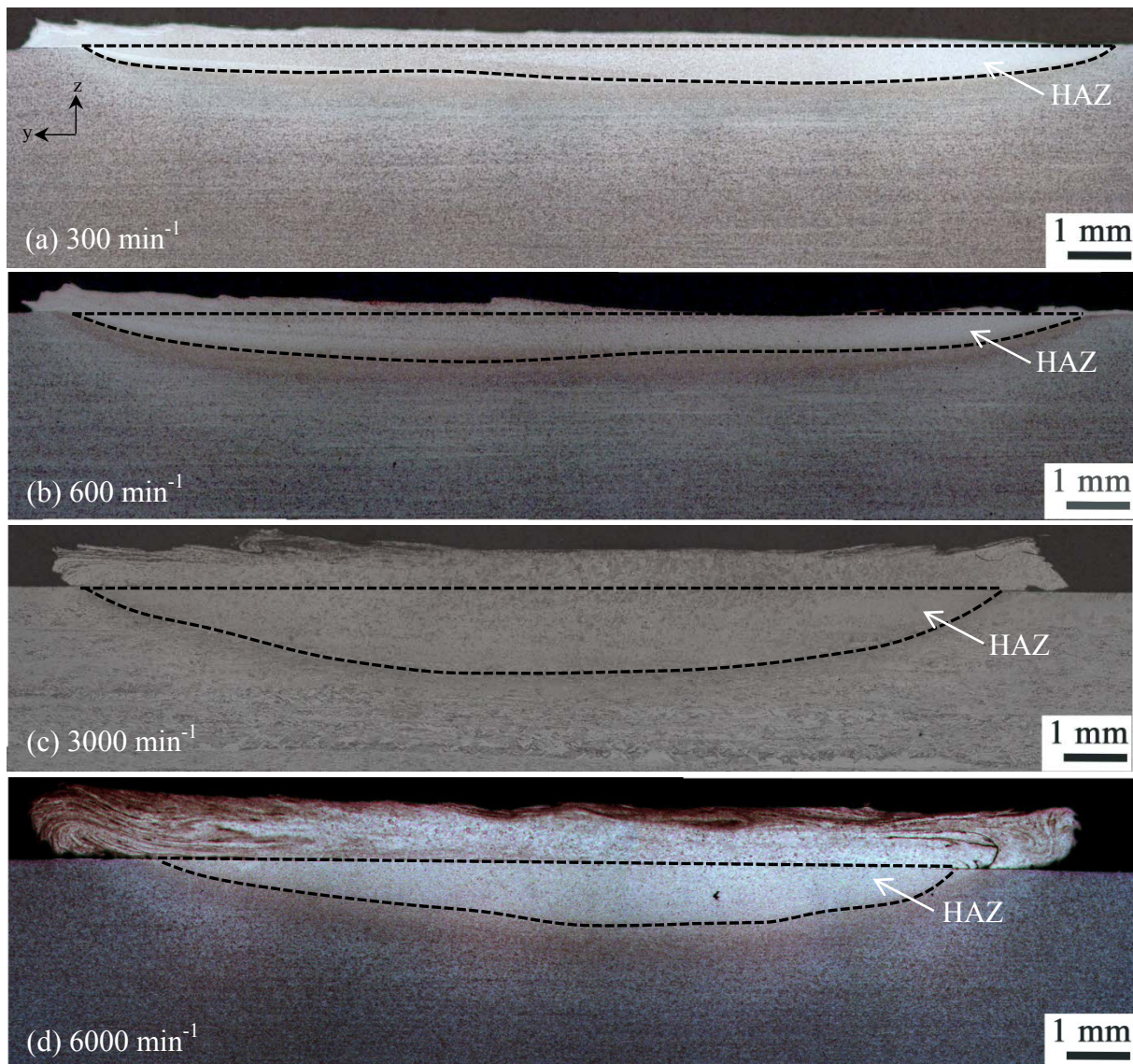

Figure 5.25: The cross section of the Ti-6Al-4V depositions at various rotational speeds with the HAZ indicated by black lines; thin layers (a, b), thick layers (c, d).

Moreover, the effect of the heat generation on the substrate can be seen in the HAZ (Figure 5.25). All images demonstrate a crescent-shaped HAZ with a maximum depth in the centre,

which can be correlated to an unequal distribution of the frictional heat across the rod's radius. On the one hand, different degrees of pressure are effective, due to the material flow during the process [29]. Further, the duration of the interaction between rod and substrate varies across the rod radius perpendicular to the direction of the deposition speed, for geometrical reasons. The depth of the HAZ varies with the rotational speed and associated temperature. Moreover, the temperature distribution is different within the coating width, exhibiting a maximum temperature in the middle of the coating, as reported for aluminium alloy AA6082 coatings [88]. The visible border between the HAZ and the base material is the isotherm, above which the microstructure changes and below which is the unaffected base material. Coatings produced in the low rotational speed regime demonstrate a shallower HAZ depth compared with the HAZ of coatings produced in the high rotational speed regime. When increasing the rotational speed, the majority of the plastic power transfers into heat, locally increasing the temperature. This increased temperature leads to a deep HAZ.

Individual measurements at the coatings were taken to analyse the effect of the rotational speed on the layer thickness, the total coating width and the bonded width. The results of the measurements are presented in Figure 5.26. For determination of the coating geometry, three samples per coating were prepared, and a scatter in the range of ± 5 % was found for all geometry measurements. All of these cross-sectional images showed a layer width below the rod diameter (20 mm). It can be observed that an increase in the rotational speed leads to increased coating thicknesses and narrower coating widths. A similar behaviour with regard to coating width has been observed by Rafi et al. by depositing tool steel H13 coatings [36]. The influence of the rotational speed on the coating width has been demonstrated. It has been shown that a low rotational speed (800 min^{-1}) resulted in a wider coating with an 18 mm width, and a high rotational speed (2400 min^{-1}) resulted in a narrow coating width (10.5 mm) [36].
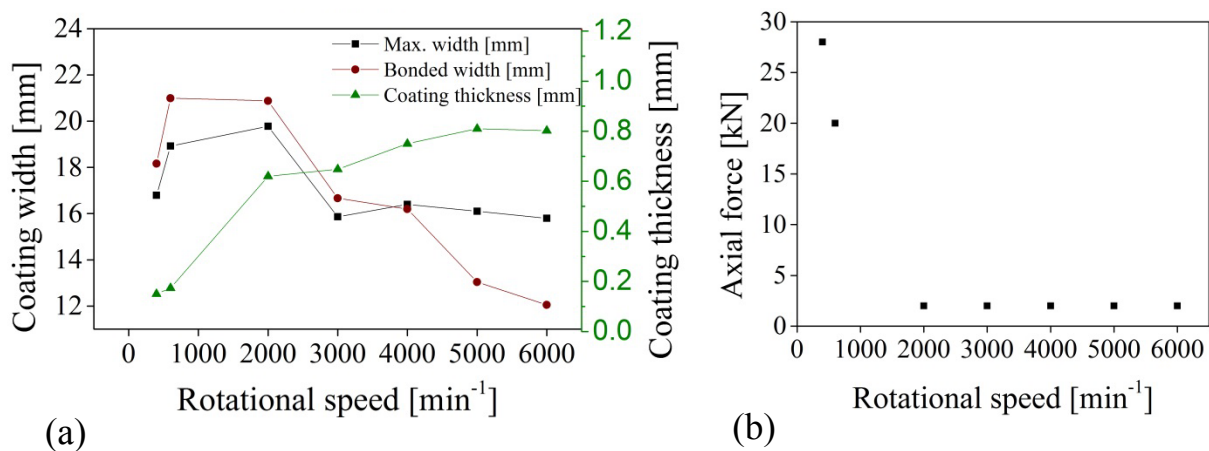

Figure 5.26: The effects of the rotational speed on the Ti-6Al-4V coating thickness and on the bonded and maximum coating widths (a). Resultant axial force vs. rotational speed (b).

The coating geometry at a certain rotational speed in the current work is related to the resultant axial force values during the process. The force values decline with increasing rotational speed from 29 kN to 1 kN (Figure 5.26 b). It can be assumed that when using a low rotational speed less heat is generated from plastic deformation, so relatively low temperatures are developed. This results in high flow stress and high axial forces are needed to plasticise the shear layer. These high forces squeeze the material from the process zone into the flash, leaving a wide and thin coating on the substrate. When employing a high rotational speed, more heat is generated leading to high temperatures, and correspondingly only low axial forces occur while processing. These low axial forces preclude the "squeezing out" of the material, increasing the shear layer thickness and therefore resulting in thicker and narrower coatings.

This interaction of the axial force and coating geometry has been reported by Gandra et al. for mild steel coatings produced by a constant rotational speed and varying axial force [42]. It has been shown that the coating geometry becomes wider and thinner with increasing axial force [42].

Evaluation of the Shear Layer at the Rod

To correlate the coating thickness to the shear layer formed at the tip of the consumable rod were analysed in the post-FS condition. The longitudinal section image of a consumable rod from the experiment with 400 min^{-1} is presented in (Figure 5.27). The shear layer exhibits a thickness of 600 μm.
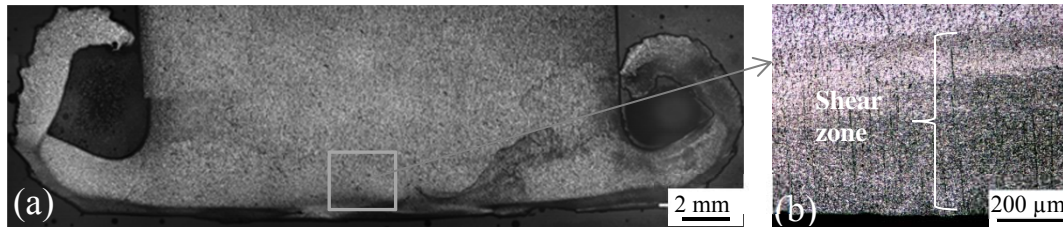

Figure 5.27: Longitudinal image of a consumed Ti-6Al-4V rod employing a rotational speed of 400 min^{-1} (a), and an image showing the shear zone (b).

The longitudinal sections of the rod from the experiments with 3000 min^{-1} and different deposition speeds with various resultant axial forces are presented in Figure 5.28. All images exhibit flash formation around the rod. The heat-affected zone did not undergo deformation but was temperature affected because of the heat conduction. The shear zone was heavily deformed. The shape of the consumed rods differs, exhibiting a concave rubbing area at a 2 kN force and a convex rubbing surface at 4 kN and 6 kN (Figure 5.28 a, b, c). The shape of the rubbing surface correlates very well with the coating thicknesses, which are derived from the axial forces. When a high axial force (≥ 4 kN) is applied, the shape of the rod is convex because the axial force presses the material out of the process zone. When low axial forces are

employed (~ 2 kN), the material flow out of the contact is decreased, leading to a coating width less than the diameter of the rod and a concave shape of the rod tip.
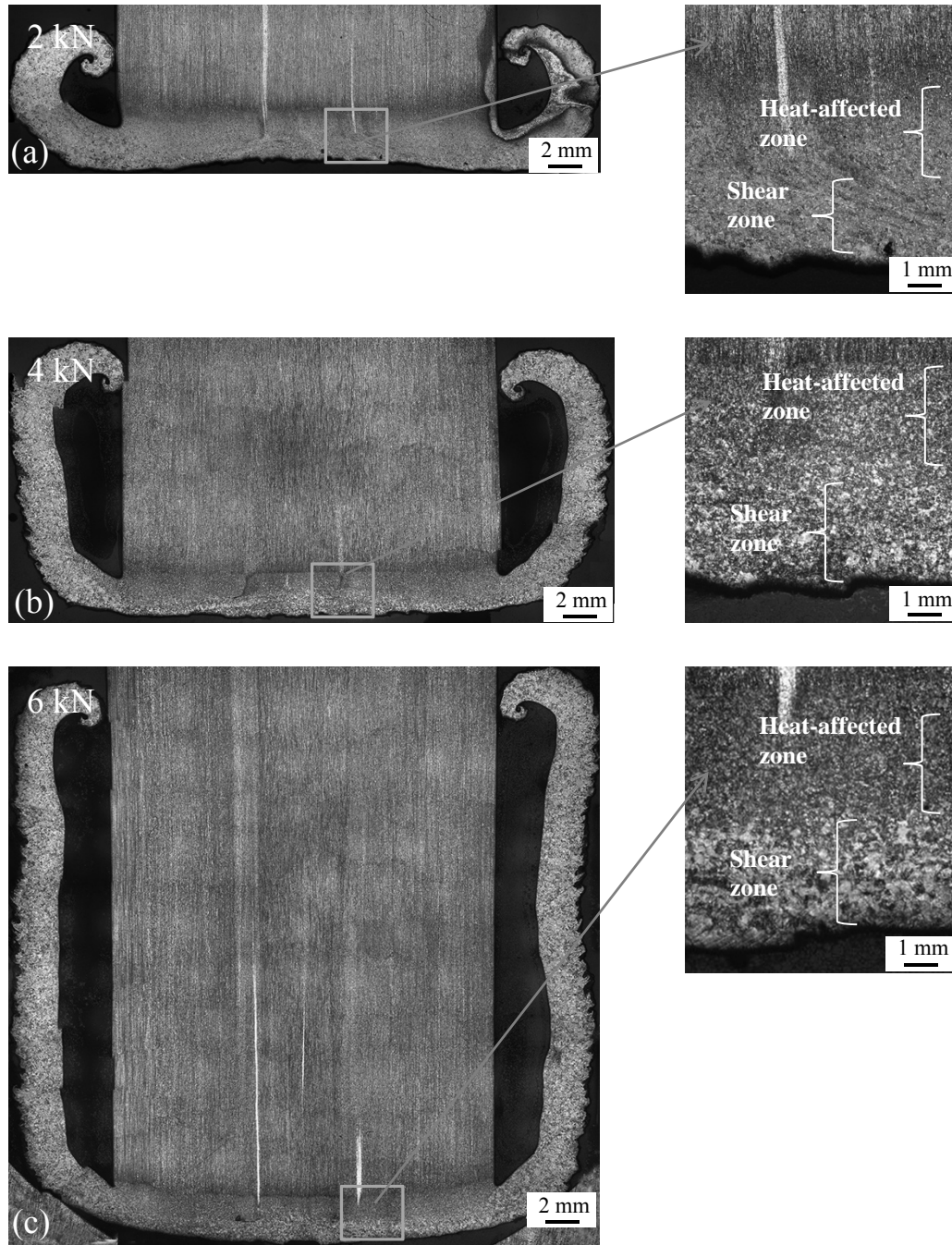

Figure 5.28: Longitudinal images of the consumed Ti-6Al-4V rods employing deposition speeds: (a) 16 mm/s, (b) 8 mm/s and (c) 4 mm/s. The thickness of the shear layer varies with deposition speed which can be seen in the images with high magnification.

The height of the flash depends on the experiment duration and becomes higher with increasing length of the coating layer. Three microstructure zones can be identified from Figure 5.28. The unaffected region of the base material presents a typical microstructure with

elongated grains. The heat-affected zone of the base material into the shear layer is visible. The shear layer can be observed with different heights. The height of the shear layer is a function of the rotational speed, deposition speed and temperature and correlates very well with the corresponding coating thickness. Within the shear zone, a martensitic microstructure is formed. Moreover, the microstructure of the consumed rods with regard to grain size evolution correlates well with the grain size observed in the coatings (1.64 µm ± 1.33 µm). The thickness of the shear layer is an effect of the deposition speed. It can be observed that the shear layer thickness increases from 1.47 mm to 1.91 mm with a declination in deposition speed. A possible explanation for this might be the dwell time of the rod on substrate.

Stop Action Experiments

Furthermore, stop action experiments were conducted, during which lifting off the rod at the end of the deposition was precluded. The coating and the consumable rod have been cooled with liquid nitrogen during the final rotation of the rod. The motive for these experiments was to observe the frozen condition during the process with the hope of being able to preclude static grain growth by the extreme cooling of the coating. A longitudinal section of the consumable rod welded onto the substrate is demonstrated in Figure 5.29.
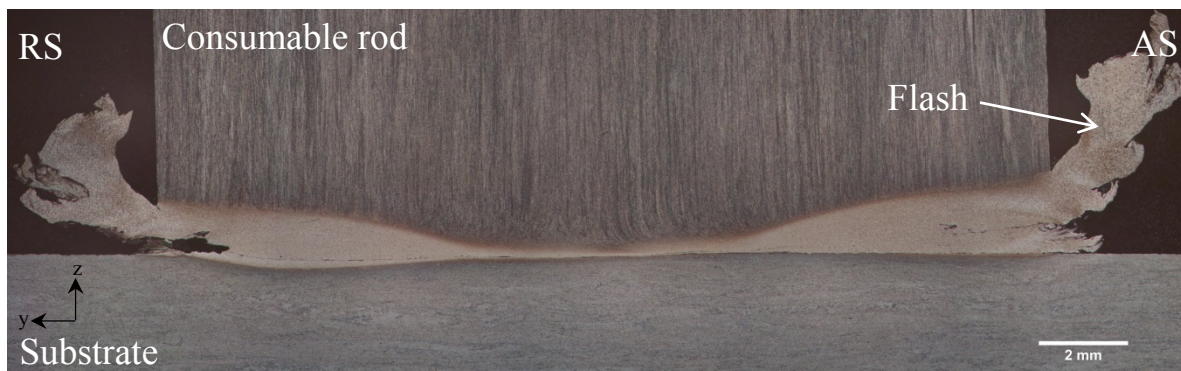

Figure 5.29: Ti-6Al-4V rod welded onto the substrate by the stop action procedure and cooled with the liquid nitrogen. Process parameters: 400 min^{-1} rotational speed, 16 mm/s deposition speed and 1.6 mm/s consumption rate.

The shear layer between the consumable rod and the substrate can be seen. The shear layer is not continuous over the rod's cross section, exhibiting a U shape. Investigation of the shear layer form did not reveal any differences for the conventional experiments by air cooling. The microstructure of the shear layer exhibits a grain size of 1.8 µm ± 1.7 µm, which is similar to the grain size of the coatings generated by conventional cooling in air. The reason for this might be the fact that when the stop action was executed by a process abort, the consumable rod still rotated, and the process did not instantly stop due to the inertia of the driving device, which still resulted in high temperatures. Additionally, perhaps the amount of liquid nitrogen was insufficient to cool the rod. Moreover, it can be seen that the shear layer is predominantly

formed at the AS, exhibiting a clear line between the coating and shear layer with squeezed flash. At the RS, an insufficient amount of the coating was transferred, revealing a gap. Considering the different occurrences of the material transfer from the consumable rod to the substrate at both sides (AS and RS), it might be assumed that the flash formation of the coating RS might occur similarly. Presumably, the lower thickness of the layer on the RS might lead to the flash formation of the coating, which was observed in subsection 5.1.2.

Ti-Gr.1 Coatings

The titanium Gr.1 deposits produced at various rotational speeds (300 min^{-1}, 3000 min^{-1} and 6000 min^{-1}) were employed to investigate the influence of the rotational speed on the coating geometry. The deposits exhibit varying visual appearance (Figure 5.30). Similar to Ti-6Al-4V alloy coatings, it can be observed that pure titanium coatings generated at 300 min^{-1} exhibit a smooth surface appearance, and no oxidation colours are visible, due to the lower process temperature and thin coating thickness resulting in faster cooling rates. In contrast, both other coatings produced at high rotational speeds present rather rough surfaces with a welding bead structure typical of FS coatings.
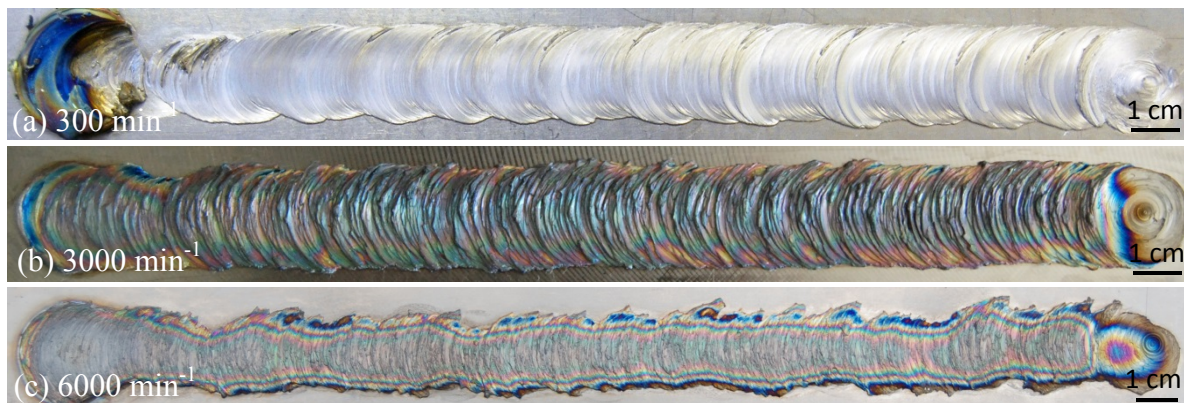

Figure 5.30: Surface appearances of the Ti-Gr.1coatings generated at a deposition speed of 16 mm/s and a consumption rate of 1.6 mm/s in conjunction with three different rotational speeds.

The cross sections of the presented coatings were prepared to investigate their geometry in detail (Figure 5.31). The coating produced at 300 min^{-1} exhibits the lowest thickness. This low coating thickness is related to the high force (25 kN), similar to the previous explanation for Ti-6Al-4V coatings. This high axial force is a result of the required consumption rate of 1.6 mm/s. The coatings produced at 300 min^{-1} and 6000 min^{-1} demonstrate lower surface roughness compared with the coating produced at the 3000 min^{-1} rotational speed.

The effects of the rotational speed on the layer thickness, the total coating width and the bonded width are presented in Figure 5.32. It can be seen that the coating thickness increases substantially from the low rotational speed (300 min^{-1}) to the high rotational speed

(3000 min^{-1}) from 0.4 mm to 1.1 mm and slightly declines with a further increase in rotational speed to 0.75 mm at 6000 min^{-1}. The increase in coating thickness is related to the lower axial force value achieved at a 3000 min^{-1} rotational speed (Figure 5.32 b). The coating width and thickness do not show a clear pattern depending on the rotational speed.
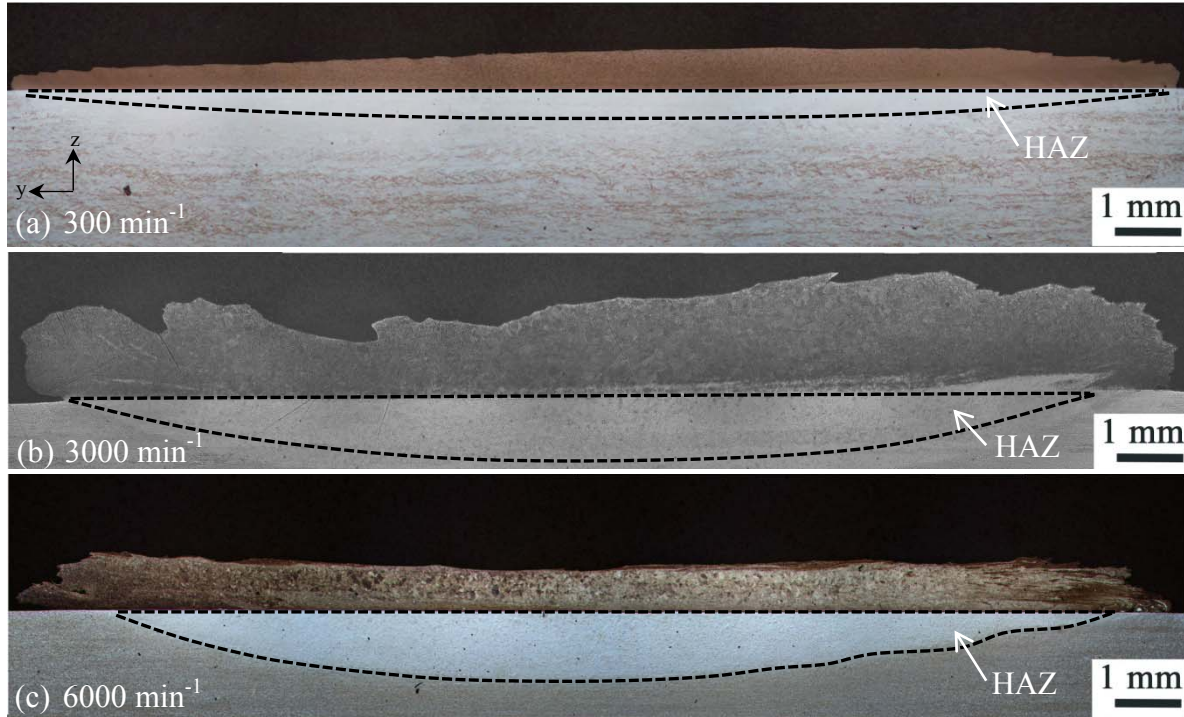

Figure 5.31: The cross section of the Ti-Gr.1 depositions at various rotational speeds with the heat-affected zone indicated by black lines; thin layers (a) thick layers (b, c).
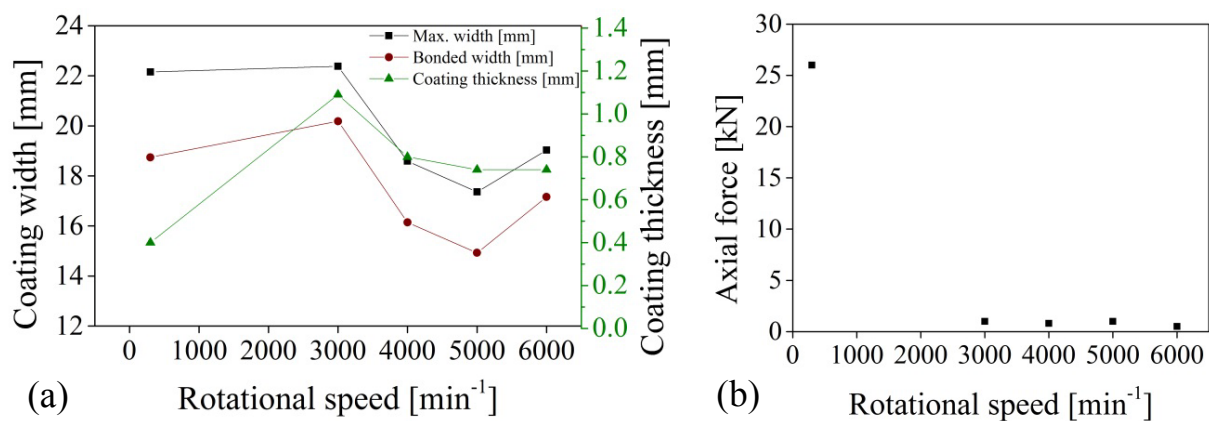

Figure 5.32: The effects of the rotational speed on the Ti-Gr.1 coating thickness and on the bonded and maximum coating widths (a). Corresponding axial forces for different rotational speeds (b).

Additional experiments were carried out to investigate the correlation between deposition speed and coating thickness. The deposition speed was varied in the range from 16 mm/s to 48 mm/s in 8 mm/s increments to show its effect on the coating thickness. The deposition speed was plotted against coating thickness for two rotational speeds (3000 min^{-1} and 6000 min^{-1}), as presented in Figure 5.33.
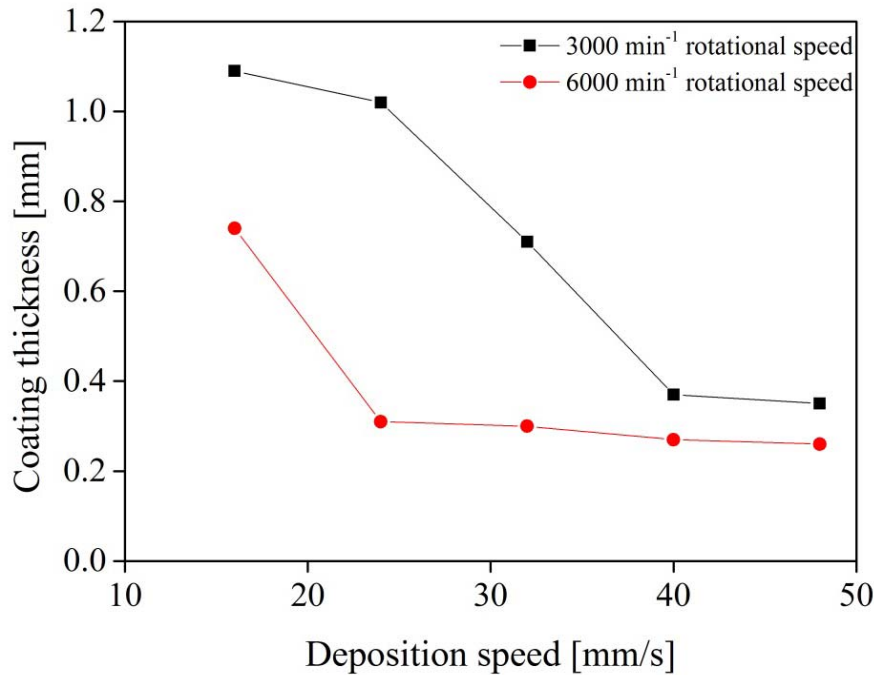

Figure 5.33: Effect of deposition speed on Ti-Gr.1 coating thickness at 3000 min^{-1} and 6000 min^{-1} rotational speeds.

For coatings produced at 3000 min^{-1}, the coating thickness is in the range between 0.35 mm and 1.1 mm, and for coatings produced at 6000 min^{-1}, it ranges from 0.28 mm to 0.74 mm. It can be seen that at the 3000 min^{-1} and 6000 min^{-1} rotational speeds, the coating thickness remarkably decreases with increasing deposition speed until reaching 40 mm/s and 24 mm/s, where the coating thickness does not vary. Generally, it can be stated that the coating thickness can be controlled within a certain range by varying the deposition speed. In the current results, an increase in deposition speed leads to a decrease in coating thickness.

In contrast to Ti-6Al-4V, titanium Gr.1 coatings exceeded the rod diameter for rotational speeds of 300 min^{-1} and 3000 min^{-1}. Moreover, the coating thickness of the pure titanium coatings is higher than that of Ti-6Al-4V coatings. This may be explained by the low material strength of pure titanium compared with Ti-6Al-4V. Even at elevated temperatures, the material strength might be slightly lower, resulting in a lower flow stress that can lead to the generation of a thick shear layer and thus wider and thicker coatings.

5.4.2 Deposition Efficiency

As shown in the previous subsection, the rotational speed affects the coating geometry, resulting in various coating widths and thicknesses. This leads to the conclusion that the amount of material loss (flash formation at the consumable rod) must also be consequently affected by the variation in the rotational speed. This would also imply that the deposition efficiency of the process must be influenced by the variation of the rotational speed.

The deposition efficiency of the materials is defined as the ratio of the deposited volume to the consumption volume of the rod and can be calculated, as follows [42]:

$$\eta_{deposition}(\%) = \frac{Deposited\ volume}{Consumption\ volume\ of\ the\ rod} * 100\% \quad \text{Eq. (3)}$$

The deposited volume is the product of the cross-sectional area of the coating thickness and the deposited coating length. The consumption volume of the rod is the product of the rod cross-sectional area and the consumed rod length. To accurately determine the deposition efficiency of the coatings with flash formation, a section without the flash formation must be selected, because the flash cannot be considered as effective deposition. Coatings with a homogeneous geometry were exclusively considered for the following deposition efficiency analysis.

Ti-6Al-4V Alloy Coatings

The deposition efficiency is strongly affected by the variation in the rotational speed. The results, presented in Figure 5.34, describe the effects of the rotational speed and resultant axial force on the deposition efficiency. The deposition efficiency varies in a wide range between 9 % and 39 %. As expected, the layers that were generated at low rotational speeds (400 min^{-1} - 600 min^{-1}) and exhibit low coating thicknesses provided low deposition efficiency in the range of 9 % - 12 %. High deposition efficiencies were achieved for coatings generated at high rotational speeds (2000 min^{-1} and 6000 min^{-1}) in the range from 26% to 39 %. It is worth mentioning that the most efficient configuration was achieved at a rotational speed of 3000 min^{-1}, which generated the highest temperature (1379 °C).

The fact that low rotational speeds results in low efficiency and high rotational speeds results in high efficiency can again be related to the resultant axial forces. With the low axial forces (~ 1 kN) and high rotational speeds, less of the material was pushed to the flash compared with the coatings produced at low rotational speeds and high axial forces (~30 kN). Correspondingly, when less material passes into the flash, more material can be deposited increasing the deposition efficiency. Gandra et al. [42] reported the opposite relationship between the axial force and deposition efficiency in aluminium alloys, noting that a high axial force range results in effectively deposited material, whereas the use of low forces provides low efficiency because high axial force leads to improvement in the bonded width of the

coatings [42]. Similar behaviour of decreasing deposition efficiency with increasing axial force has been reported for aluminium alloys [7]. No explanation for this observation has been suggested by the authors. Furthermore, when the deposition efficiency increased at 2000 min^{-1} for Ti-6Al-4V alloy, the highest energy input was determined. Moreover, this condition depicts the transition zone where the flash formation at the coating no longer occurs.
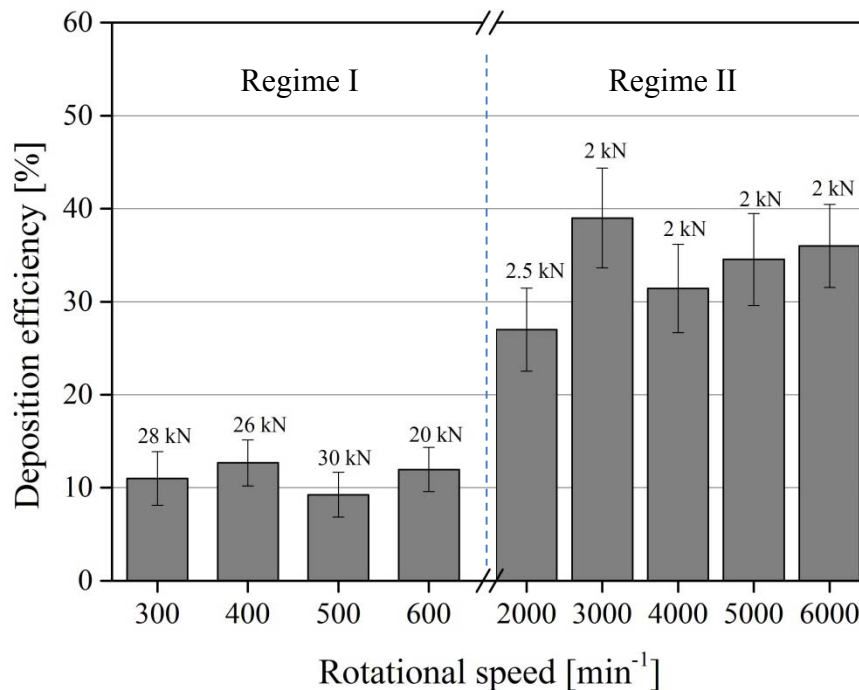

Figure 5.34: Deposition efficiency of Ti-6Al-4V coatings as a function of the rotational speed with corresponding axial forces exhibiting two clearly defined regimes.

Ti-Gr.1 Coatings

Based on the coating geometry and process parameters, the deposition efficiency was determined for Ti-Gr.1 coatings produced at various rotational speeds, displayed in Figure 5.35. The strong influence of the rotational speed can be clearly noticed. The lowest deposition efficiency was achieved with coatings produced in the range of 300 min^{-1} to 600 min^{-1} with a maximum value of 31 %, which is remarkably higher than the efficiency of the Ti-6Al-4V coatings (12 %) at this low rotational speed range. The presence of the alloying elements in Ti-6Al-4V leads to a different high-temperature strength compared with pure titanium [89]. It can be assumed that pure titanium exhibits a slightly lower material resistance to deformation than Ti-6Al-4V at a similar temperature, allowing the transfer of a higher material volume onto the substrate and leading to higher deposition efficiency.

Coatings generated at high rotational speeds show distinctly higher values up to 51 %. The tendency of achieving higher deposition efficiency at high rotational speeds compared with low rotational speeds is related to the low forces as previously explained for Ti-6Al-4V.

64

Furthermore, a transition for both Ti-6Al-4V and Ti-Gr.1 can be noticed in which the deposition efficiency increases (3000 min⁻¹ for Ti-Gr.1 and 2000 min⁻¹ for Ti-6Al-4V). This transition is located at exactly the same range where flash formation at the coating no longer appears. This fact supports the theory suggested in section 5.2 dividing rotational speeds into two regimes.

The deposition efficiency of the Ti-Gr.1 coating exceeds that of the Ti-6Al-4V coatings. This might be related to the higher peak temperatures and lower resultant axial forces, leading to a lower amount of material that squeezes out to the flash formation at the rod.
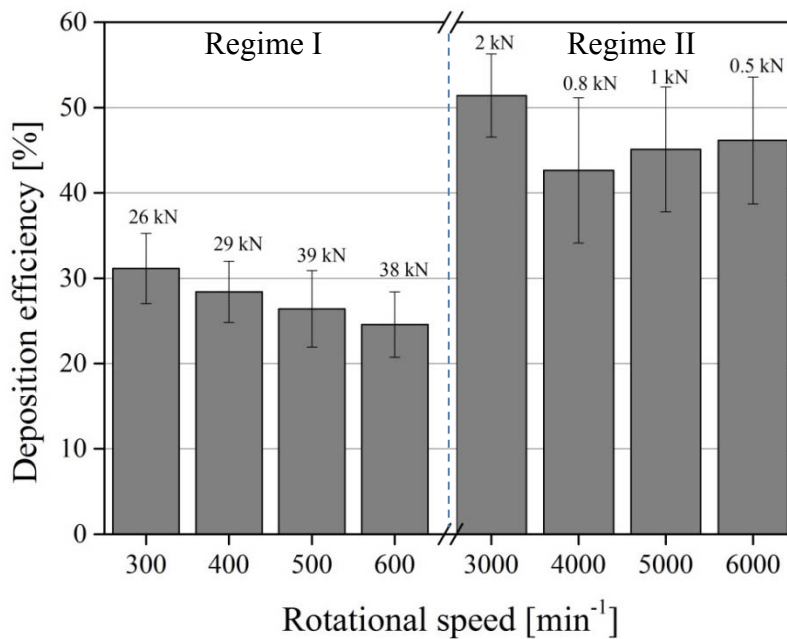

Figure 5.35: Deposition efficiency of Ti-Gr.1 coatings as function of the rotational speed with corresponding axial forces displaying two clearly defined regimes with a deposition efficiency up to 31 % (regime I) and 51 % (regime II).

5.5 Microstructural Analysis of the Base Material and Coatings

In this section, an overview of the microstructural investigation of the base material and coatings is presented and discussed. The grain size formation within the coatings is correlated with process parameters and thermal phenomena. In order to understand the microstructure formation within coatings, the attempt was made to separate the two most significant influencing factors, the thermal cycle and the deformation. To simulate the thermal cycle induced during FS without applying additional deformation, dilatometer experiments were performed. The differences of the microstructure of the coatings and dilatometer tested samples were discussed.

Both Ti-6Al-4V alloy and Ti-Gr.1 undergo phase transformations when reaching the β-transus temperature of 995 °C for Ti-6Al-4V and 882.5 °C for Ti-Gr.1 while heating. As mentioned in the introduction, the microstructural features of Ti-6Al-4V and Ti-Gr.1 coatings differ after cooling due to the martensitic phase transformation. Furthermore, it is well known that the microstructure of the materials during deformation is influenced by the deformation temperature and strain rate in addition to the strain because thermally activated restoration processes, such as dislocation climb, occur at certain temperatures [90].

Ti-Gr.1 Coatings

The microstructure of the Ti-Gr.1 base material is presented with an EBSD map (Figure 5.36), in which the different colours indicate different grain orientations. The microstructure comprises a hexagonal α structure with fine equiaxed grains with an initial size of 7.9 µm ± 2 µm.
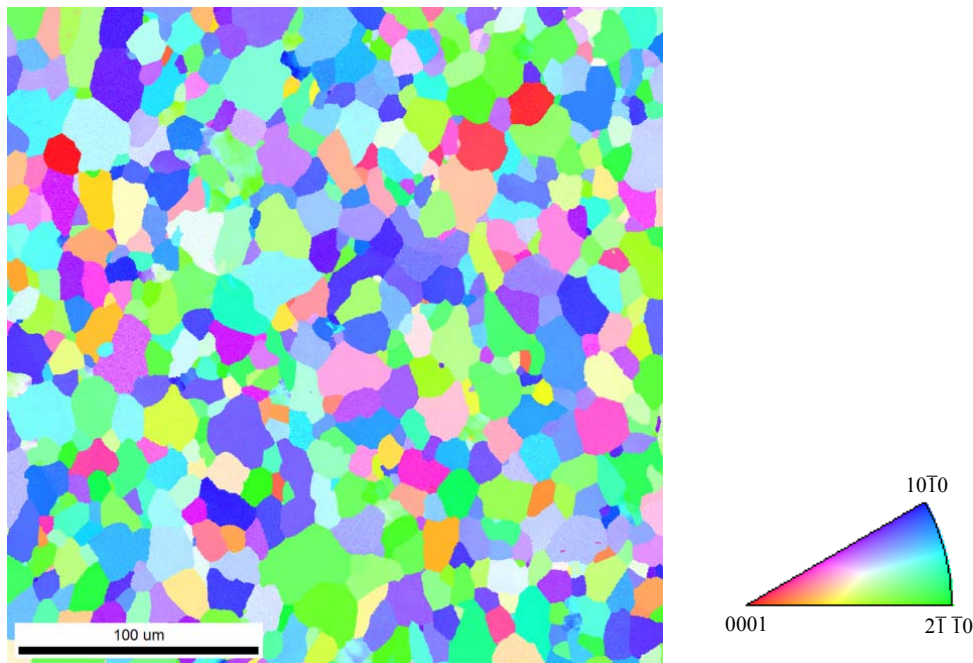

Figure 5.36: EBSD image with respective IPF of Ti-Gr.1 base material exhibiting the grain morphology and their orientations.

In the previous sections, it was demonstrated by the results of the IR camera and thermocouple measurements that the temperature passed the β phase transformation temperature while processing.

Based on the temperature study, it was shown that the material plasticises rapidly, achieving the peak temperature with a high heating rate within the process zone. The coatings were processed within the beta phase, despite such high heating rates, and cooled down through the beta transition zone into the alpha phase. The microstructure of the coatings exhibits a

recrystallised acicular α' martensite structure. Cross sections of the coatings have been analysed by light and scanning electron microscopes.

Figure 5.37 a displays the interface between the coating (produced at 700 min^{-1} rotational speed and 16 mm/s deposition speed) and the substrate. No defects or voids are observed at the interface. The new dynamically recrystallized grains are presented in Figure 5.37 b. The microstructure of pure titanium coatings exhibits recrystallised grains in which an acicular fine structure can be noted, and the grains exhibit irregular characteristics.
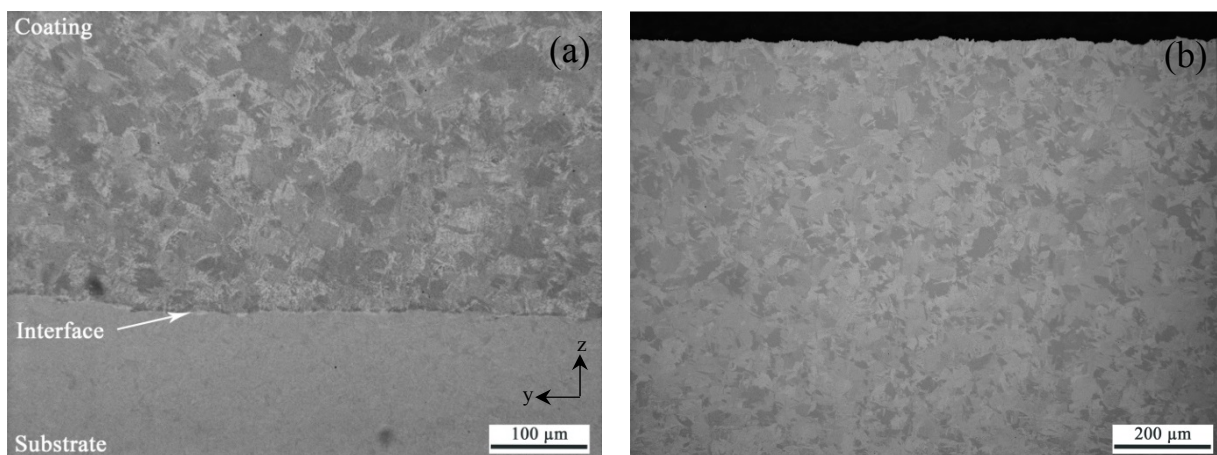

Figure 5.37: Interface between Ti-Gr.1 coating (generated at a 700 min^{-1} rotational speed and 16 mm/s deposition speed) and substrate (a), and microstructure of the coating with higher magnification (b).

The grain size of the microstructure of the coatings generated at low rotational speeds cannot be identified by light microscopy, due to the small grain size. Therefore the samples were prepared using a cross section polisher, and EBSD analysis was carried out to investigate the grain size evolution of the coatings generated at the different conditions. EBSD images were taken from the centre of the coatings. The image shows the microstructure exhibiting recrystallised refined α' grains with a homogeneously developed grain size (4.4 μm ± 2 μm) (Figure 5.38). The shape of the recrystallised grains differs from the equiaxed grain shape of the base material, revealing more serrated grain boundaries. Moreover, a texture gradient from the bottom of the image to the top can be recognised, which must be related to the material flow during the process.

The coatings generated at a rotational speed of 3000 min^{-1} exhibit an acicular microstructure similar to those obtained at a low rotational speed (Figure 5.39). However, differences in the grain size were noticed. In this context, dynamic recrystallisation has occurred but with an increase in grain size compared with coatings generated at low rotational speeds. The grain size displays an irregular distribution with some small grains formed between large grains. EBSD images demonstrate this feature more precisely (Figure 5.40). The grain size was

measured based on the interception length method. The average grain size of the coating produced at 3000 min^{-1} exhibits a value of 103.8 µm ± 10 µm.
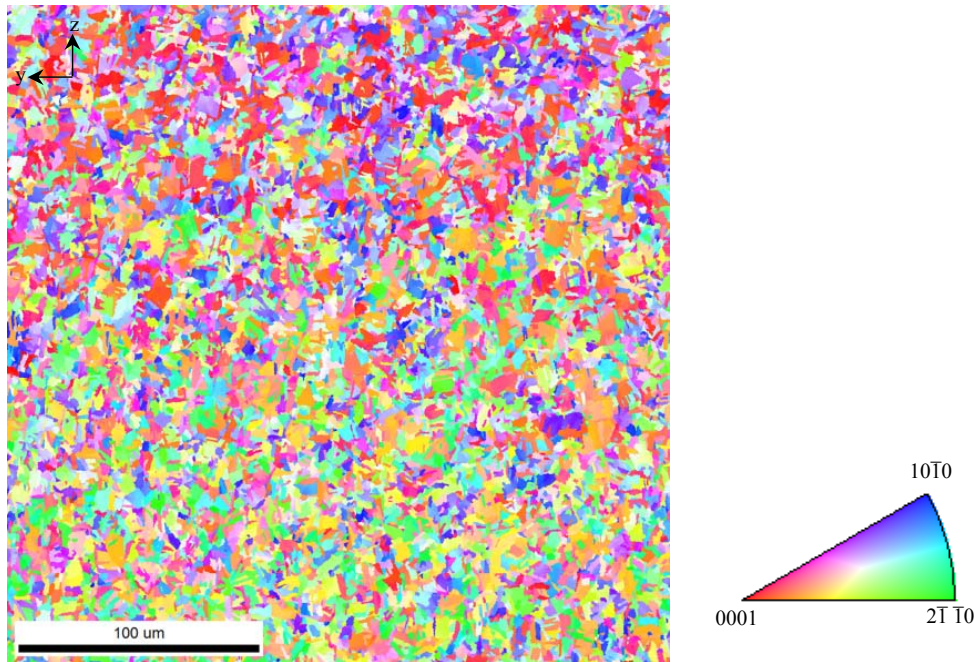

Figure 5.38: EBSD image with IPF of the microstructure of a Ti-Gr.1 coating produced at 300 min^{-1} exhibiting dynamic recrystallisation with refined α' grains.
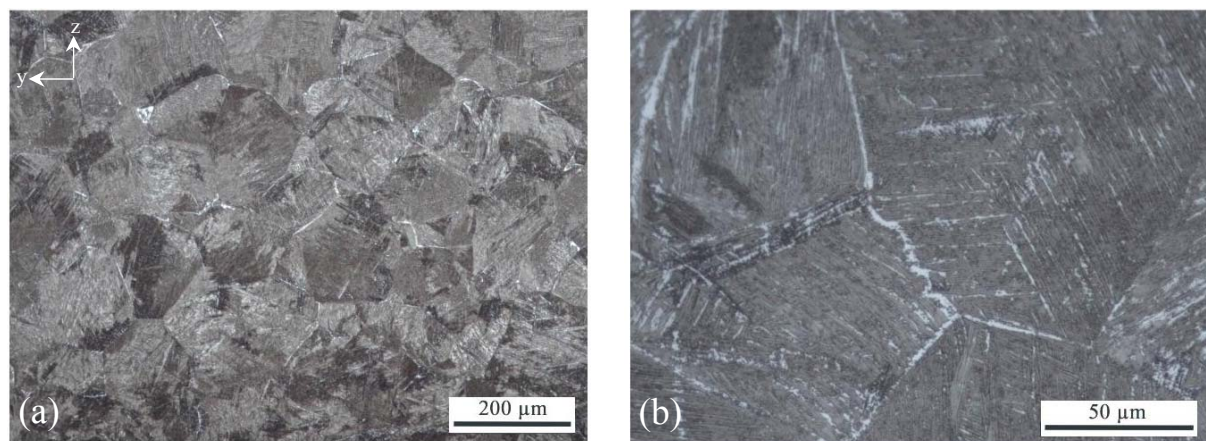

Figure 5.39: Microstructure of coatings processed at 3000 min^{-1} (a), and higher magnification exhibiting the grain size (b).

Figure 5.41 presents the maximum measured temperatures as a function of the rotational speed. The corresponding EBSD images are displayed for each condition to establish a correlation with the grain size. As mentioned earlier, experiments with a low rotational speed regime exhibit low temperatures, which rise with increasing rotational speed. The employment of a high rotational speed regime results in constant higher temperatures. These thermal ascents and descents can be noticed in the microstructural evolution.
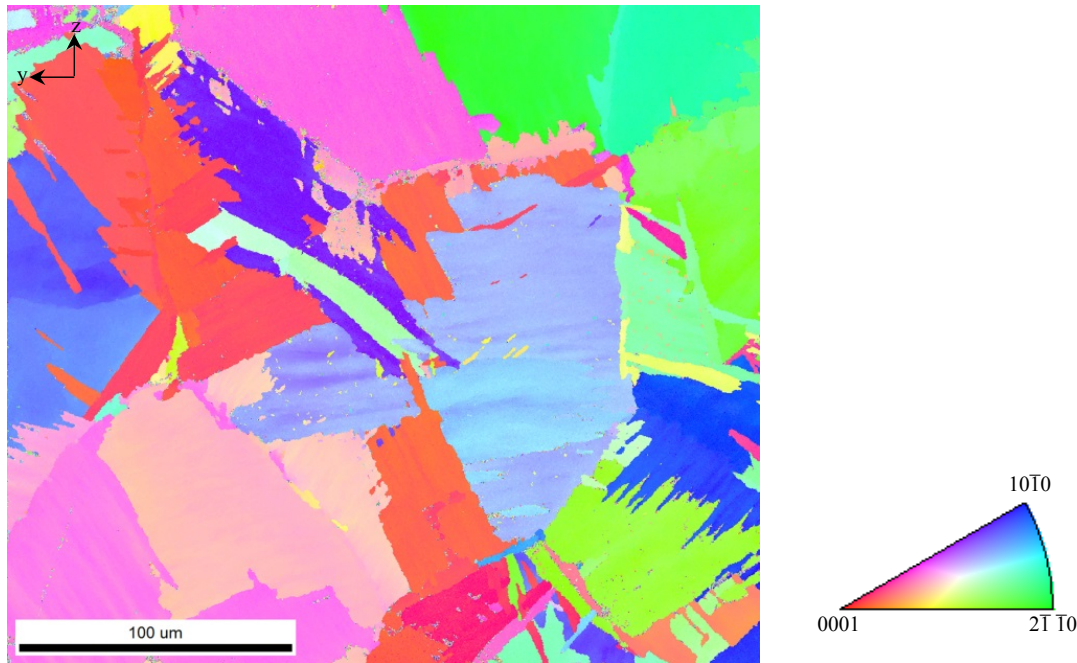
Figure 5.40: EBSD image with IPF taken from the centre of the coating produced at a 3000 min^{-1} rotational speed.

Compared with the base material with a grain size of 7.9 μm, the structure of the 300 min^{-1} coating shows refined recrystallised grains with a grain size of 4.4 μm ± 2 μm. The recrystallised grains have serrated grain boundaries and are homogeneously distributed. However, it can be seen that the grain size of the coatings rises with an increase in rotational speed and temperature in regime I. The grain size of the processed coatings continuously increases with an ascent in the rotational speed in the range from 300 min^{-1} to 1000 min^{-1} and in the temperature range from 995 °C to 1010 °C. However, the recrystallised grains have smaller sizes compared with the initial size of the base material. In regime II at the high rotational speed (3000 min^{-1}) and the elevated temperature (1421 °C), grain coarsening can be observed. Moreover, with a further increase in rotational speed and a slight decrease in temperature, the grain size seems to decrease marginally. It seems that the temperature is the dominant factor in the grain size evolution. Furthermore, the formation of lamellae differs with the rotational speed in regime II. At a rotational speed of 3000 min^{-1} the lamellae are located within the grains. At higher rotational speeds (5000 min^{-1} and 6000 min^{-1}) the lamellae also grow into the neighbouring grains and different orientations can be noticed.

Nevertheless, the limitation of grain refinement was observed, which is known to occur also for other materials processed by SPD techniques. In [46] it has been reported that the grain size becomes finer until reaching a certain pass number when using equal-channel angular pressing. At the given pass, the grain size cannot be fragmented any further. Conversely, it has been shown that the grain size increases at a higher deformation degree [46]. The limitation of grain refinement by dynamic recrystallisation of pure Ni is also known [91].

When deformation is applied to Ni with an initial nanocrystalline structure of 20 nm grain size, the deformation by HPT induces grain growth, and the nanocrystalline structure transforms into an ultrafine grained structure with a grain size of 200 nm. The reason for the saturation of the grain refinement is proposed to be, in addition to the grain boundary sliding or localised deformation, the grain boundary migration during severe plastic deformation [91].

The relationship between the temperature and the grain size has been reported in the literature. It was shown that the grain size increases with increasing temperature [92]. Furthermore, it was reported that in a high temperature deformation field, the grain size declines with strain until reaching a strain level of 60 %, beyond which the grain size rises with increasing strain level [92]. Since the strain level applied in the current study is unknown and might be greater than 60 %, no direct relationship can be established. Nevertheless, a tendency of the grain growth of pure titanium depending on the strain and temperature can be assumed.
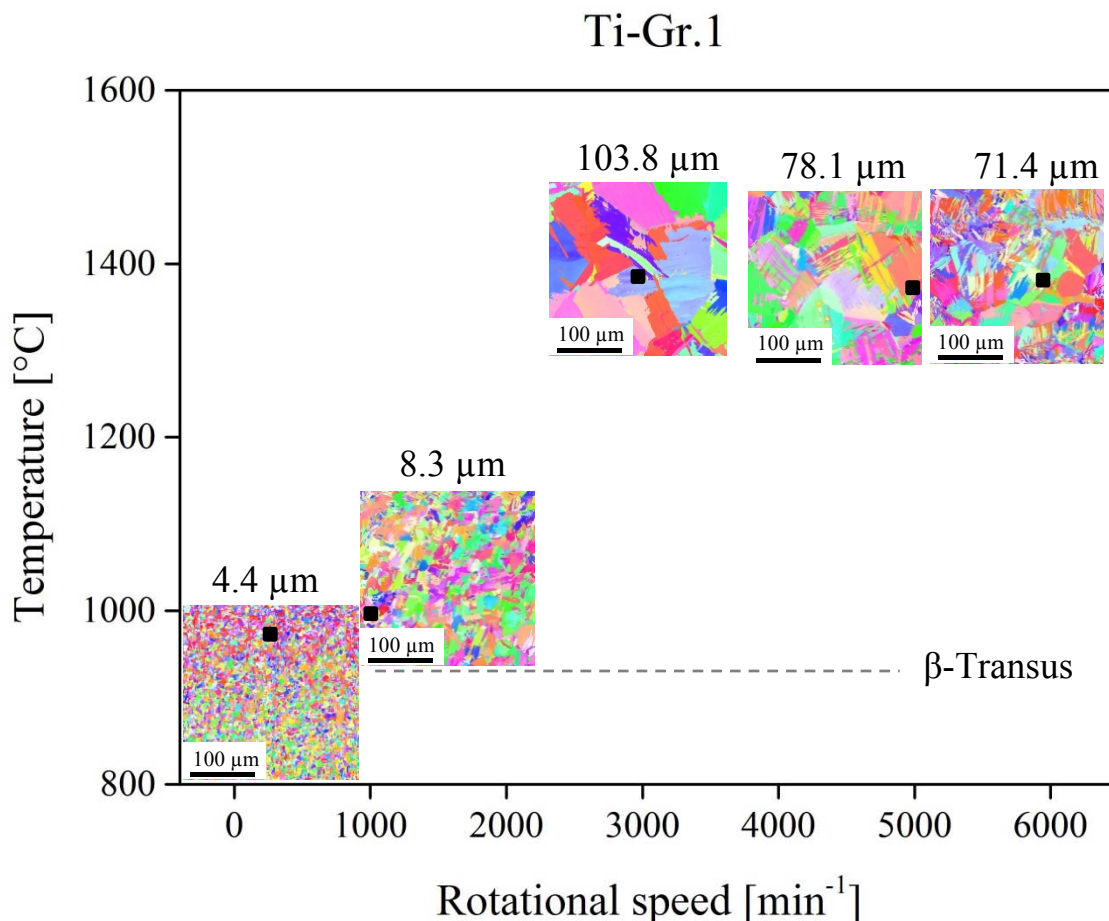

Figure 5.41: EBSD images of the coatings produced at corresponding rotational speeds and temperatures. Grain growth with increasing rotational speed and temperature can be observed. A decrease in grain size at a constant temperature with a further increase in rotational speed is visible.

Ti-6Al-4V Coatings

The microstructure of the Ti-6Al-4V rod base material contains a dual-phase alpha-beta structure, which exhibits equiaxed alpha grains with transformed beta islands (Figure 5.42 a). The β transformation temperature (β-transus) of this alloy is approximately 995 °C. An EBSD map shows the microstructure of the base material with an initial grain size of 4.42 μm ± 2 μm (Figure 5.42 b).
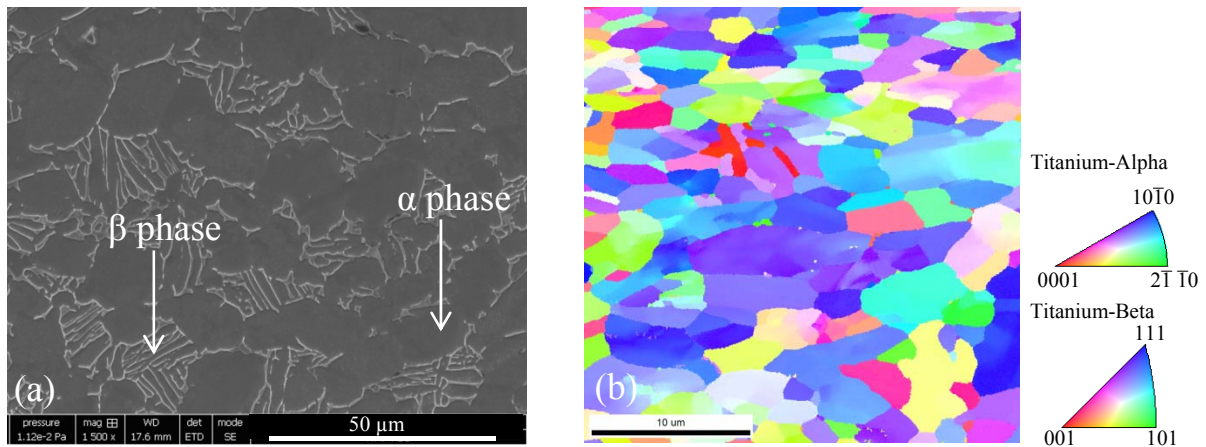

Figure 5.42: Microstructure of Ti-6Al-4V rod in its as-received condition (a), and an EBSD map with IPF exhibiting equiaxed grains with their orientations and sizes (b).

As the temperature analysis revealed, the Ti-6Al-4V coatings were deformed during the FS process in the β phase and were cooled through the α+β phase and the martensite regime. As known, the phase transformation of Ti-6Al-4V while cooling can occur either martensitically or by the diffusion-controlled nucleation and growth process. The phase transition depends on the cooling rate and the alloy composition. Generally, the martensitic transformation can occur at cooling rates higher than 18 Ks^{-1} and might lead either to the hexagonal crystal lattice (α') or orthorhombic crystal lattice (α'') [13, 16]. According to the measured cooling rates (39.8 Ks^{-1} – 53.8 Ks^{-1}), which were higher than 18 Ks^{-1}, a diffusion-controlled nucleation can be precluded, so it can definitively be stated that a martensitic transformation occurred.

The microstructure and HAZ of a coating generated at a 400 min^{-1} rotational speed and 16 mm/s deposition speed are shown in Figure 5.43. The interface between the coating and substrate does not contain any defects or voids. The coating, HAZ in the centre and unaffected substrate at the image bottom can be seen. The transition zone between the microstructure formed in the HAZ and the unaffected base material can be clearly identified. The grains are recrystallised and refined within the HAZ. The grain boundaries within the coating cannot be distinctly seen and can only be locally adumbrated. Nevertheless, the microstructure in the coatings was dynamically recrystallised, and the martensitic transformation occurred.
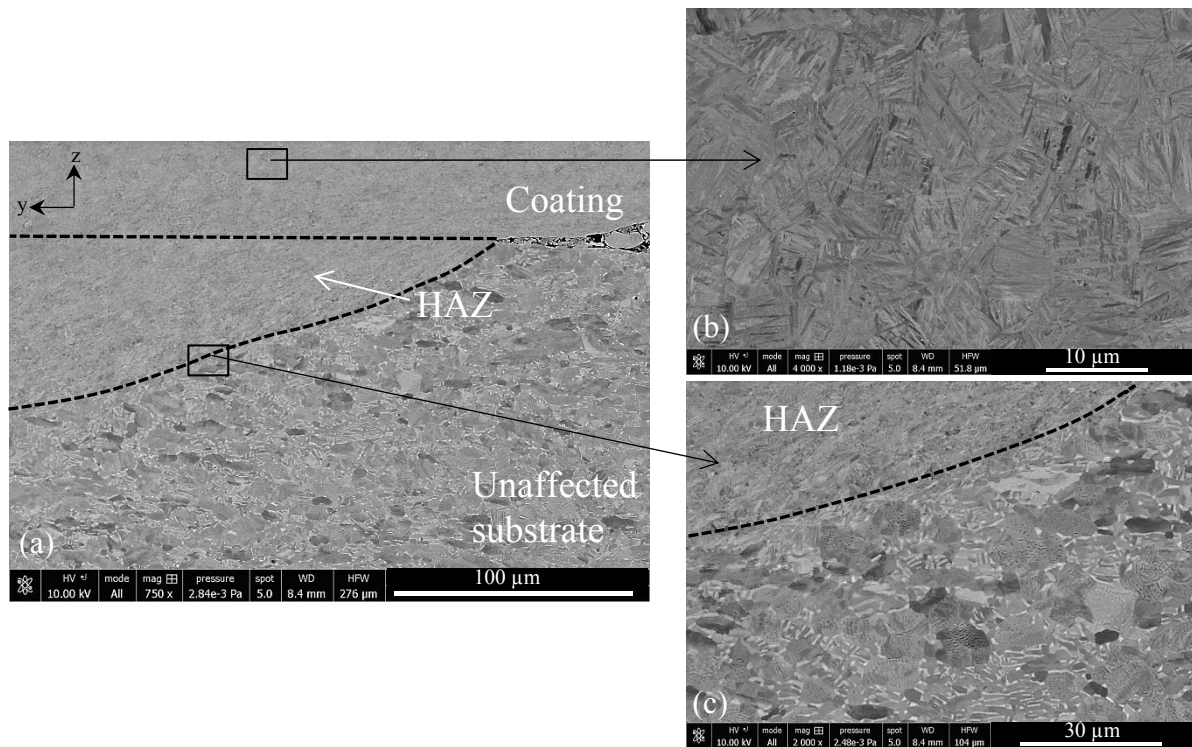
Figure 5.43: Microstructure evolution of coating produced at 400 min^{-1}: (a) overview, (b) coating and (c) HAZ and unaffected substrate (SEM).

Figure 5.44 shows micrographs taken from the centre of the coatings generated at high rotational speeds of 3000 min^{-1} and 6000 min^{-1}. The grain boundaries can be barely distinguished in both conditions. The grains seem to be irregular in their shape.
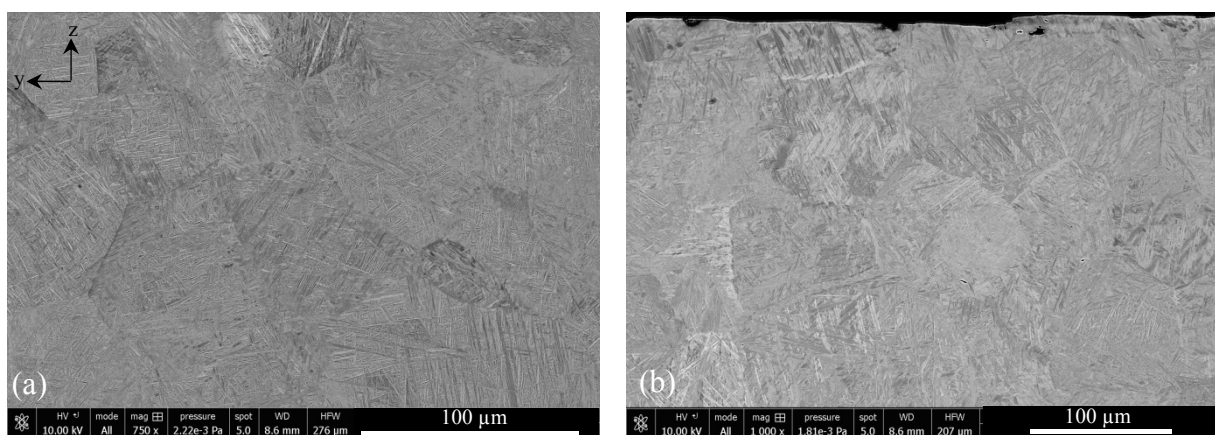

Figure 5.44: Microstructure of coatings produced at 3000 min^{-1} (a) and 6000 min^{-1} (b).

An EBSD image of the coating demonstrates a martensitic acicular structure, and the grain boundaries cannot be identified here (Figure 5.45). Furthermore, lamellar α' colonies are

visible in the coarse prior beta grains. These α' lamellae are nested and interleaved according to 12 orientation possibilities derived from 6 slip planes and 2 slip directions of the α crystal orientation [9]. However, within the individual α lamellae, the orientation is identical. It can be seen that the high and low deformation degrees (rotational speeds) affect the prior beta grain size. To characterise the prior beta grains formed at a high temperature, grain size reconstruction must be conducted, which will be presented in subsection 5.5.1.
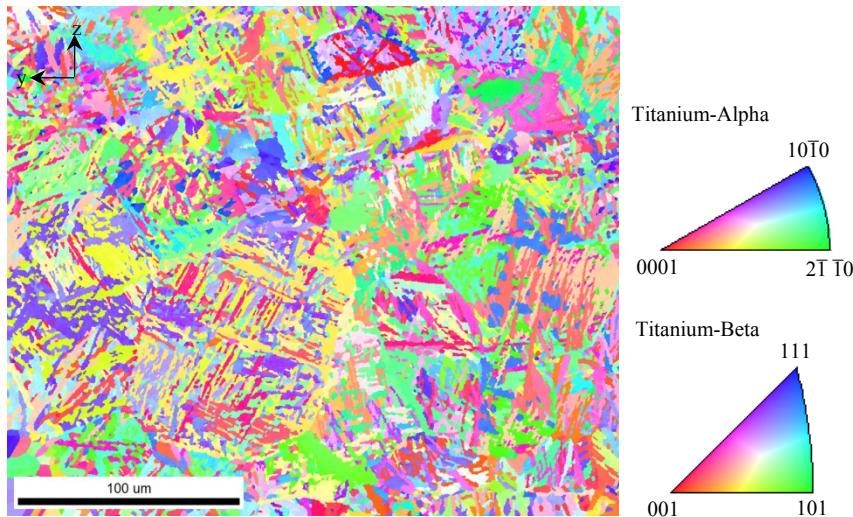

Figure 5.45: Ti-6Al-4V coating with recrystallised grains exhibiting a hexagonal structure generated at a 3000 min^{-1} rotational speed (EBSD).

5.5.1 Grain Size Reconstruction for Ti-6Al-4V Alloy Coatings

Initially, the prior beta boundaries could not be identified thoroughly. To emphasise the prior β grain boundaries at high temperatures, the grain boundary reconstruction was obtained based on the method suggested by Gey and Humbert [93]. The main aim of this method is to distinguish the prior β grain boundaries from other high-angle boundaries by a classification of misorientations between α variants inherited from the same parent β-grain according to the Burgers orientation relationship. The following angles with individual planes were selected for Ti-6Al-4V alloy: $60°\langle11\bar{2}0\rangle$, $60.83°\langle\overline{1.377};\bar{1};2.377;0.359\rangle$, $63.26°\langle\overline{10};5;5;\bar{3}\rangle$ and $90°\langle1;\overline{2.38};1.38;0\rangle$ [72, 93-95]. The contours of the prior β grain boundaries can be reconstructed by eliminating the supernatant boundaries from the EBSD map. Eventually, a black and white map is created, exclusively showing the prior beta grain boundaries and excluding the martensitic features. The reconstructed grain size map for a coating generated at a low rotational speed is shown in Figure 5.46. The prior beta grain size of the coatings generated at a low rotational speed regime differs from that in the high rotational speed regime (Figure 5.44). Further reconstructed grain size maps for various rotational speeds were created.
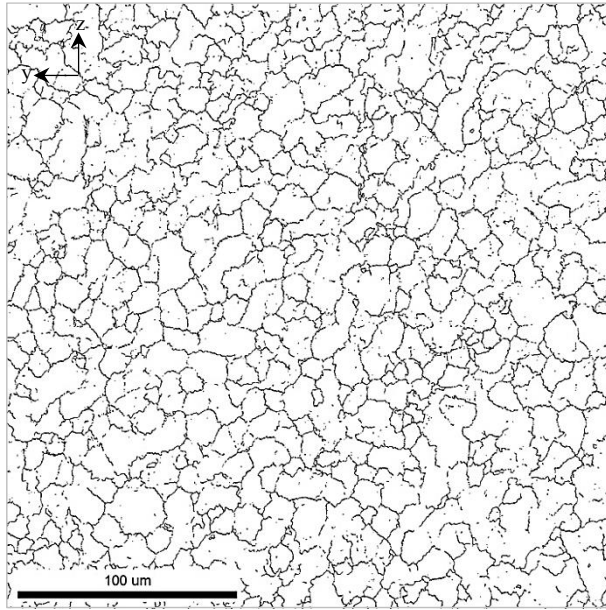
Figure 5.46: Reconstructed grain boundary map of a coating generated at a 400 min^{-1} rotational speed.

Similar to Ti-Gr.1 coatings, the processing temperature was plotted versus the rotational speed. In each condition, the corresponding boundary map is displayed (Figure 5.47). The coatings generated at low rotational speeds exhibit refined grains. The coatings produced at a 400 min^{-1} rotational speed measuring the size of 1.64 µm ± 1.33 µm linear intercept length. An increase in the rotational speed and resultant temperature lead to a marginal increase in the grain size. Subsequently, the coatings generated in the high rotational speed regime (3000 min^{-1}), with a high peak temperature of 1298.3 °C, demonstrate significantly coarser prior beta grains of 28.43 µm ± 11.47 µm. From 3000 min^{-1} to 6000 min^{-1}, no further grain size increase was observed; instead, the grains become marginally smaller.

It is well known that in annealing treatments and hot working of titanium alloys, temperatures higher than β-transus are usually avoided due to the occurrence of grain growth. The driving force of the grain growth is derived from the surface energy of the grain boundaries. The large grains grow at the cost of small grains according to the "Ostwald-ripening" phenomenon. By this process, the number of grains decreases while their size increases. The area of the grain boundaries decreases along with the total energy stored in them, so a state of high thermodynamic stability is consequently achieved [50, 96]. This grain size evolution has been observed in friction stir welding and in friction-welded microstructures. The grain size evolution for titanium was shown to be dependent on the heat input and the peak temperature until a certain degree of deformation was reached [70], [97]. Based on the current microstructural results of Ti-6Al-4V and Ti-Gr.1 coatings, it can be concluded that the combination of the degree of deformation and temperature affects the prior beta grain size evolution. Moreover, Honarmandi et al. reported that the prior beta grain size increases when

either the temperature or the strain rate increases [98]. In his work an investigation has been conducted on Ti-6Al-4V alloy under isothermal hot compression testing. It has been demonstrated that using a testing temperature of 1100 °C at various strains from 0.1 to 0.5 in 0.1 increments the grain size increases from 37.7 μm to 46.4 μm. The strains applied in FS are unknown but they must be much higher than those applied in other severe plastic deformation processes. Moreover, it is unknown whether either static or dynamic grain growth or both occurred, so it is difficult to say exactly how the recrystallisation occurred. The grains might grow either dynamically while processing or statically in the post-process condition while cooling. Generally, dynamic grain growth development is faster than static growth [99].
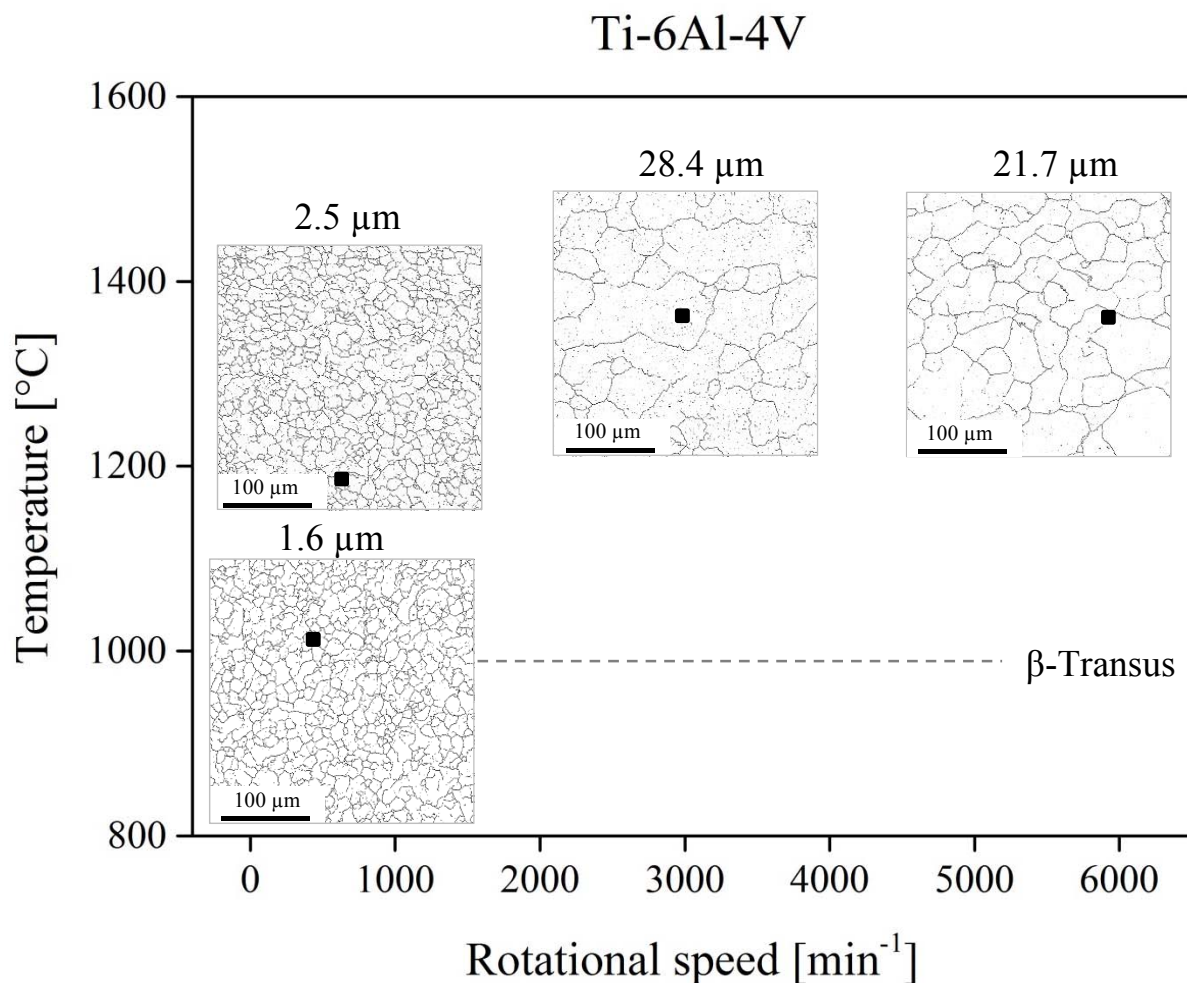
Figure 5.47: Relation of the rotational speed and temperature and their influence on the grain size distribution in coatings.

The investigation of a combined increase in temperature and strain and its impact on the grain size has not been observed in other thermo-mechanical processes such as FSW. Moreover, in FSW, when increasing the rotational speed in the range of 300 min^{-1} to 600 min^{-1} in 100 min^{-1} increments, the grain size also increases. This grain size increase has been suggested to be

correlated with increased heat input and corresponding temperature when raising the rotational speed. The increased temperatures (above the β-transus) lead to prolonged dwell time in the β phase, which results in the evolution of coarse grains [75]. Analogous conclusions regarding increased grain sizes with higher temperatures and dwell times may be drawn for friction surfacing. The coatings of Ti-Gr.1 exhibit a larger grain size compared with the Ti-6Al-4V coatings, which can be related to the higher generated temperatures and the resulting longer dwell time within the β phase.

Still, the effect of the large differences in strain and strain rate encountered in the every wide parameter window applied in the current study must also be considered. Because the strain applied in the current study is unknown, no direct relation to the reported severe plastic deformation literature can be established, but the occurrence of grain growth with increasing strain can be assumed.

Adiabatic Shear Bands during Friction Surfacing

The thorough investigation of the coating microstructure has revealed an interesting finding. In the near-surface regions and within the coatings, equiaxed grain bands were observed. This finding was observed for all parameter sets that do not lead to flash formation at the coatings (Figure 5.48). The grains do not contain martensitic structure such as the matrix, and EBSD analysis revealed them to be α-phase. Equiaxed grains with a size of ~ 1 μm were formed parallel to the rotational shear plane without a preferred location. This formation of the equiaxed grains within the martensitic structure could stem from adiabatic shear band formation with distinct defined boundaries to the matrix, which might be formed during the plastic deformation by FS. Another possibility might be that the equiaxed grains recrystallised during cooling.
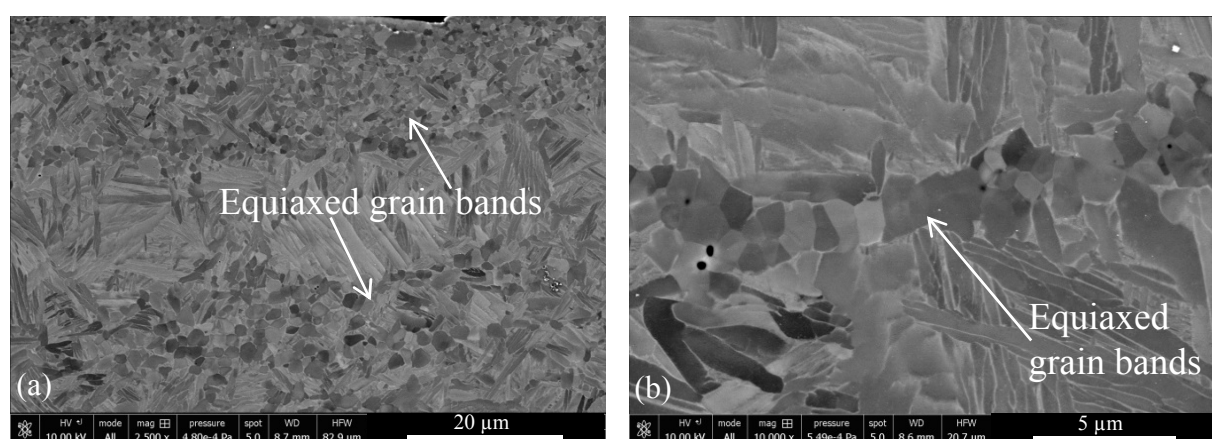

Figure 5.48: Microstructure of coating generated at 6000 min^{-1} exhibiting equiaxed grain bands with a size of < 1 μm surrounded by the martensitic structure (a) and equiaxed grain bands at high magnification (b).

Adiabatic shear localisation occurs during plastic deformation of materials when the thermal softening exceeds the strain hardening [94]. The presence of localised thermal softening in materials can lead to a cycle of concentration of plastic deformation, resulting in a local increase in temperature, followed by more intensified local deformation, resulting in the formation of adiabatic shear bands. The formation of the shear bands depends on the alloying elements and the original microstructure of the materials. In the case of titanium alloys, a lamellae structure has a higher susceptibility to shear band formation compared with the equiaxed structure [100, 101]. Adiabatic shear bands can be easily triggered in titanium alloys because of their low heat conductivity (~16 W/m K) [102].

Meyer et al. found that shear bands formed during plastic deformation of titanium by compression Kolsky experiments [86]. It has been demonstrated that the shear bands consisted of small grains with sizes of 0.05 μm and 0.3 μm. Moreover, hardness in the shear band region and adjacent matrix showed similar values, which was explained by the deformation structure. The material adjacent to the shear bands is work hardened by dislocations and deformation twinning. Inside the shear band, the increase in hardness was derived from the reduction in grain size. Both effects lead to similar hardness results [86]. In the FS coatings investigated in this work, no hardness variations were found for the bands of fine grains.

Moreover, shear compression experiments on Ti-6Al-4V alloy have been conducted using a Kolsky apparatus at a strain rate of 3000 s^{-1}. It was suggested by the author that DRX leads to adiabatic shear band formation, which is not the consequence of high local temperatures, and strains as generally assumed. Therefore, DRX can be considered as a possible mechanism leading to adiabatic shear band formation [103].

A similar finding with regard to equiaxed grain bands forming in the stir/transition zone has been reported for titanium alloys after friction stir welding [104]. Mishra et al. reported the presence of equiaxed grain formation in the heat-affected zone, suggesting the formation of α grain boundaries [79]. For FSW, adiabatic shear bands were not considered as the source of the equiaxed grain bands.

Because no publications about fusion welded structures have reported on the formation of equiaxed grains within the martensitic structure, it can be concluded that the occurrence of equiaxed grains is related to severe plastic deformation induced during the FS process and resulting dynamic recrystallisation. The fact that widespread, narrow bands consisting of a different microstructure exist in the FS coatings may become relevant in the future, since they may affect mechanical properties, e.g. under cyclic loading.

5.5.2 Thermal Cycle Induced by Dilatometer

To understand the individual impact of elevated temperatures and rapid cooling rates induced by FS on the grain size, experiments using dilatometer equipment were conducted to decouple the thermal phenomena from the plastic deformation. The thermal cycle during FS was measured and was applied to samples tested in the dilatometer equipment without deformation. The microstructure derived from the Ti-6Al-4V and Ti-Gr.1 samples tested in the dilatometer were compared with the microstructure developed by FS coatings with identical thermal cycles but with the additional deformation induced by the process. The microstructure of the Ti-Gr.1 coatings and dilatometer specimens with the corresponding thermal cycle is demonstrated in Figure 5.49. By comparing both microstructures of dilatometer samples, shown in Figure 5.49 a, b, it can be observed that the grain growth kinetics are faster when employing a high temperature (1337 °C) and a cooling rate of 15.1 Ks^{-1} compared with the temperature near the β-transus (943 °C). A similar tendency regarding to the grain size can be seen in microstructures of the coatings (Figure 5.49 c, d). When deformation is induced, the temperature also seems to be a dominant factor in grain size evolution.
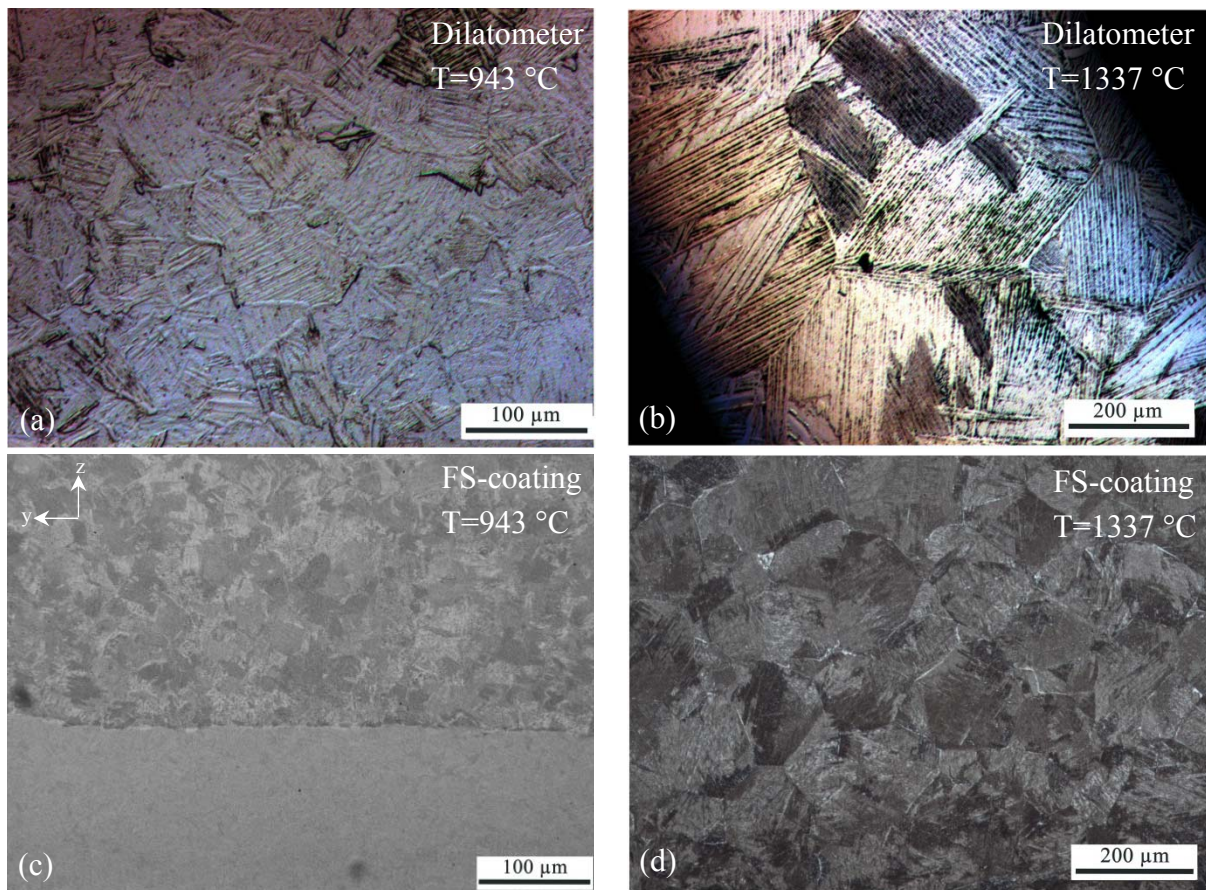

Figure 5.49: Microstructure of Ti-Gr.1 coatings generated at 400 min^{-1} (c) and 3000 min^{-1} (d) and dilatometer specimens (a, b) generated at identical thermal cycles.

When comparing the microstructure of the coatings and dilatometer samples produced with an identical thermal cycle, it can be clearly seen that the grains (90 μm ± 20 μm) are smaller within the coatings due to the applied deformation compared with the grain size of dilatometer samples (380 μm ± 10 μm). The microstructure produced at a low temperature (943 °C) and high cooling rate (46.6 Ks^{-1}) also displays finer grains in the coatings in comparison to dilatometer specimens (Figure 5.49 a, c). The acicular structure of dilatometer specimens is more clearly developed. At a higher temperature (1337 °C) and lower cooling rate (15.1 Ks^{-1}), the grains become generally coarser (Figure 5.49 b, d). The high temperature applied to the dilatometer samples achieved the recrystallisation temperature, leading to a decrease in free energy and grain boundary area and therefore an increase in grain size [51].

The thermal conditions recorded for FS were also induced in Ti-6Al-4V samples in the dilatometer tests. The thermal cycle was applied in dilatometer testing under two thermal conditions with a peak temperature of 1021 °C at a cooling rate of 39.6 Ks^{-1} and 1299 °C at a cooling rate of and 53.8 Ks^{-1}. The developed microstructures are presented in Figure 5.50.
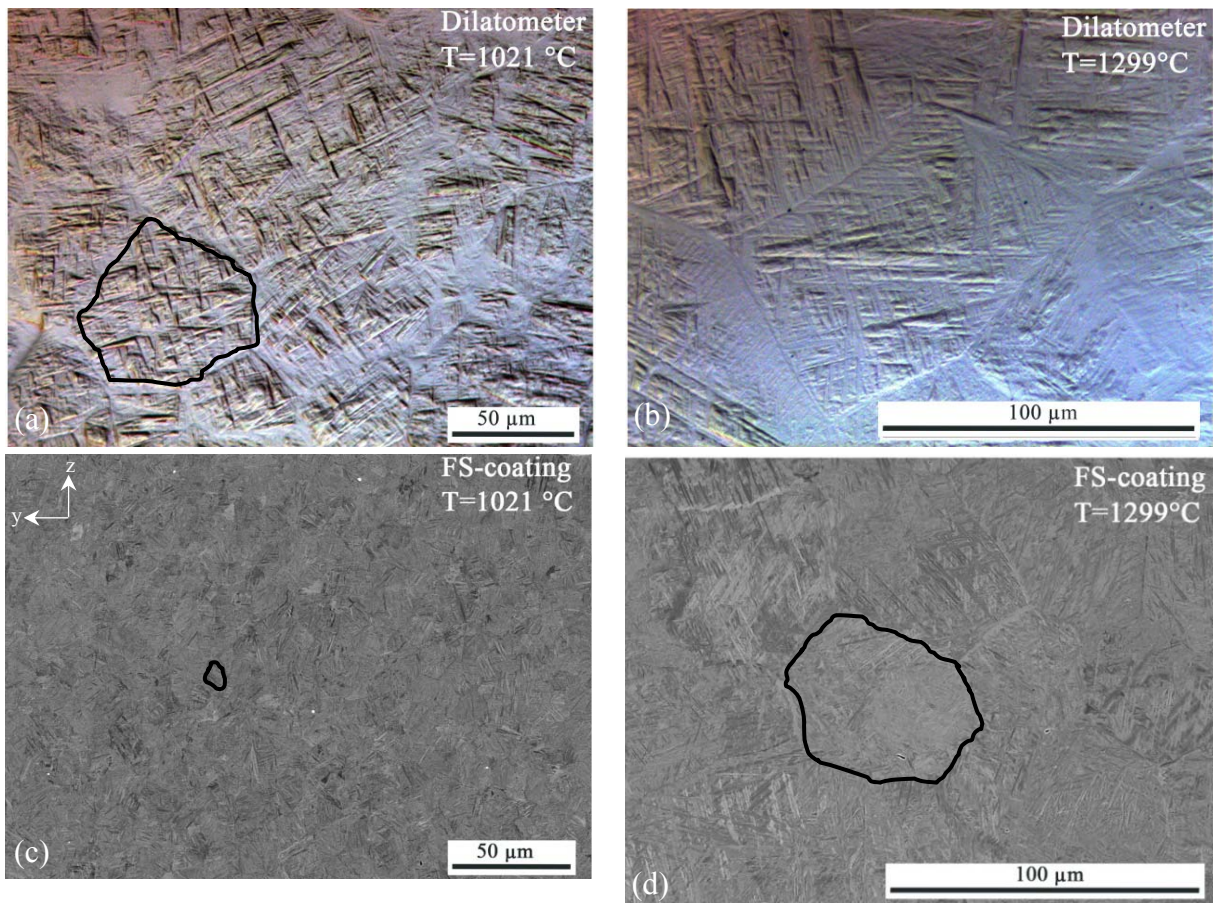

Figure 5.50: Microstructure of Ti-6Al-4V coatings produced at 400 min^{-1} (c) and 3000 min^{-1} (d) and dilatometer specimens (a, b) generated at identical thermal cycles.

The grain size of the microstructure of dilatometer-tested samples differs with the variation in the thermal cycle. It seems that the peak temperature is a major factor regarding the grain size evolution. The application of a high temperature of 1299 °C and induced high cooling rate of 53.8 Ks^{-1} produces large grains. A similar phenomenon regarding the impact of thermal conditions on the grain size evolution has been observed in the microstructure of coatings.

The grain size of the coatings in both thermal conditions is smaller than that in specimens from the dilatometer. Comparing both microstructures generated at a low temperature (1021.7 °C) that is near the beta transformation temperature with a cooling rate of 39.6 Ks^{-1}, such smaller grains were formed when deformation was induced (Figure 5.50 a, c). The dilatometer specimens show a grain size of 42 μm ± 10 μm, whereas the grains formed in the coating are 4 μm in size. When observing the coatings generated at a high temperature with a higher cooling rate (53.8 Ks^{-1}), the grains are larger (Figure 5.50 c, d). Again, the deformation here seems to lead to a decrease in grain size in comparison to the microstructure without deformation (dilatometer samples). The martensitic needles formed in the heated specimens are larger in size. Needles generated within the coating microstructure are finer and smaller in length.

The investigation of the grain growth kinetics of titanium alloys when heat treated in the β-field has been reported by Gil et al. [96]. It has been demonstrated that the grain growth rate is high during the first 15 to 20 min of heat treatment, after which the growth rate declines. This eventual reduction in the growth rate can be explained by the initial increase in grain size, which produces a decrease in the grain boundary area per unit volume ratio. Thus, the grain boundary interfacial energy per unit volume declines, so the driving force for further grain growth is reduced [96]. Similar phenomena in the low rotational speed regime can be observed. An increase in rotational speed in the range of 300 min^{-1} to 1000 min^{-1} leads to an increase in temperature (from 1021 °C to 1299 °C) that favours grain growth until it achieves a certain size by reducing the driving force for further grain growth. The high rotational speed regime exhibits nearly constant temperatures by increasing the rotational speed. The grain size decreases marginally with increasing rotational speed. The results of both coating materials (Ti-6Al-4V and Ti-Gr.1) showed grain refinement at the peak temperatures near the beta transus and in the low rotational speed regime. When processing in the high rotational speed regime, the temperature achieves its maximum value and remains constant with a further raise in the rotational speed. With the employment of a 3000 min^{-1} rotational speed, grain growth occurs. However, an additional increase in the rotational speed leads to a marginal decrease in grain size.

A quantitative representation of the grain size evolution is shown in Figure 5.51. It was shown that the maximum temperature (above the beta transus) significantly influences the grain size. Small grains were formed at 1200 °C, and large grains were formed at 1400 °C. Here, the

high temperature and corresponding longer dwell time (0.99 s for the high rotational speed regime and 0.54 s for the low rotational speed) in the beta phase seem to be crucial factors for coatings and dilatometer samples.
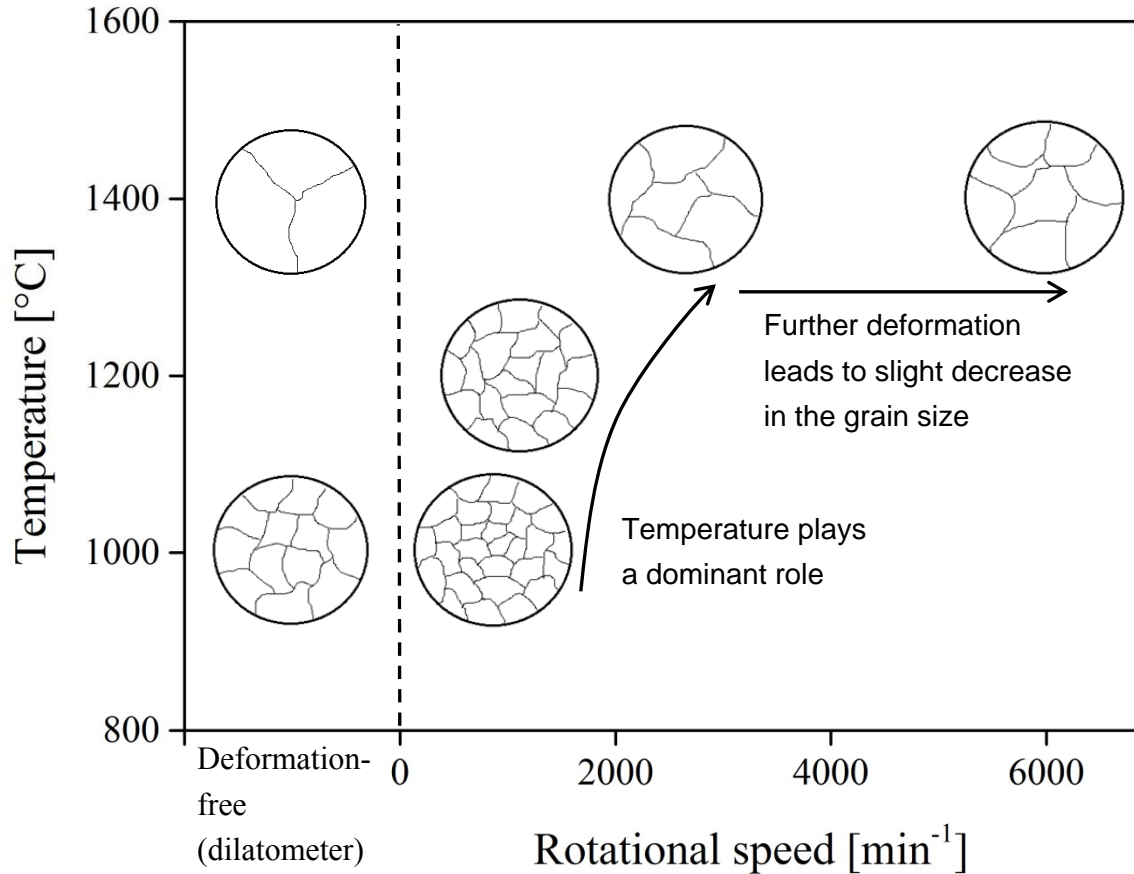

Figure 5.51: Qualitative representation of grain size evolution dependent on deformation and maximum temperature.

In conclusion, it can be stated that the grain size of the coating, produced in the low rotational speed regime, increases with rotational speed and resultant temperature, but it is smaller compared with the grain size of the dilatometer specimens. In the high rotational speed regime, the grain size of the coatings produced at a 3000 min^{-1} rotational speed is coarse, but it is still smaller than the grain size of the dilatometer specimens at the same temperature. Furthermore, by increasing the rotational speed to 6000 min^{-1} with the same resultant temperature, slightly smaller grains (25 μm ± 16 μm) were observed compared with the coatings produced at 3000 min^{-1} (28 μm ± 11 μm). However, the low grain size of the coatings produced in the low rotational speed regime still could not be achieved. This means that the influence of deformation cannot compensate for the influence of high temperatures, and the grain size is coarse. Both temperature and deformation play an important role in the grain size formation, but the influence of temperature seems to predominate.

5.5.3 Transmission Electron Microscopy Analysis

The microstructure evolution in Ti-alloys is complex, and depending on temperature cycles and strains, mixed states containing e.g. α as well as α', and varying amounts of β can exist [105]. The before presented EBSD results indicate, that the coatings mainly consist of α or α' phase, and no β was identified using this method. To gain a further understanding of the microstructure constituents, and to clarify possible differences at a microscopic level below the EBSD resolution, TEM analysis was carried out. The TEM images were taken from cross sections of the base material rods and from the top surfaces of coatings. The microstructure of the base material exhibits α and β phases (Figure 5.52 a), and dislocations were observed (Figure 5.52 b).
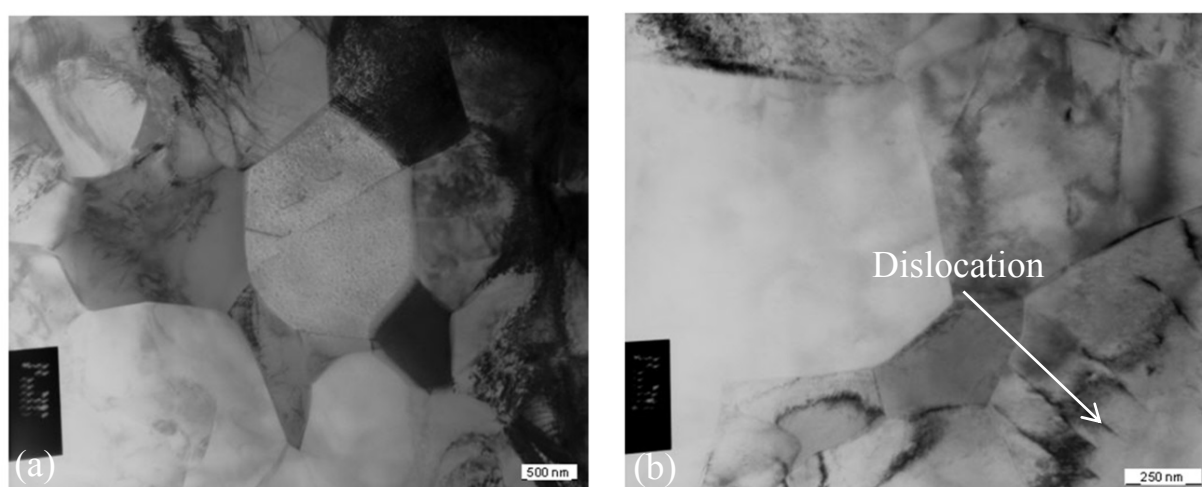

Figure 5.52: The microstructure of the Ti-6Al-4V base material consists of α and β phases (a), an image showing dislocations (b).

The microstructure of coatings exhibiting coarse and fine grain sizes was also investigated by TEM analysis. Figure 5.53 a reveals a coarse grain structure that shows a grain boundary extending diagonally through the image. Below the grain boundary, a recrystallised region can be assumed with few dislocations and twinning (Figure 5.53 b). Above the grain boundary, stacking faults were identified, the geometry of which correlates very well with the corrugated grain boundary. It can be assumed that the stacking faults might be responsible for the growth of the corrugated shape of the grain boundary.

In the diffraction image in Figure 5.54 b, double reflexes can be seen, which correlates very well with the microstructure image and suggests twinning formation. Also in Figure 5.54 a, the formation of a possibly recrystallised twin can be recognised, directly adjacent to a presumed martensite needle, which reveals a high dislocation density by its dark appearance. It was reported that martensitic plates, formed during phase transformation, contain generally high dislocation density and may contain sometimes twins [13]. Figure 5.55 also exhibits an image from a coating with a corresponding diffraction image. A region with the formation of

titanium oxides was observed. According to the analysis of the diffraction images, three different types of titanium oxides (Ti_4O_2, Ti_5O_2 and Ti_4O_5) might be considered. Despite the use of the shielding gas during friction surfacing titanium oxides were formed.
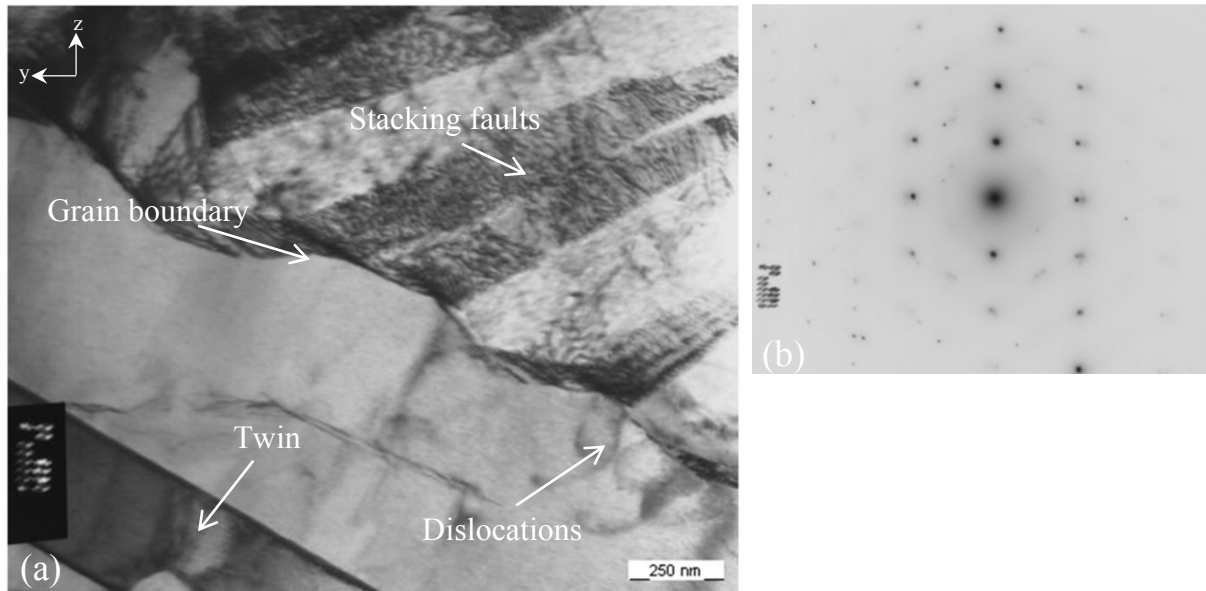

Figure 5.53: Microstructure of the coating generated at 6000 min^{-1} exhibiting a grain boundary, twinning and dislocations (a), and a corresponding diffraction image (b).
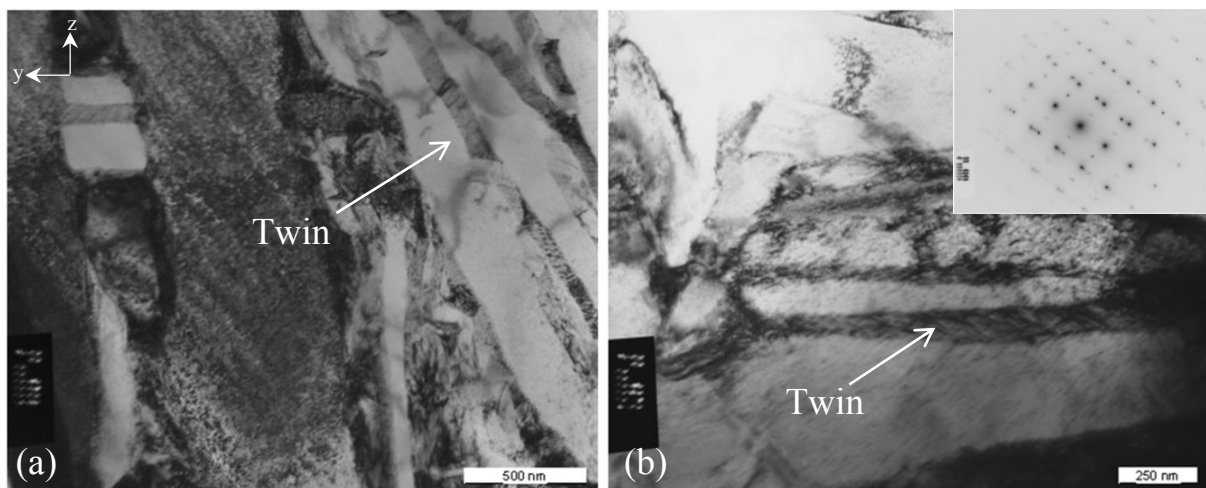
Figure 5.54: Microstructure of the coating generated at 6000 min^{-1}. Recrystallised twins can be seen which were heavily deformed (a, b).

The microstructure of the coatings with refined grains exhibits the formation of high dislocation density (Figure 5.56 a). Titanium oxides have been observed similar to the coatings with coarse grains, but the distribution of these oxides seems to be regular. The grain boundaries visible in Figure 5.56 b are straighter than the corrugated boundary in the coarse grain structure (Figure 5.53).
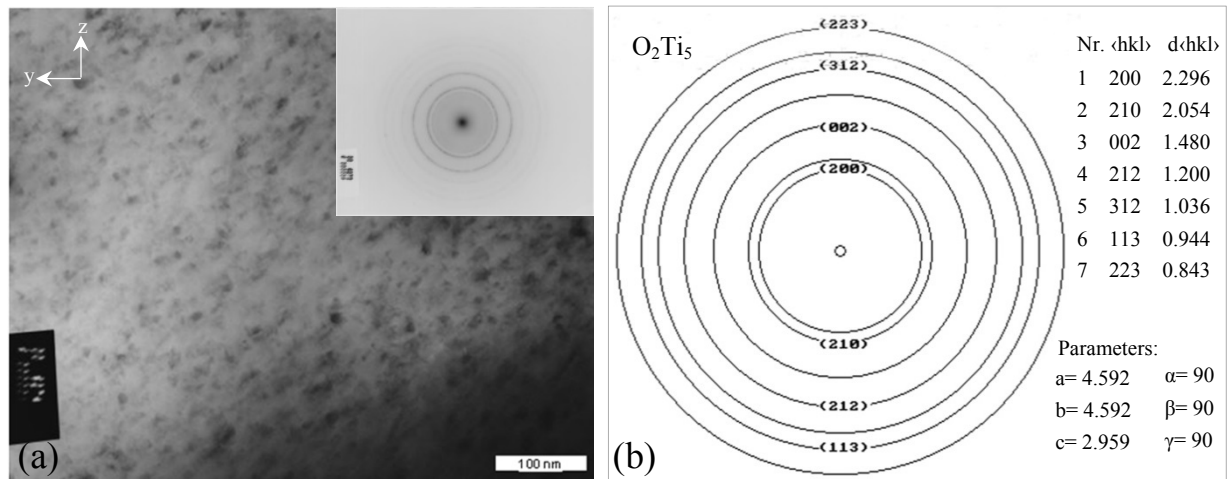
Figure 5.55: Microstructure of the coating generated at 6000 min^{-1} showing titanium oxides (a), and the analysis of the oxides (b).
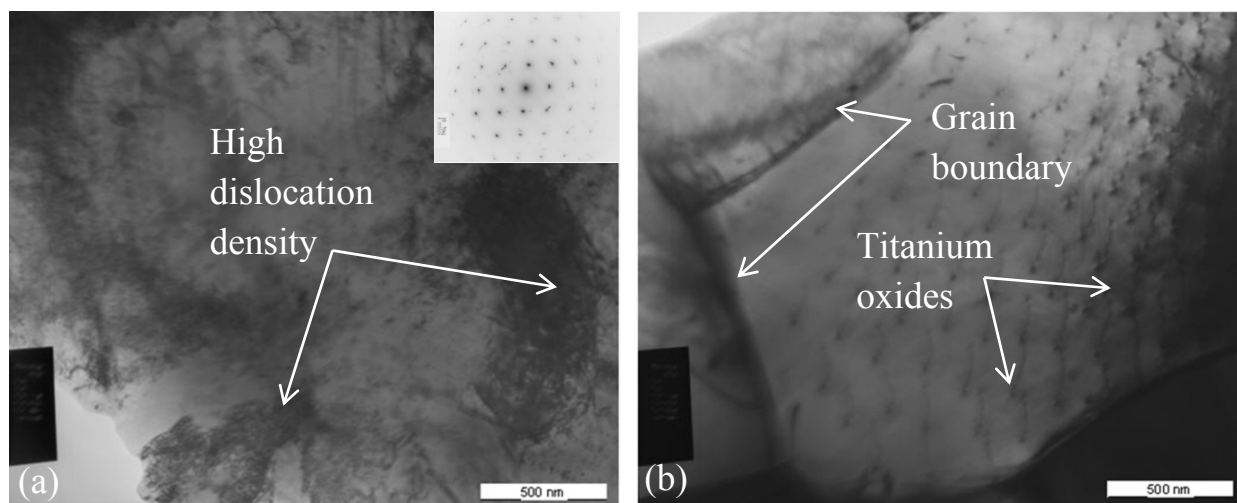

Figure 5.56: Microstructure with refined grains of the coating produced at 300 min^{-1} with corresponding diffraction image (a) and microstructure demonstrating titanium oxides (b).

In conclusion, it can be stated that formation of martensite does occur, in accordance with the high cooling rates during FS reaching the martensitic starting temperature, but it is not the only microstructure constituent. The α' martensite structure cannot be distinguished thoroughly due to the similarity of the α and α' crystallographic structures. Still, the presence of grains with low dislocation densities indicates recrystallisation or recovery processes, which are diffusion controlled, contrary to martensite formation. High dislocation densities and twins in other regions show, that also a considerable amount of residual strain is present. These findings correlate with the dynamic nature of the FS process, which induced dynamic recrystallisation in the coating material. The differences found represent locally varying states of residual strain and recovery at the instant when the material cooled down. The TEM

investigation did not reveal any β phase, supporting the EBSD results. The knowledge of formation of the titanium oxides will be important information in regard to further applications. The mechanical properties of Ti-alloys depend strongly on the morphology and state of the microstructure, so especially regarding possible future applications with cyclic loading conditions, further investigations and a thorough microstructure control may be required.

5.6 Mechanical Characterisation of Base Material and Coatings

In the previous section of this work, it was demonstrated that coatings produced by FS exhibit microstructures with different grain sizes, depending on the deformation and thermal conditions induced by the process. In detail, several tests, including micro hardness, micro flat tensile and fretting wear, were performed to investigate the mechanical properties of the generated coatings. Moreover, it was essential to investigate whether the mechanical properties of the coatings can be affected by the different process parameters. If so, the process parameters can be chosen adequately. The coatings produced under two different conditions, the low and high rotational speed regimes, were examined.

5.6.1 Tensile Test of Base Material

The round tensile samples were electro eroded from the bars of Ti-6Al-4V and Ti-Gr.1 materials in the longitudinal direction. The specimens were tested in the tensile testing machine at room temperature with a velocity of 1 mm/min. The force and length alteration data during the experiment were recorded. The ultimate tensile stress values obtained for Ti-Gr.1 lie in the range between 563 MPa and 571 MPa with an engineering elongation to fracture between 24.61% and 25.25 %. Ti-6Al-4V specimens achieved an ultimate tensile strength between 902 MPa and 917 MPa. The values for the engineering elongation to fracture lie between 12.95 % and 13.87 %. The stress values of the Ti-6Al-4V plate were obtained at 830 MPa ± 8 MPa with an engineering elongation to fracture of 12 % ± 2 %. The individual measurements of the tensile strength (R_m) and elongation results are presented in Table 5.1.

Table 5.1: Mechanical properties of the base materials.

	Material	Tensile strength [MPa]	Elongation to fracture [%]
Consumable rod	Ti-6Al-4V	910 ± 8	13.11 ± 1
Consumable rod	Ti-Gr.1	567 ± 3	25.06 ± 2
Plate	Ti-6Al-4V	830 ± 8	12 ± 2

5.6.2   Micro Hardness Testing

To investigate material properties of the deposited coatings hardness measurements were conducted. Hence, the hardness and ductility ratio of the material can be compared. Moreover, for future application of titanium coatings hardness values are strongly required.

Ti-Gr.1 Coatings

Micro hardness testing on the base material was conducted on the cross sections of the consumable rod. The hardness value of 188.49 ± 10.16 HV 0.2 was obtained by the measurements.

Micro hardness profiles of the coatings were carried out horizontally at mid-thickness through the entire coating width. Figure 5.57 presents average hardness values of the base material and coatings produced at different rotational speeds. It can be seen that the coatings exhibit a 26 % increase in hardness (237 ± 16 HV 0.2) compared with the base material. Moreover, the variation of the rotational speed did not influence the hardness.
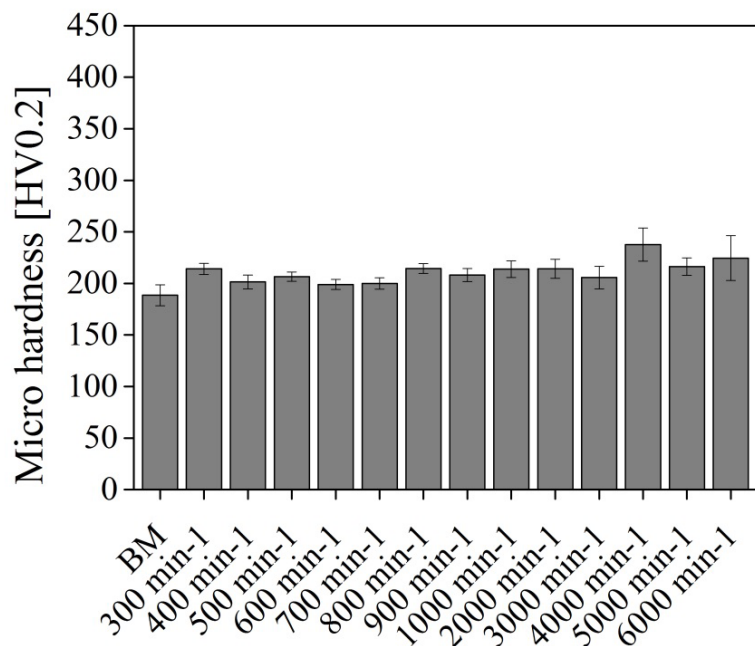
Figure 5.57: Micro hardness results of Ti-Gr.1 base material and coatings generated at various rotational speeds and at 16 mm/s deposition speed.

Additionally, hardness profiles were obtained vertically from the coating surface through the HAZ into the base material, to determine the hardness gradient. Because the hardness of Ti-Gr.1 is lower than that of the Ti-6Al-4V substrate, the hardness profile is presented to investigate the values in the HAZ. As expected, the hardness measured in the coating presents a low value, increasing in the HAZ (320 HV 0.2) and slightly decreasing in the base material

(300 HV 0.2) (Figure 5.58). The increased values in the HAZ can be related to the microstructure alteration during the deformation in the heat-affected zone (Figure 5.59).
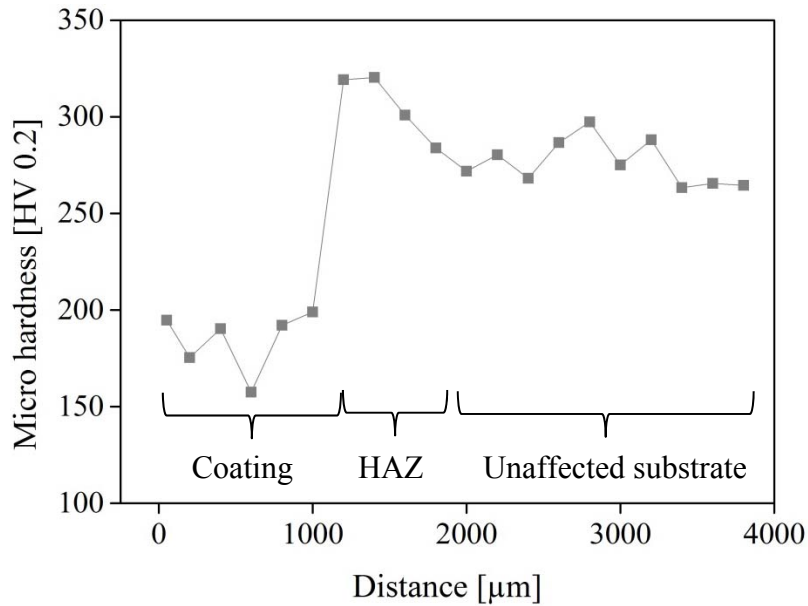

Figure 5.58: Measurement of a vertical hardness profile through the Ti-Gr.1 coating (produced at 3000 min^{-1} rotational speed), HAZ and substrate.
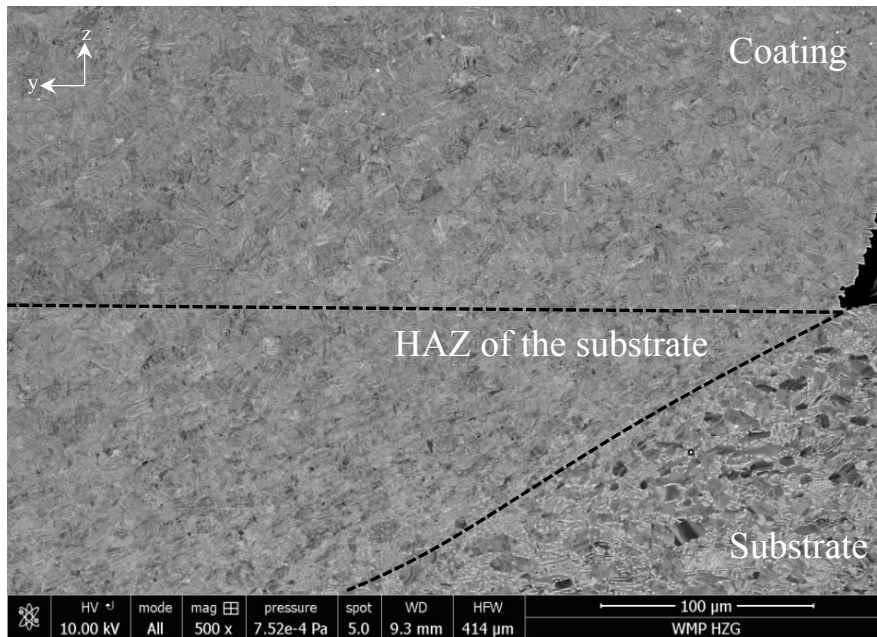

Figure 5.59: Deformed heat-affected zone of the substrate.

Ti-6Al-4V Alloy Coatings

The micro hardness investigation of the base material was carried out on cross sections of the rod, resulting in 305.1 ± 10.36 HV 0.2.

Micro hardness profiles were carried out within the coating produced at different rotational speeds horizontally in the middle of the coating thickness. Overall, the hardness values of the coatings up to 393.2 ± 23.86 HV 0.2 surpassed the hardness of the base material (305.1 ± 10.36 HV 0.2) by 28 % (Figure 5.60). The current hardness results are near the results obtained in the welding region that have been reported for friction welding, 398 ± 3 HV 0.2 [97]. No correlation was established with the hardness when varying the rotational speed. In FSW experiments, Zhang et al. showed that the hardness evolution varied with changing rotational speed [75]. Moreover, Figure 5.61 shows two measurements of the vertical hardness distribution, beginning near the coating surface and continuing through the HAZ until reaching the unaffected substrate region. The results indicate a hardness value within the coating of 328 ± 6 HV 0.2, and the hardness of the heat-affected zone is 316 ± 12 HV 0.2, exceeding the unaffected substrate hardness of 282 ± 15 HV 0.2.
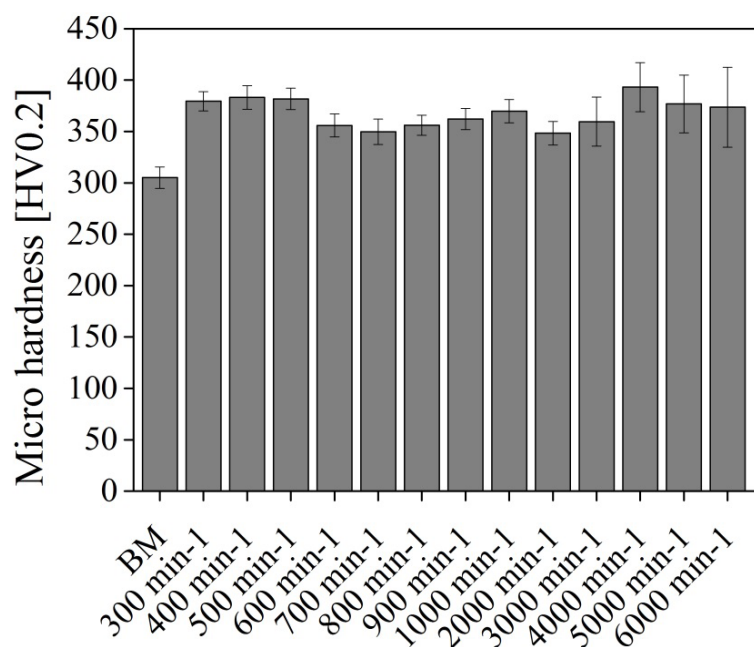

Figure 5.60: Micro hardness results of the Ti-6Al-4V base material and the coatings generated at various rotational speeds and at a deposition speed of 16 mm/s.

The hardness results of the coatings compared with the dilatometer samples are presented in Figure 5.62. It can be seen that when applying an identical thermal cycle, the coatings that have undergone plastic deformation show higher hardness compared with the dilatometer samples. Generally, the martensitic structure that develops in titanium alloys does not result in a considerable increase in hardness. It has been reported that the martensitic structure formed in titanium alloys is much softer than the martensite formed in Fe-C alloys. Carbon and nitrogen in Fe-C alloys cause a severe tetragonal distortion of the bcc lattice in the ferrous martensite, which leads to a significant increase in hardness. In contrast, the interstitial oxygen atoms in the titanium martensite cause a small elastic distortion of the hexagonal

lattice, with a marginal effect on the hardness [13] [9]. The TEM investigation demonstrated the high dislocation density formed within the microstructure. These two features could be the cause of the associated hardness increase in the coated material.

(a)

(b)

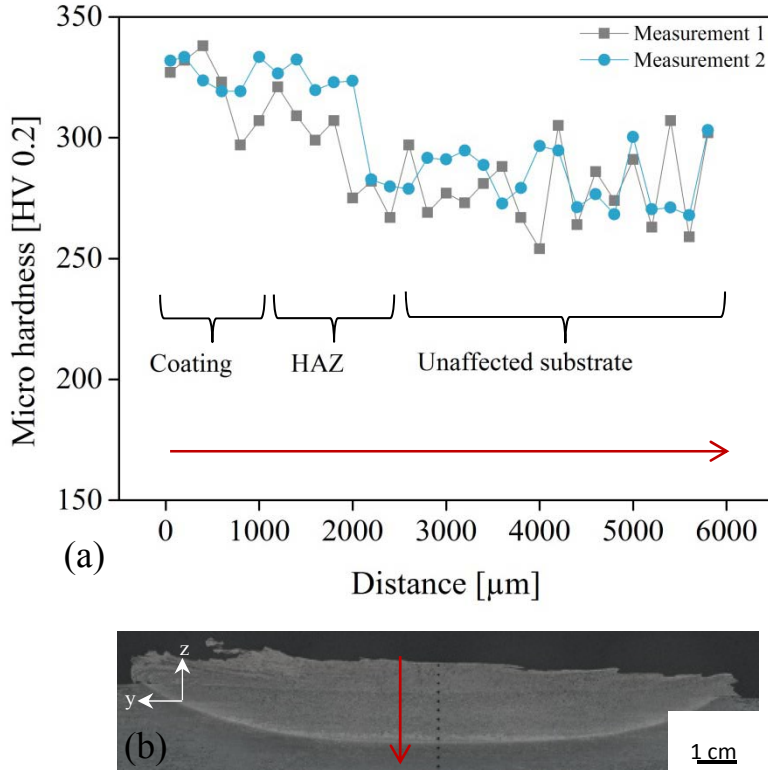Figure 5.61: Measurement of a vertical hardness profile through the coating (produced at 3000 min^{-1}), HAZ and substrate (a); corresponding cross section with hardness imprints (b).
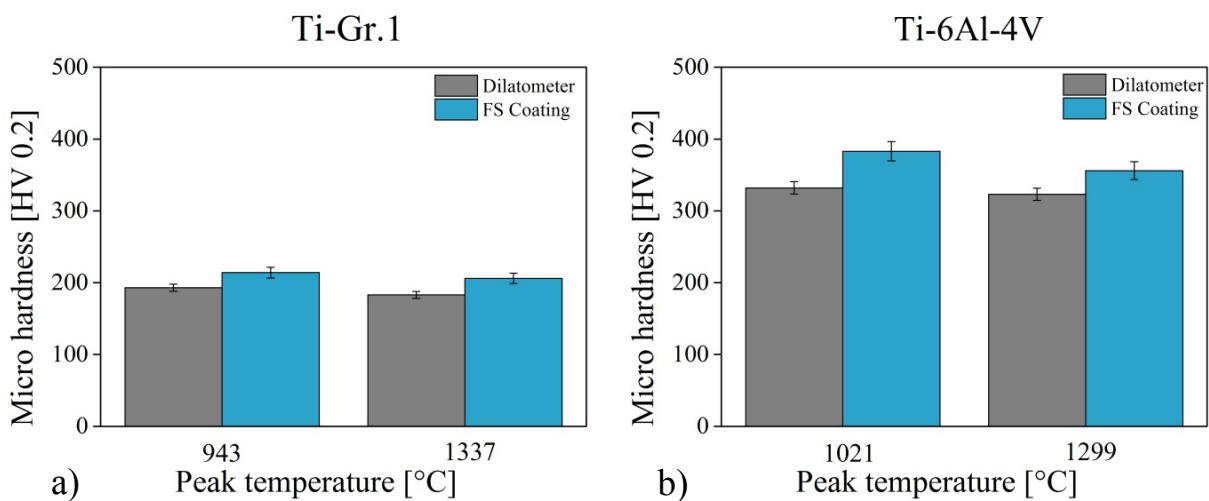

a)

b)

Figure 5.62: Micro hardness analysis of the coatings and dilatometer samples. Ti-6Al-4V (a) and Ti-Gr.1 (b) coatings exhibit higher hardness because of the high deformation even when the thermal cycle was identical.

5.6.3   Micro Flat Tensile Test

Micro tensile samples were machined by electro discharge machining (EDM) with measurements of 27 × 5 × 0.5 mm, as shown in the schematic in Figure 4.4. Samples from the base material and from coatings produced at high rotational speeds (3000 min^{-1} and 6000 min^{-1}) were investigated, because the coatings produced at a low rotational speed do not exhibit sufficient coating thickness for the micro tensile specimen geometry. The samples were eroded from the centre of the coating width and 0.1 mm above the substrate (Figure 4.5) to ensure that only the coated material would be tested. The processed specimens were tested parallel to the deposition direction.

Micro Flat Tensile Results and Fractography Examination of Ti-Gr.1 Coatings

The micro flat tensile samples of base material bars were tested in the longitudinal direction. The base material stress and strain results are shown in Figure 5.63. The ultimate tensile stress was 476 MPa ± 1.7 MPa with an average elongation to fracture of 32 % ± 2.1 %.

Two distinct conditions were tested: coating generated at 3000 min^{-1} and 6000 min^{-1} rotational speeds. As presented in Figure 5.63, the processed coating specimens exhibit an average ultimate tensile stress of 510 MPa ± 9.8 MPa and an elongation to fracture of 19 % ± 1.9 %. The alteration of the rotational speed does not affect the stress and tensile elongation properties of the coatings. The examined tensile stress and elongation behaviour of the coatings differ from those of the base material. Whereas the coatings demonstrate a slight increase in stress (510 MPa) compared with the base material (476 MPa), the tensile elongation of the coatings decreases significantly (19 %) relative to the base material (32 %). The fact that coatings exhibit higher strength and lower elongation is consistent with the mechanical behaviour results of materials that are plastically deformed [106-108]. The elongation to fracture decreases in plastically deformed materials due to the very high dislocation density in the microstructure [109].

The fracture surfaces and morphology of the coatings and base material on the micro flat tensile specimens were characterised. The images taken by SEM using the SE mode are displayed in Figure 5.64. The fracture surfaces of both are composed of dimples; however the base material exhibits more pronounced dimples. The dimple size of the base material is rather homogeneous, whereas the dimples of the coatings are irregular. Moreover, the dimple depth of the coating fracture surfaces seems to be shallow.

It can be seen that pure titanium material exhibits a ductile fracture mode. The fracture mode is governed by ductile stretching and tearing. Generally, the fracture mechanism of titanium is micro void coalescence and growth. The voids in Ti-Gr.1 are mainly nucleated at grain boundaries and grow by plastic stretching, eventually coalescing by ductile tearing of the ligaments between the voids [13].

Figure 5.63: Micro flat tensile test results of the Ti-Gr.1 base material and coatings generated at 3000 min^{-1} and 6000 min^{-1}.

Figure 5.64: Tensile fracture surface of Ti-Gr.1 presenting the base material (a) and coating generated at 3000 min^{-1} rotational speed (b).

Micro Flat Tensile Results and Fractography Examination of Ti-6Al-4V Coatings

Figure 5.65 exhibits the results of the base material from micro tensile tested samples with the engineering stress plotted against the engineering strain. The specimens have achieved ultimate tensile stress values from 985 MPa to 1034 MPa. The samples showed strongly dispersed strain values in the range of 12 % to 19 %.

The round tensile samples showed similar stress values for the base material of 1070 MPa ± 8 MPa at the elongation to fracture of around 15 %.
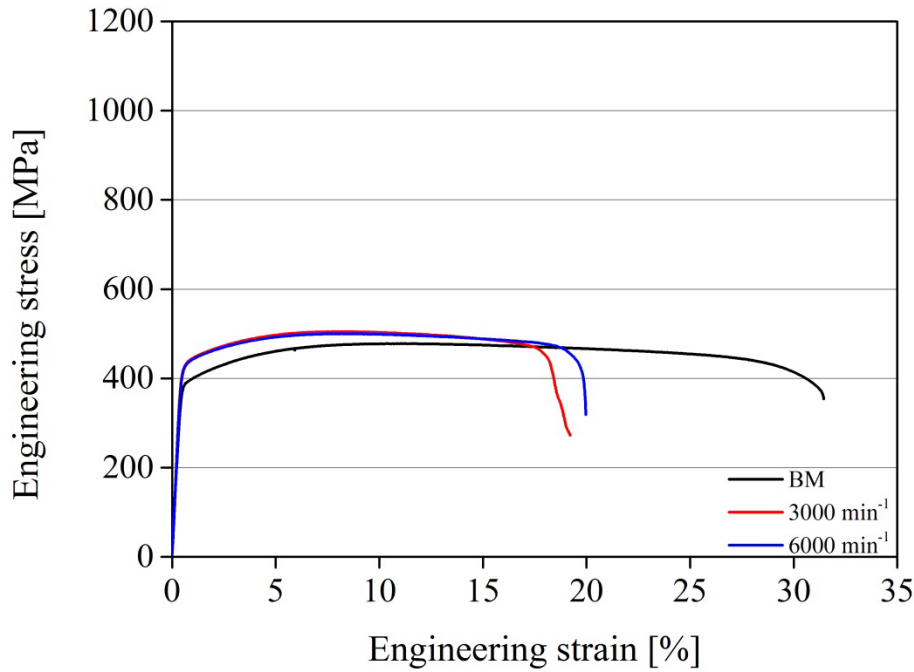

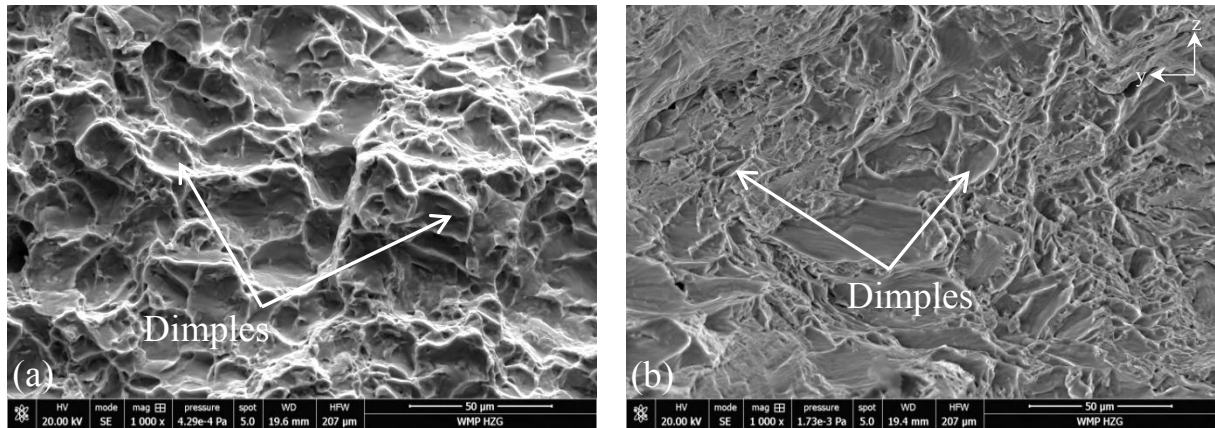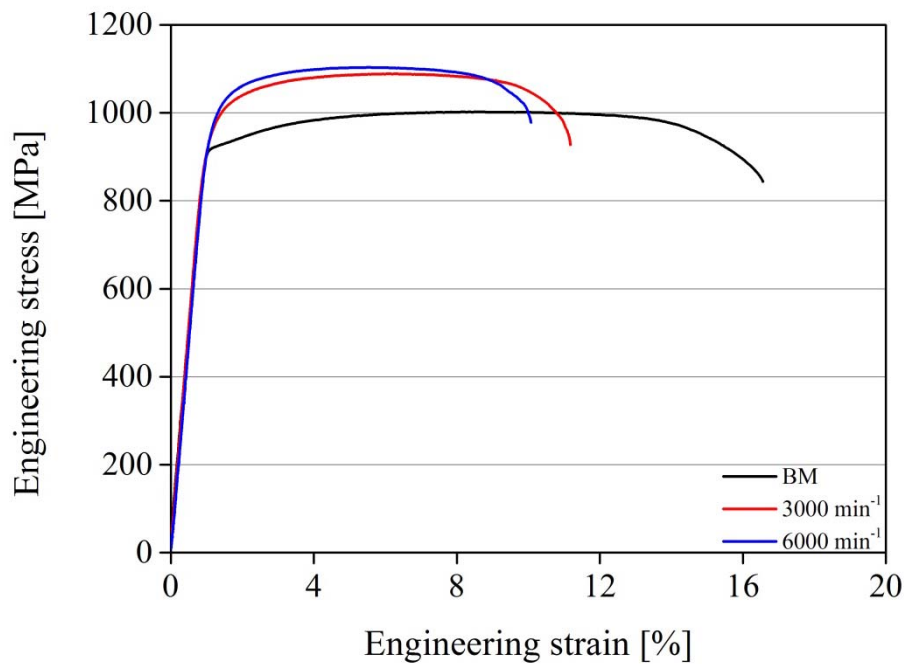Figure 5.65: Micro flat tensile test results of the Ti-6Al-4V base material and coatings generated at 3000 min^{-1} and 6000 min^{-1} rotational speeds.

The coatings processed at two different rotational speeds exhibit opposite results to the base material. The ultimate tensile stress values of the coatings, in both conditions surpass the values of the base material. Regarding the elongation to fracture, the coatings exhibit lower values, than the base material (Figure 5.65). Expressed in values, the ultimate tensile stress of the coatings increased from 985 MPa to 1100 MPa, and of the elongation to fracture showed a marginal reduction from 17 % (base material) to 11 % (coating). Both rotational speeds resulted in similar stress and strain performance. This loss in tensile elongation compared with the base material can be explained by the increase in hardness, which may be related to the high dislocation density and twin formation. It can be concluded that the coatings demonstrate a slightly higher strength but a lower ductility than the base material. Similar results regarding elongation to fracture (around 10.6 %) have been reported for Ti-6Al-4V welds produced by Friction Welding [97] and for material processed by severe plastic deformation [110].

The fracture surface analysis of the micro tensile tests was performed via SEM using the secondary electron mode. The micrograph presenting the fracture surface of the base material probe is depicted in Figure 5.66 a. The surface shows micro void coalescence resulting in fine dimples, typical of ductile behaviour.

The fracture surface of a coating produced at 3000 min^{-1} is shown in Figure 5.66 b. The dimples in the base material seem to be regular in size, whereas the dimples at the coating fracture are small in some regions and large in others. It can be seen that in both cases, a ductile intercrystalline dimple type of fracture occurs.

Micro tensile tests of Ti-Gr.1 and Ti-6Al-4V coatings exhibit similar behaviour with increased ultimate tensile stress compared with base material and a marginal reduction in elongation to fracture.
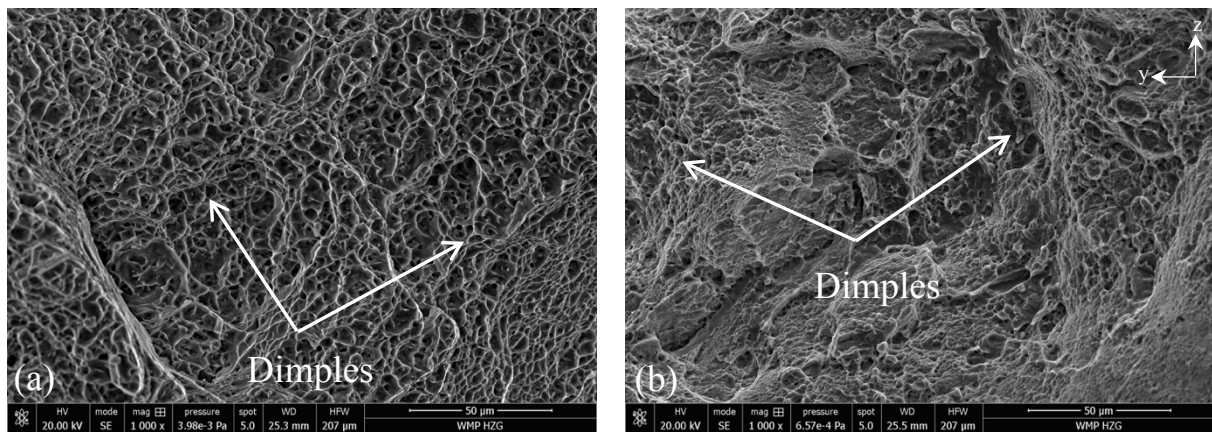

Figure 5.66: Tensile fracture surface of Ti-6Al-4V base material (a) and coating at 3000 min^{-1} (b). Both images exhibit dimples in the structure

5.6.4 Fretting Wear Test

The insufficient wear resistance behaviour of titanium alloys is well known, especially in application areas where oscillating motions occur e.g., in turbine blades and hip joints. Because friction surfacing offers a new possibility for generating titanium coatings, the wear behaviour of the processed material under oscillating load conditions was investigated.

The fretting wear experiments were conducted on polished coating top surfaces. The cross sections of the base material were taken as a reference material to examine the wear propagation.

The metallurgical preparation was described previously in subsection 4.5.1. The experiments were conducted with a ceramic sphere ZrO_2 as a counter body with a diameter of 32 mm under the dry condition. A schematic showing the test configuration is shown in Figure 5.67. Ti-6Al-4V was tested in its as-received condition. The coatings produced at different conditions exhibit microstructures either with refined grains or coarse grains. No impact of the grain size on the wear behaviour of the coatings could be noticed, so the following results are concentrated on the comparison of the Ti-6Al-4V base material and coatings with coarse grains. The test setting parameters are presented in Table 5.2.

Table 5.2: Setting parameters for the fretting wear experiment.

Normal force	35 N
Displacement	180 µm
Frequency	10 Hz
Sphere	ZrO_2
Diameter of sphere	32 mm
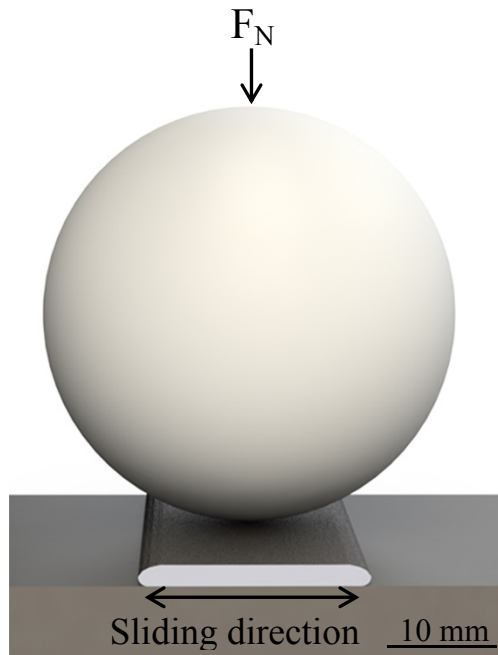
Figure 5.67: Schematic of fretting wear test configuration with a normal force F_N and sliding direction, demonstrating the ceramic sphere and titanium-based material.

Hysteresis Analysis

The test configuration includes a sphere and a flat rigid plate. The nominal contact area between the two parts is denominated as the Hertzian contact area, which is derived from the Hertzian stress [111]. High stresses are induced when a load is applied to the centre of the contact areas between two elastic solids [111]. The Hertzian contact area for the current experiments was determined to have a diameter of 360 µm for Ti-6Al-4V.

Tangential force, normal load and friction coefficient loops were plotted versus the displacement at different times (cycles) of the experiment. The loops were plotted at the beginning, in the middle and at the end of the experiment. The loops for both the base material and coatings for test duration of 500 cycles are presented in Figure 5.68. The normal load varied for both specimens in a range between 28 kN and 44 kN, exhibiting an oscillatory behaviour. Nevertheless, the oscillating normal load behaviour does not seem to severely

influence the tangential load. The tangential load exhibits a plateau in the middle of the stroke and peaks on the reversal point of the movement. At the forward run a high coefficient of friction is observed, which decreases on the return path and increases again when passing the middle of the displacement (Figure 5.68 c). The plateau of the base material that can be seen in the tangential force loops is also recognisable for the coefficient of friction. The coefficient of friction of the base material is constant over the entire test duration, exhibiting peaks at the reversal points. In that plateau phase, the coefficient of friction is low (~0.2) but it increases at the reversal points (~0.8).

The friction coefficient of the coating does not exhibit a similar plateau as the friction coefficient observed in the base material. The coefficient of friction is higher (0.6) on the forward run, and the peaks at the reversal point are lower compared with base material. On the return run, the coefficient of friction is lower (0.2) until the middle of displacement and then increases again, exhibiting similar behaviour to that in the other side of the loop. Moreover, the hystereses of the materials for the longest test duration of 1 Mio cycles are presented in Figure 5.69. A similar development of fluctuating normal force behaviour was also observed here. The tangential force and corresponding coefficient of friction of the base material seem to be slightly lower than those of the coating. The coefficient of friction for the base material and coating slightly decreases with the number of cycles. Still, the friction coefficient of the base material at 950k cycles is lower (0.4) than that of the coating (0.6).

The appearance of the hystereses presented in the current work differs from those published in the literature. Blanchard et al. observed three different types of tangential force-displacement hystereses: quasi-rectangular, closed and elliptic. Moreover, it has been demonstrated that displacement affects the tangential hysteresis shapes, resulting either in quasi-rectangular or closed shapes. When the displacement was set to ± 15 μm, closed hysteresis cycles were observed. When a displacement of ± 50 μm was applied, quasi-rectangular hystereses were created [112].

In the current work, the hystereses did not appear as those types (quasi-rectangular) reported in the literature. The tangential force hysteresis appearance is irregular in shape. The tangential force significantly increases on the forward and return runs without achieving a plateau. These irregular hysteresis appearances may be related to the comparably large displacement of 180 μm used in this work, compared to other studies, which is half the Hertzian contact diameter. The test parameters, including the large ZrO_2 sphere, were selected in accordance with the capabilities of the employed test rig. Also the material of the sphere plays an important role. Considering the Young' modulus of ZrO_2, it must experience less deformation compared with titanium resulting in a sort of ploughing action, which may explain the resultant hysteresis. Moreover, the amount of wear debris can ascent with increasing displacement and may thus lead to variations in hysteresis shapes.

Ti-6Al-4V Base material   Ti-6Al-4V Coating

(a)

(b)

(c)

Figure 5.68: Hystereses of normal force (a), tangential force (b) and friction coefficient (c) of Ti-6Al-4V base material and coatings (generated at 400 min^{-1}) for 500 cycles at various temporal stages (50, 250 and 450 cycles).

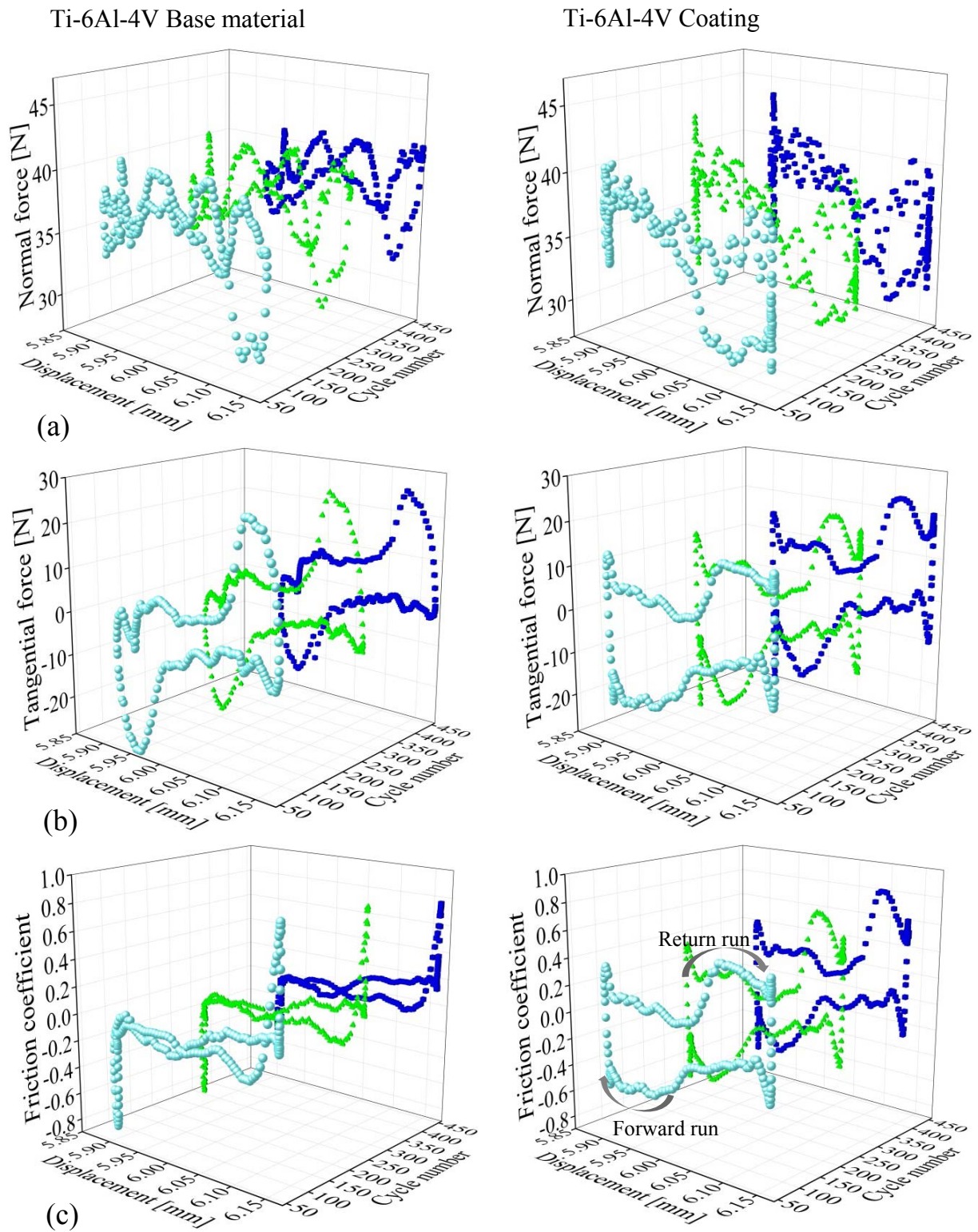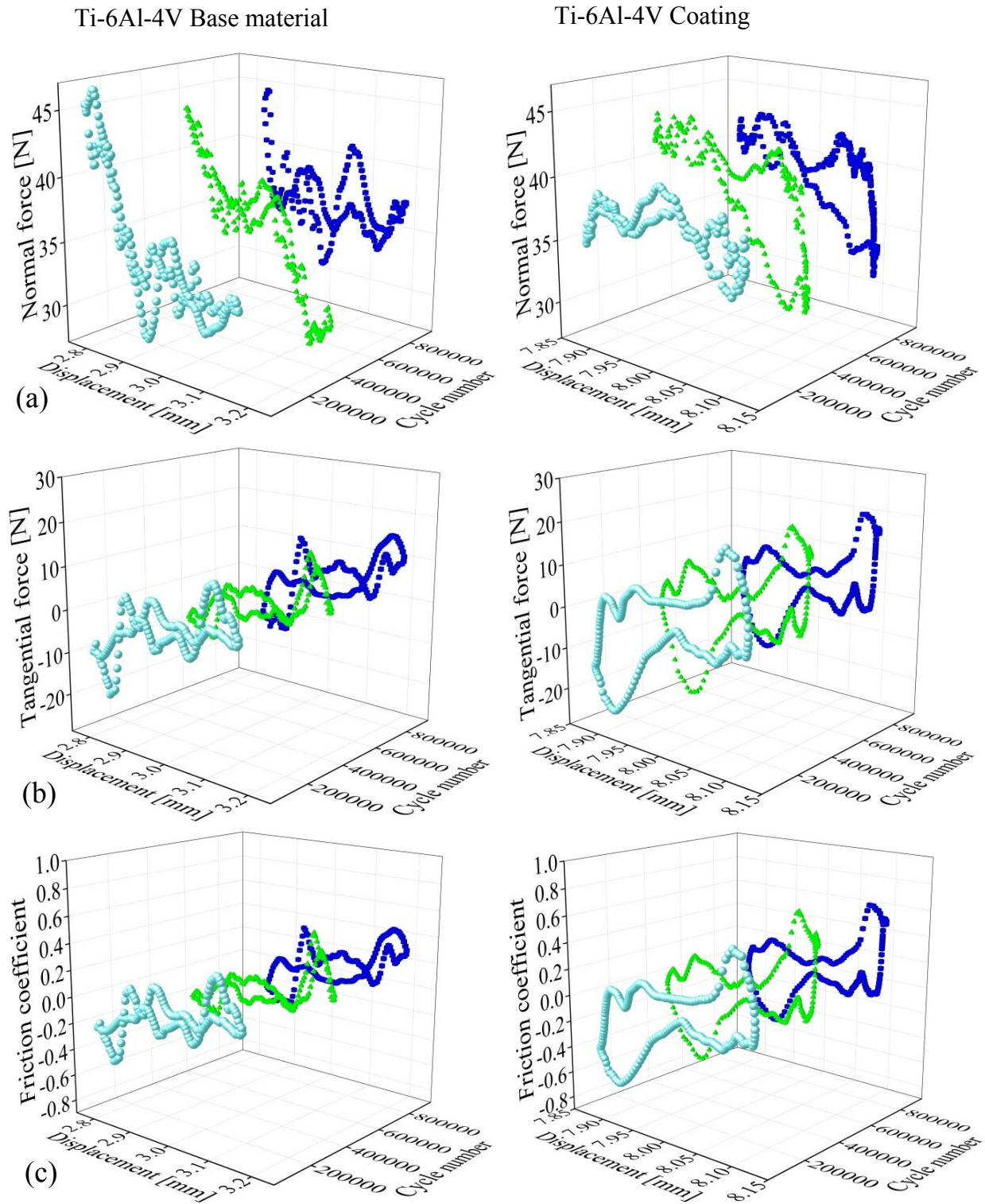Ti-6Al-4V Base material   Ti-6Al-4V Coating

Figure 5.69: Hystereses of normal force (a), tangential force (b) and friction coefficient (c) of Ti-6Al-4V base material and coatings (generated at 6000 min^{-1}) for 1Mio cycles at various temporal stages (5k, 500k and 950k cycles).

Surface Topographies

A confocal microscope allowing 3D surface measurements was used to determine the topography of the contact areas of specimens after wear experiments. For this purpose, an unworn surface region was defined as a reference surface. The protruded material of the surface in the contact area is defined as positive volume V_{wear}^+. Material loss below the reference surfaces was considered as negative wear volume V_{wear}^- [113].

Images of the surface topographies were captured from both bodies. A typical wear track on the coating (a) and a surface of the sphere (b) is displayed in Figure 5.70. It can be clearly seen that the entire wear track areas of both surfaces fit each other. The removed material in the shape of grooves on the coating can be found on the sphere surface as protruding material.

Groove

Adhering material

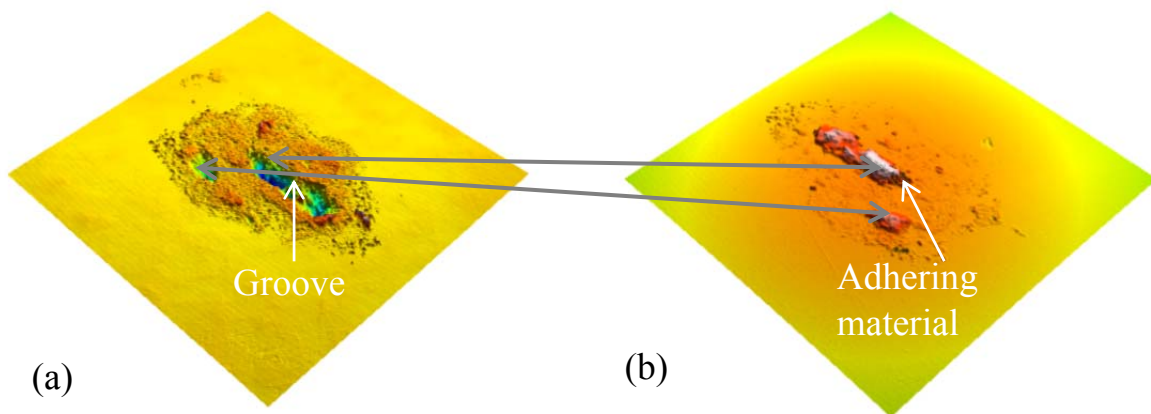(a)   (b)

Figure 5.70: Surface topographies of the coating (a) and sphere (b) post-wear conditions at duration of 50k cycles.

The profile measurements were taken parallel and perpendicular to the testing direction. All profiles exhibit material loss (cavities) in the contact area and material transfer at the outer edges of the wear scar. The wear depths of the base material and coatings measured perpendicular to the sliding direction are presented in Figure 5.71 and Figure 5.72, respectively. The profiles of the base material demonstrate a continuous roughening over the number of cycles, demonstrating the deepest wear track (4 µm) after 1 Mio cycles. The profiles of the coatings show that the wear depth first increases with the number of cycles from 100 to 50k. From 50k to 1 Mio cycles, the wear depth decreases, and the profiles exhibit protruded material on the surfaces. This might be due to the fact that the worn particles will be incised in the wear cavity, so the primary formed cavity is filled up again. It might be assumed that similar wear depth evolution occurs in the base material and coating after 1 Mio cycles; however, in the case of the base material, the wear particles seem to be ejected, and in the case of the coatings, they remain within the wear groove.
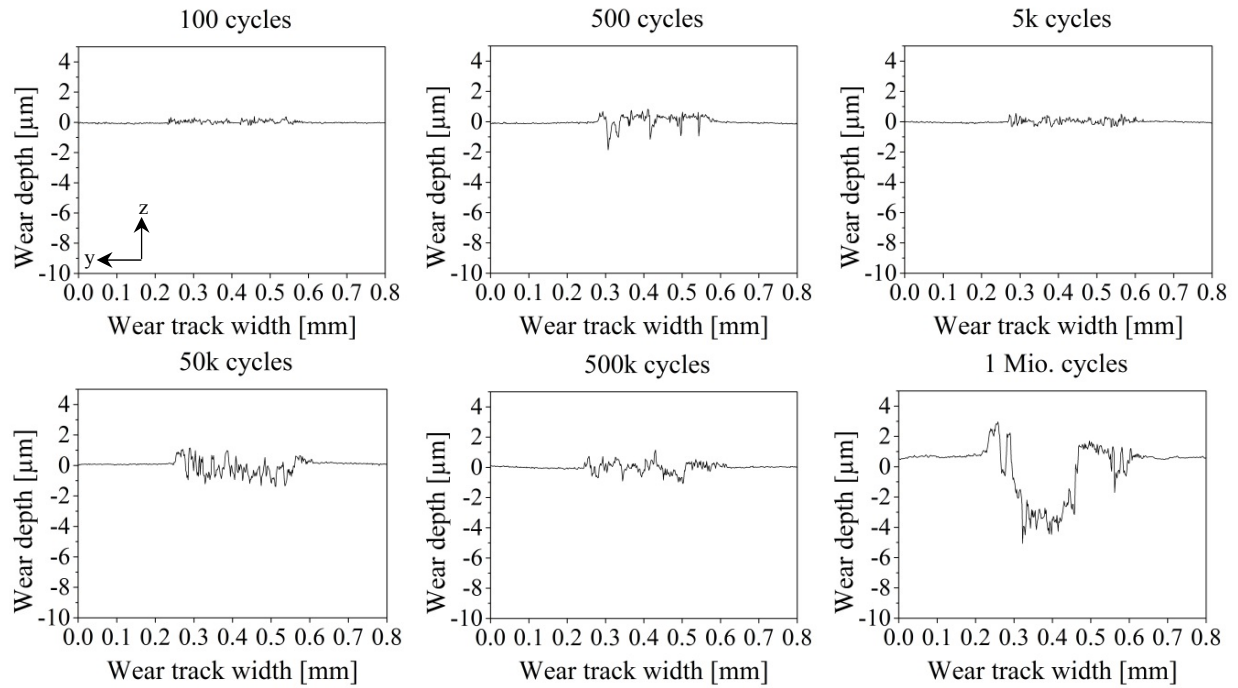
Figure 5.71: Wear depth of the base material at various numbers of cycles, measured perpendicular to the sliding direction.
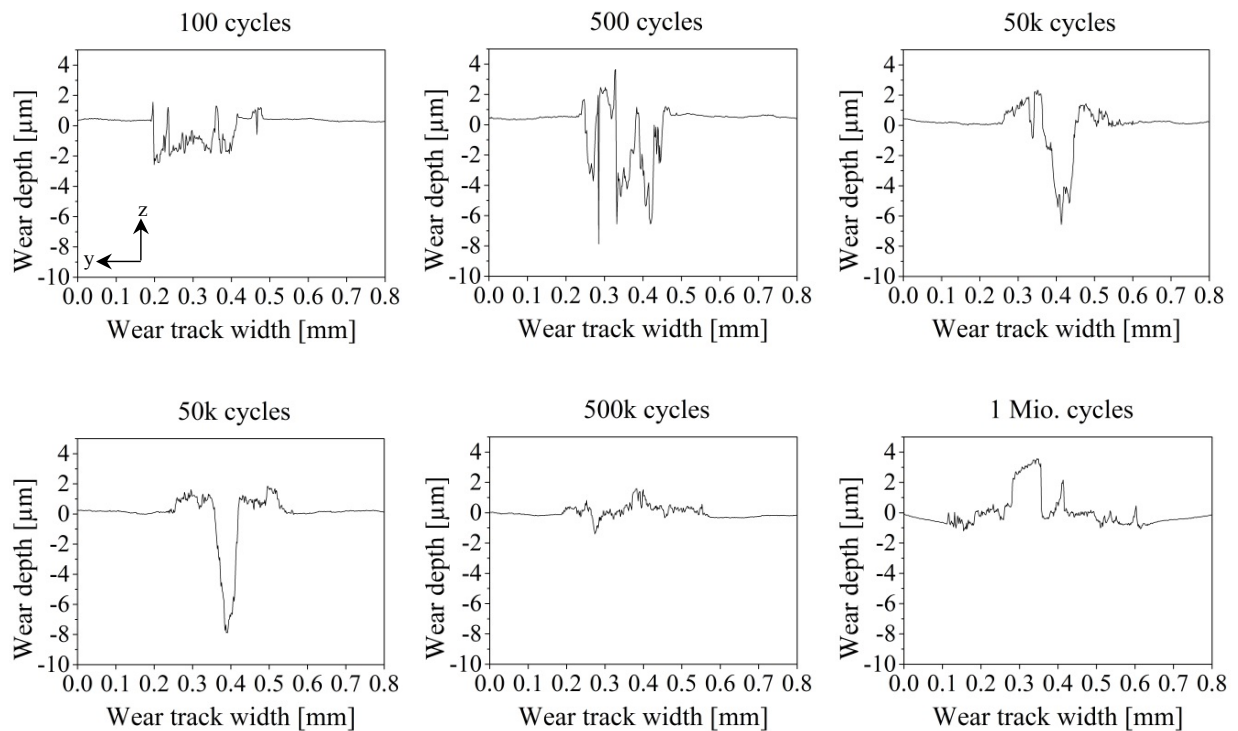

Figure 5.72: Wear depth of coatings with coarse grains generated at a 6000 min^{-1} rotational speed at various numbers of cycles, measured perpendicular to the sliding direction.

The surface topographies of the coating and base material after 1 Mio cycles are displayed in Figure 5.73. It can be clearly seen here that the wear debris of the coatings remained within the wear track, whereas wear debris of the base material are ejected, leaving a groove in the centre of the wear track. The possibility that wear particles remain within the wear groove might have a protective effect, hindering further material degradation [114].
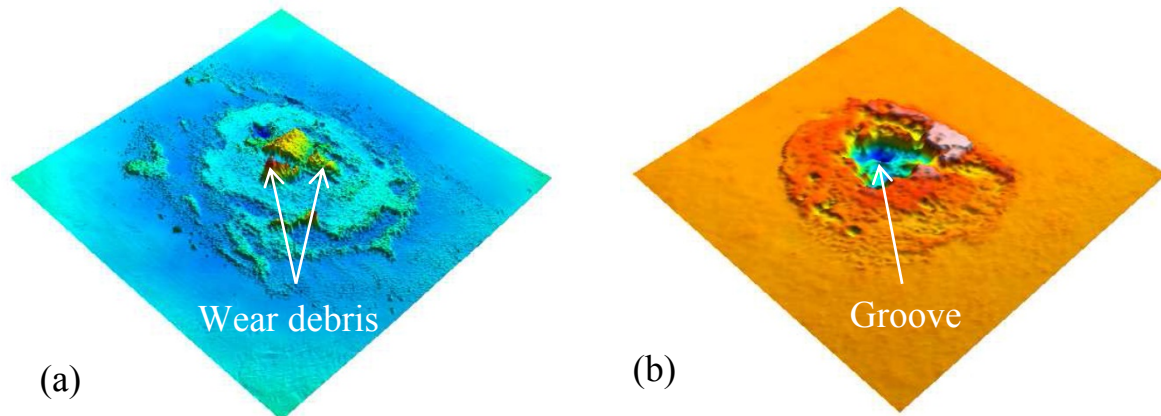

Figure 5.73: Surface topographies of the coating (a) and base material (b) post-wear condition at duration of 1 Mio cycles.

Characterisation of the Wear Tracks

The top surfaces of the wear tracks of the base material and coatings were examined by light microscopy and compared with regard to the shape. Light microscopy images of the top views of the base material and coatings for all durations of cycles are presented in Figure 5.74 and Figure 5.75, respectively. The sequence of the images shows that the wear track area does not enlarge with increasing duration of the experiment. The generated contact area fits well into the determined Hertzian contact area. At the first stage of the experiment, a discontinuous contact area was observed, demonstrating wear-unaffected material in some regions. In all images, the worn surface exhibits a continuous contact area with a circular shape. Wear particles are presented in the contact area surroundings, especially in the testing direction. It can be seen that the wear debris is transferred to the sphere and built up on it (Figure 5.70 b), which might lead to unworn areas within the wear track, where the contact with the counter body was precluded.

Cross Section of Wear Tracks

To analyse the wear depth thoroughly, cross sections of the wear scars of the base material and coatings generated at 6000 min^{-1} were prepared. Cross sections of the coatings are presented in Figure 5.76. The wear mechanism distribution can be observed at different cycles.
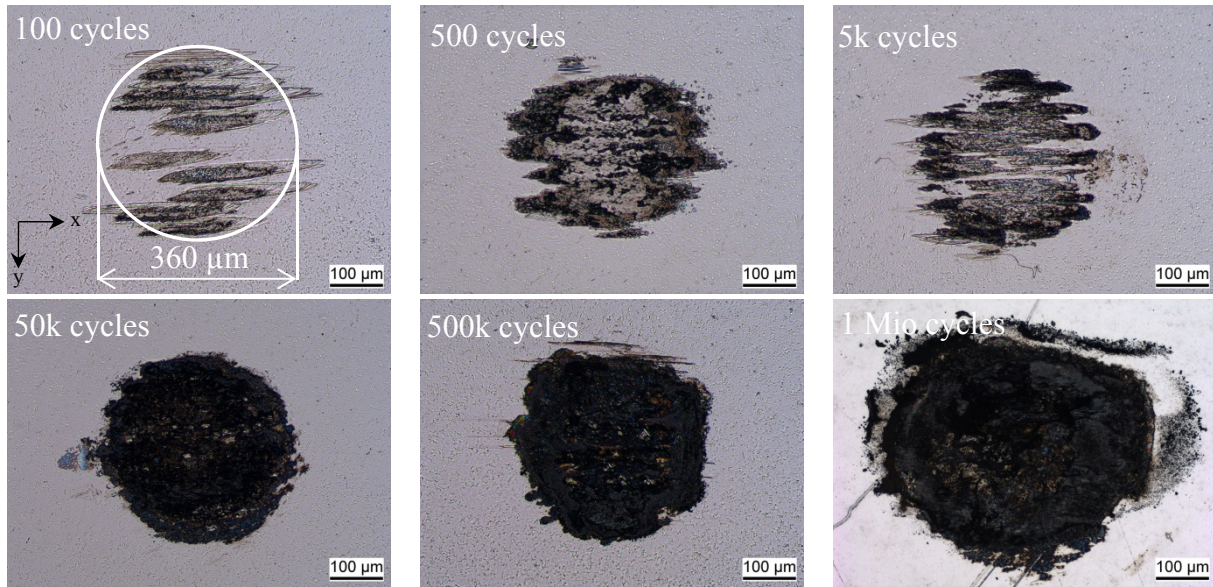
Figure 5.74: Top view of the base material wear tracks generated at different cycles exhibiting the Hertzian contact area.
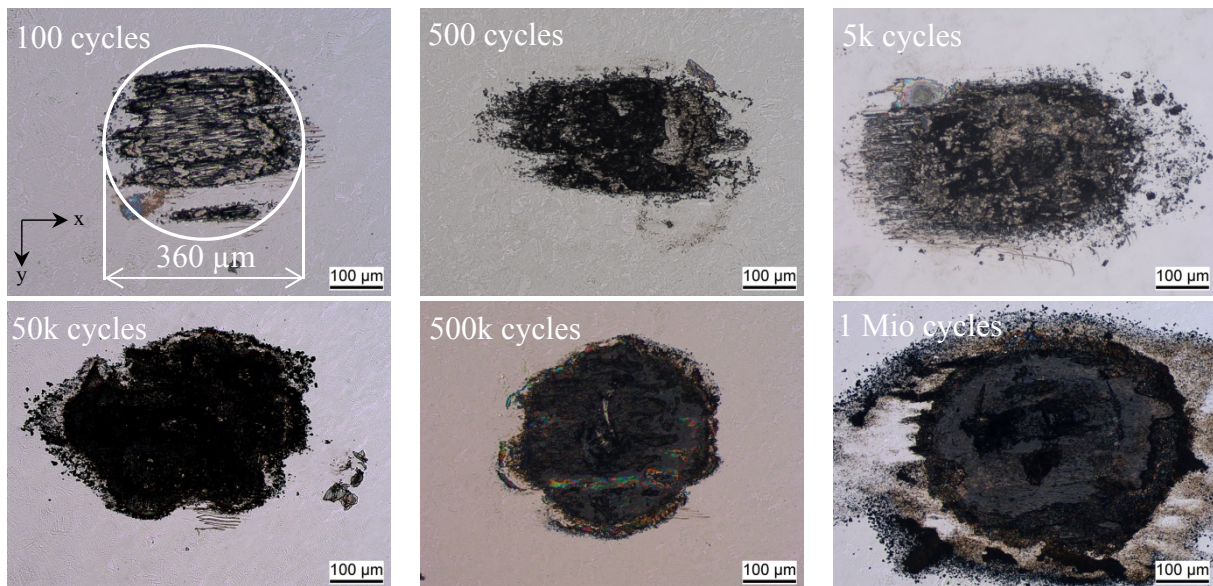
Figure 5.75: Top view of the wear tracks from the coatings generated at a 6000 min^{-1} rotational speed exhibiting the Hertzian contact area.

It can be seen that the wear depth of the coatings increases drastically until reaching 500k cycles. Similar observations have been reported in the literature, showing a continuous wear rate increase with advancing number of cycles [114, 115]. By further doubling the cycles (1 Mio), the wear depth does not increase significantly. It seems that the wear groove formed at this cycle condition is sufficiently deep, precluding the ejection of generated debris. Hence, it may be assumed that wear debris is collected in the wear groove, creating a new layer formed from debris.

The images exhibit how the wear scars evolve during the various numbers of cycles:

- Roughness increases due to the primary material loss after 100 cycles (Figure 5.76 a).
- After 5k cycles, cracks 5 μm under the surface are identified, extending along the length of the wear scar (Figure 5.76 b).
- After 50k cycles a deep groove (9.19 μm) in the middle of the wear scar appears, and at the sides, cracks are observed again; however, the material above the cracks does not exhibit the same structure as the coating below the crack (Figure 5.76 c).
- After 1 Mio cycles, the wear scar shows a groove with a depth of 10.69 μm, which 3 μm is compacted wear debris and cannot be counted as wear depth (Figure 5.76 d). Additionally, at the edges of the wear scar, compacted wear debris can be seen. It seems that once a certain wear depth is achieved and, ejecting the wear debris to the outer edges because of the oscillating motion, the worn particles transfer again into the wear groove and are indented (Figure 5.77). It can be assumed that the indented wear debris represents a sort of movable roughness hill, which will be transferred from one region to the other during the experiment, so the material below remains unaffected.
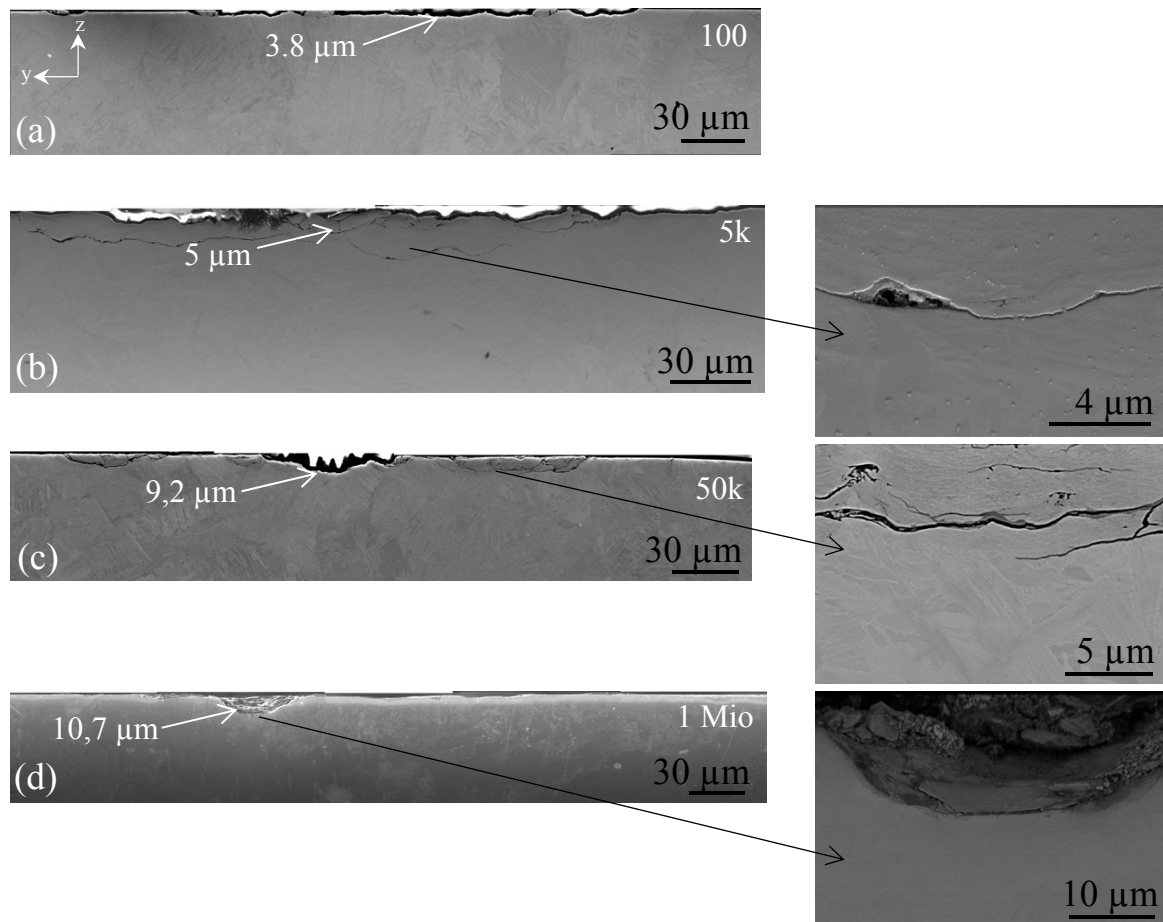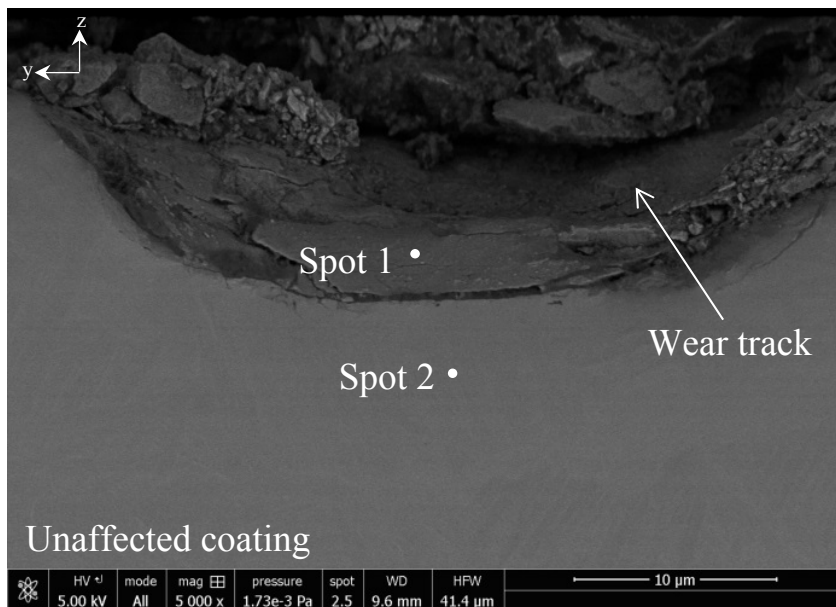

Figure 5.76: Cross sections through wear tracks after different numbers of cycles perpendicular to the sliding direction on coatings produced at 6000 min^{-1} rotational speed.

Element analysis was conducted on the cross sections of the wear tracks (Figure 5.77). Zr from the sphere was found, and the amount of oxygen detected far exceeds the 1:2 ratio from ZrO_2 (26 atomic% O, compared with 1.6 atomic% Zr). Clearly, titanium oxides formation occurred at the bottom of the wear track after 500k and 1 Mio cycles. The high amount of carbon and nitrogen may result from the environment, too. The formation of the oxides, especially of rutile titanium oxides in fretting test surfaces, has also been observed by Hager et al. [59]. Moreover, the presence of the rutile titanium in the contact area has a lubricous effect and can preclude further crack propagation [116-118]. After achieving a certain number of cycles, the rutile titanium is formed, leading to a reduction of the friction [59]. Similar findings were made in the current work, indicating a reduction in wear depth propagation at a high number of cycles when the titanium oxides formed. Moreover, the coefficient of friction after 500k cycles decreased, slightly indicating that the titanium oxide formation has a lubricous impact.

Region	C	N	O	Al	Zr	Ti	V
Spot 1	5.87	4.89	14.55	11.18	4.91	55.6	2.99
Spot 2	1.45	5.07	-	10.7	-	79.44	3.34

Figure 5.77: Cross section through wear track generated with 1 Mio testing cycles of a coating generated at 6000 min^{-1}. The image exhibits deformed wear particles and titanium oxides formed in the wear groove. The elements in the table are given in wt. %.

Sphere Analysis

SEM images of the wear tracks on spheres were also captured from the top view (Figure 5.78). As anticipated, it can be seen that material lost from the counter body can be found on the sphere. Furthermore, cracks on the ceramic spheres were observed after 5k cycles or more.

Element analysis by the EDS technique was carried out on the sphere's wear tracks. Titanium oxides were formed at the sphere surfaces after 500k cycles. Figure 5.79 shows a ceramic sphere surface after 1 Mio cycles of fretting wear testing and EDS analysis were conducted. Two regions of the sphere were analysed performing an element analysis at the surface where no debris was transferred (Spot 2) and at the area exhibiting oxidised wear debris within the contact area (Spot 1).
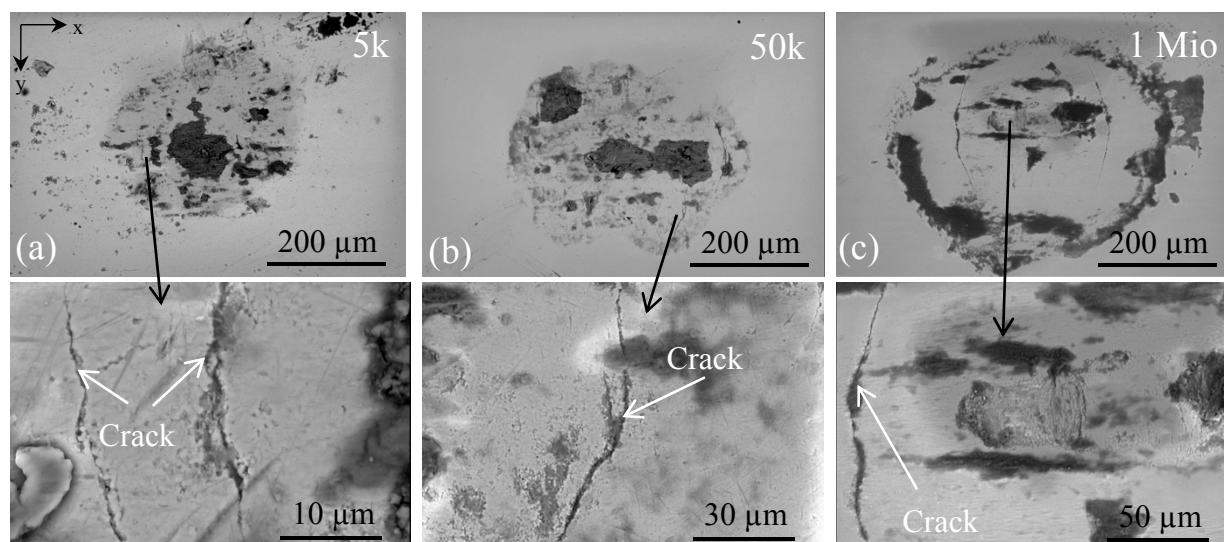
Figure 5.78: Crack initiation at the surfaces of ZrO_2 spheres after different cycles, and respective images at high magnification.
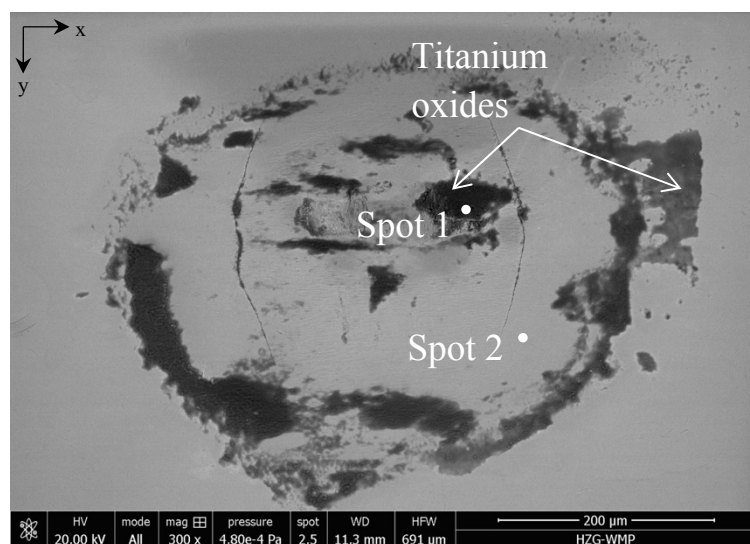
	Element	Weight [%]
Spot 1	C	7.98
	Al	7.35
	Zr	5.77
	O	47.19
	Ti	35.31
Spot 2	Zr	65.13
	O	34.87

Figure 5.79: EDS analysis at the sphere surface showing the formation of titanium oxides.

It can be concluded that Ti-Gr.1 and Ti-6Al-4V coatings presented comparable evolution of the fretting wear, showing formation of compacted wear debris over time and titanium oxides which may have a lubricious effect. Additionally, the base material and the coatings exhibit similar wear behaviour. Therefore, friction surfacing of titanium can be used as a repair method.

6 Conclusions

Friction surfacing is a relatively novel joining technology with a great potential to be applicable for deposition of various metallic materials. The processing of each new introduced material combination is rather challenging and significant; unexpected differences in material behaviour are regularly observed. Therefore, each new material combination can contribute to a more comprehensive understanding of the FS process.

In the current work, successful deposition of titanium alloy coatings by friction surfacing was demonstrated. During process development flash formation at the coatings, which has not been reported so far for any other materials, was investigated. Differences in the material behaviour in two rotational speed regimes were identified, which was only possible because an extensive parameter range was applied. Another important point of this work was the investigation of resultant microstructural and mechanical properties. The following conclusions are grouped into process development, characterisation of the coatings, and microstructural and mechanical examinations.

Process Development

The current study has demonstrated a thorough process development for the generation of Ti-6Al-4V and Ti-Gr.1 coatings by FS. The coatings have been deposited successfully in a wide range of process parameters. The use of the consumption rate control mode instead of conventional force control for depositing titanium coatings turned out to be a suitable mode due to the susceptibility to force and plastic flow instability of the material. The rotational speed has been varied in a broad spectrum. Two regimes of the rotational speed have been established.

In the first regime, flash generation at the coating may occur at certain combinations of the rotational and deposition speeds. Both parameters are responsible for the temperature development and strain rates that affect the material flow stresses while depositing, resulting either in domination of thermal softening (flash generated at the coating) or flow stability (flash formed at the rod).

In the high rotational speed regime, the temperature achieves its maximum. Here, the flash generation at the coating is precluded, and an alteration of rotational speed and deposition speed does not influence the temperature distribution significantly.

Characterisation of the Coatings

The geometry of the coatings varies with changing rotational speed and resultant axial force. The employment of low rotational speeds requires high axial forces that lead to deposition of thin and wide coatings. In contrast, the employment of high rotational speeds results in low

axial forces that generate thick and narrow coatings. In this context, the deposition efficiency varies with changing rotational speed and resultant forces. The highest deposition efficiency was 38 % for Ti-6Al-4V and 52 % for Ti-Gr.1 when employing a high rotational speed.

Microstructure Evolution

The temperature history based on the thermocouples and thermal camera examinations have shown that the peak temperature exceeds the beta transformation field in all experiments. The temperature achieves its peak during the plastification phase, followed by a steady state. The temperature evolution, including the peak temperature and heating rate, is affected by the rotational speed.

Due to the fact that the process temperature exceeds the transformation temperature, the material is deformed in the beta phase. Here, during processing, dynamic recrystallisation takes place. While cooling, Ti-6Al-4V passes the temperature field of martensitic initiation. Therefore, the phase transformation of the coatings occurs martensitically because of the high cooling rate, so no diffusion occurs. Furthermore, the influence of the combination of strain, strain rate and temperature on the recrystallised β grain size has been observed. It has been shown that by using a low rotational speed and the resultant low temperatures, the grains become refined relative to the base material. By raising the rotational speed, the temperature increases, and the grains become coarse. With an additional rise in rotational speed, the temperature does not increase any further, and the additional grain growth is precluded.

Moreover, the separation of the thermal cycles from the deformation induced on the coatings by FS have been realised via dilatometer tests. It has been demonstrated with the dilatometer results that the employment of such high temperatures in titanium samples leads to grain growth which is even more predominant when increasing the temperature. The grain growth is less pronounced when using identical temperatures with additional deformation applied by the FS process.

Mechanical Properties

The mechanical properties of the coatings have been examined by micro hardness analysis, micro flat tensile measurement and investigation of the fretting fatigue behaviour. The micro hardness behaviour of the pure titanium coatings has not been affected significantly by the process because no martensitic structure has been formed. Conversely, Ti-6Al-4V coatings have featured a hardness increase of approximately 15 % with respect to the martensitic structure formed by FS and high dislocation density, as observed by TEM analysis.

The micro flat tensile experiments have been conducted on coatings and the base material. The tensile strength of the coatings has been increased along with a loss in ductility.

It could be seen that the fretting wear evolution can be divided into three regimes. First, the cracks are propagated, then the material above the cracks is deformed during the tests, and finally, the particles lost from the initiated cracks are used as filler material for the worn grooves. The filled grooves avoid further wear of the matrix, and these agglomerated particles can be seen as movable hills, protecting the matrix. The fretting wear behaviour of the coatings and base material are similar. The coating properties with regard to wear behaviour cannot be improved. However, the wear behaviour is still comparable so that, friction surfacing can be used as a repair method.

The mechanical properties of the coatings presented in the current study have demonstrated fretting wear behaviour that is at least similar to that of the base material. The micro tensile results of the coatings have shown higher strength and lower ductility than the base material. Fusion-welded materials rarely achieve the mechanical properties of the base material [9].

The failure to deposit titanium coatings by friction surfacing reported in previous publications has been overcome in the current study. Furthermore, it was shown that, given the proper control mode, coatings of various dimensions can be produced at high quality and reproducibility. The coatings exhibit encouraging results regarding mechanical properties. This work has opened up the new possibility and knowledge to apply friction surfacing for titanium alloys, which can be effectively used for repair of worn or damaged parts.

7 References

[1]   Klopstock H, Neelands AR. An improved method of joining or welding metals, British Patent Specification No. 572789 (1941).

[2]   Nicholas ED, Thomas WM. Metal deposition by friction welding, Welding Journal, 13 (1986) 17-27.

[3]   Miranda RM, Gandra J, Vilaça P, Quintino L, Santos TG. Surface modification by solid state processing, Woodhead Publishing (2014).

[4]   Gandra J, Krohn H, Miranda RM, Vilaça P, Quintino L, dos Santos JF. Friction surfacing—A review, Journal of Materials Processing Technology, 214 (2014) 1062-93.

[5]   http://www.frictec.com. Frictec Ltd, United Kingdom. 14.04.2016.

[6]   Dilip JJS, Babu S, Rajan SV, Rafi KH, Ram GDJ, Stucker BE. Use of Friction Surfacing for Additive Manufacturing, Materials and Manufacturing Processes, 28 (2013) 189-94.

[7]   Sakihama H, Tokisue H, Katoh K. Mechanical properties of friction surfaced 5052 aluminum alloy, Materials Transactions, 44 (2003) 2688-94.

[8]   Rafi KH, Ram JGD, Phanikumar G, Rao PK. Microstructure and Properties of Friction Surfaced Stainless Steel and Tool Steel Coatings, Materials Science Forum, 638 (2010) 864-69.

[9]   Peters M, Leyens C. Titan und Titanlegierungen, Weinheim, WILEY-VCH Verlag GmbH & Co. KGaA (2002).

[10]   Rao KP, Sankar A, Rafi HK, Ram GDJ, Reddy GM. Friction surfacing on nonferrous substrates: a feasibility study, The International Journal of Advanced Manufacturing Technology, 65 (2012) 755-62.

[11]   Wu H, Feng J, He J. Microstructure evolution and fracture behaviour for electron beam welding of Ti–6Al–4V, Bulletin of Materials Science, 27 (2004) 387-92.

[12]   Huang C, Zhang Y, Vilar R, Shen J. Dry sliding wear behavior of laser clad TiVCrAlSi high entropy alloy coatings on Ti–6Al–4V substrate, Materials & Design, 41 (2012) 338-43.

[13]   Lütjering G, Williams JC. Titanium, Springer-Verlag (2007).

[14]   Bombac D, Brojan M, Krkovic M, Turk R, Zalar A. Characterization of titanium and stainless steel medical implants surfaces, Materials and Geoenviroment, 54 (2007) 151-64.

[15]   Gottstein G. Rekristallisation metallischer Werkstoffe: Grundlagen, Analyse, Anwendung, Deutsche Gesellschaft für Materialkunde e.V. (1984).

[16]   Sieniawski J, Ziaja W. Titanium Alloys - Advances in Properties Control, InTech (2013).

[17]   Seshacharyulu T, Medeiros SC, Frazier WG, Prasad YVRK. Unstable flow during supratransus working of Ti–6Al–4V, Materials Letters 47 (2001) 133-9.

References

[18]   Arulselvan M, Ganesan G. Hot deformation behaviour of Ti-6Al-4V in different strain rates, International Journal of Innovative Research in Advanced Engineering, 1 (2014) 207-12.

[19]   Seshacharyulu T, Medeiros SC, Frazier WG, Prasad YVRK. Hot working of commercial Ti-6Al-4V with an equiaxed alpha-beta microstructure: materials modeling considerations, Materials Science and Engineering A, 284 (2000) 184-94.

[20]   Bruschi S, Poggio S, Quadrini F, Tata ME. Workability of Ti–6Al–4V alloy at high temperatures and strain rates, Materials Letters, 58 (2004) 3622-9.

[21]   Sulijoadikusumo AU, Dillon Jr. OW. Metallurgical Effects at High Strain Rates, Springer (1973).

[22]   Kaya Y, Kahraman N. An investigation into the explosive welding/cladding of Grade A ship steel/AISI 316L austenitic stainless steel, Materials & Design, 52 (2013) 367-72.

[23]   Chandrasekaran M, Shivalingappa D. Recent Developments in Cladding Process – A Review, International Journal for Innovative Research in Science & Technology, 2 (2016) 310-5.

[24]   Ajdelsztajn L, Jodoin B, Schoenung JM. Synthesis and mechanical properties of nanocrystalline Ni coatings produced by cold gas dynamic spray, Surface and Coatings Technology, 201 (2006) 1166-72.

[25]   Li WY, Zhang C, Guo X, Xu J, Li CJ, Liao H, et al. Ti and Ti-6Al-4V Coatings by Cold Spraying and Microstructure Modification by Heat Treatment, Advanced Engineering Materials, 9 (2007) 418-23.

[26]   Graf B, Gumenyuk A, Rethmeier M. Laser metal deposition as repair technology for stainless steel and titanium alloys, Physics Procedia, 39 (2012) 376-81.

[27]   Rasheedat MM, Esther TA, Shukla M, Pityana S. Laser Metal Deposition of Ti6Al4V: A Study on the Effect of Laser Power on Microstructure and Microhardness, Proceedings of the International MultiConference of Engineers and Computer Scientists, II (2013).

[28]   Kelly SM. Thermal and Microstructure Modeling of Metal Deposition Processes with Application to Ti-6Al-4V, PhD Thesis, Virginia, Virginia Tech (2004).

[29]   Grainger S, Blunt J. Engineering Coatings: Design and Application, Abington Publisher (1998).

[30]   Hanke S, Beyer M, Silvonen A, dos Santos JF, Fischer A. Cavitation erosion of Cr60Ni40 coatings generated by friction surfacing, Wear, 301 (2013) 415-23.

[31]   Puli R, Janaki Ram GD. Dynamic recrystallization in friction surfaced austenitic stainless steel coatings, Materials Characterization, 74 (2012) 49-54.

[32]   Vitanov VI, Javaid N, Stephenson DJ. Application of response surface methodology for the optimisation of micro friction surfacing process, Surface and Coatings Technology, 204 (2010) 3501-8.

[33]   Vitanov VI, Voutchkov I, Bedford GM. Decision support system to optimise the Frictec (friction surfacing) process, Journal of Materials Processing Technology, 107 (2000) 236-42.

[34] Rafi HK, Ram GDJ, Phanikumar G, Rao KP. Microstructural evolution during friction surfacing of tool steel H13, Materials & Design, 32 (2011) 82-7.

[35] Govardhan D, Kumar ACS, Murti KGK, Madhusudhan Reddy G. Characterization of austenitic stainless steel friction surfaced deposit over low carbon steel, Materials & Design, 36 (2012) 206-14.

[36] Rafi HK, Ram GDJ, Phanikumar G, Rao KP. Friction surfaced tool steel (H13) coatings on low carbon steel: A study on the effects of process parameters on coating characteristics and integrity, Surface and Coatings Technology, 205 (2010) 232-42.

[37] Hanke S, Fischer A, Beyer M, Dos Santos JF. Reibauftragschweißen von NiAl-Bronze-Verfahren und Materialeigenschaften unter Kavitation, Metall-Forschung, 62 (2009) 587-90.

[38] Gandra J, Pereira D, Miranda RM, Silva RJC, Vilaça P. Deposition of AA6082-T6 over AA2024-T3 by friction surfacing - Mechanical and wear characterization, Surface and Coatings Technology, 223 (2013) 32-40.

[39] Nakama D, Katoh K, Tokisue H. Some Characteristics of AZ31/AZ91 Dissimilar Magnesium Alloy Deposit by Friction Surfacing, Materials Transactions, 49 (2008) 1137-41.

[40] Voutchkov I, Jaworski B, Vitanov VI, Bedford GM. An integrated approach to friction surfacing process optimisation, Surface and Coatings Technology, 141 (2001) 26-33.

[41] Macedo MLK, Pinheiro GA, dos Santos JF, Strohaecker TR. Deposit by friction surfacing and its applications, Welding International, 24 (2010) 422-31.

[42] Gandra J, Miranda RM, Vilaça P. Performance analysis of friction surfacing, Journal of Materials Processing Technology, 212 (2012) 1676-86.

[43] van der Stelt A. Friction Surface Cladding: development of a solid state cladding process, PhD Thesis, Enschede, University of Twente (2014).

[44] Puli R, Janaki Ram GD. Microstructures and properties of friction surfaced coatings in AISI 440C martensitic stainless steel, Surface and Coatings Technology, 207 (2012) 310-8.

[45] Rafi HK, Ram GDJ, Phanikumar G, Rao KP. Friction Surfacing of Austenitic Stainless Steel on Low Carbon Steel: Studies on the Effects of Traverse Speed, Proceedings of the World Congress on Engineering, II (2010).

[46] Pippan R, Hohenwarter A, Scheriau S, Bachmaier A. Nanokristalline Metalle. Neue Werkstoffe aus plastischer Hochverformung, Physik in unserer Zeit, 41 (2010) 23-9.

[47] Goldstein R, Alexandrov S. A new evolution equation for average grain size in processes of severe plastic deformation, Journal of Engineering Mathematics, 78 (2011) 67-81.

[48] Estrin Y, Vinogradov A. Extreme grain refinement by severe plastic deformation: A wealth of challenging science, Acta Materialia, 61 (2013) 782-817.

[49] Hanke S. Microstructural Alterations of Commercial Metallic Alloys by Friction Surfacing, PhD Thesis, Duisburg, Universität Duisburg-Essen (2014).

[50]   Callister WD, Rethwisch DG. Materialwissenschaften und Werkstofftechnik, Weinheim, WILEY-VCH Verlag GmbH & Co. KGaA (2013).

[51]   Dieter JGE. Mechanical Metallurgy, McGraw-Hill Book Company, INC (1961).

[52]   Gottstein G. Physikalische Grundlagen der Materialkunde, Heidelberg, Springer-Verlag (2007).

[53]   Czichos H, Habig KH. Tribologie-Handbuch, Vieweg+Teubner Verlag (2010).

[54]   Steinert R. Einfluss von Randschichtbehandlungen auf das Ermüdungs- und Verschleißverhalten der Titanlegierungen Ti-6Al-4V und Ti-6Al-2Sn-4Zr-6Mo, Dissertation, Aachen, Brandenburgische Technische Universität Cottbus (2012).

[55]   Molinari A, Straffelini G, Tesi B, Bacci T. Dry sliding wear mechanisms of the Ti6Al4V alloy, Wear, 208 (1997) 105-12.

[56]   Qu J, Blau PJ, Watkins TR, Cavin OB, Kulkarni NS. Friction and wear of titanium alloys sliding against metal, polymer, and ceramic counterfaces, Wear, 258 (2005) 1348-56.

[57]   Long M, Rack HJ. Friction and surface behavior of selected titanium alloys during reciprocating-sliding motion, Wear, 249 (2001) 157-67.

[58]   Zum Gahr KH. Microstructure and Wear of Materials, Elsevier Science Publisher B.V. (1987).

[59]   Hager CH, Sanders JH, Sharma S. Characterization of mixed and gross slip fretting wear regimes in Ti6Al4V interfaces at room temperature, Wear, 257 (2004) 167-80.

[60]   Fouvry S, Liskiewicz T, Kapsa P, Hannel S, Sauger E. An energy description of wear mechanism and its applications to oscillating sliding contacts, Wear, 255 (2003) 287-98.

[61]   Bloyce A. Surface engineering of titanium alloys for wear protection, Journal of Engineering Tribology, 212 (1998) 467-76.

[62]   Zimmermann T, Zimmermann M. Lehrbuch der Infrarotthermografie.: Allgemeine Grundlagen der Thermodynamik, Grundlagen der Strahlungsphysik, Infrarot-Geräte-Technologie, Fraunhofer IRB Verlag (2012).

[63]   Kashaev N, Horstmann M, Ventzke V, Riekehr S, Huber N. Comparative study of mechanical properties using standard and micro-specimens of base materials Inconel 625, Inconel 718 and Ti-6Al-4V, Journal of Materials Research and Technology, 2 (2013) 43-7.

[64]   Stickel D. The Influence of Surface Finish on the Localized Dissipation of Frictional Power at Ultra-MildWear, PhD Thesis, Duisburg, Universität Duisburg - Essen (2015).

[65]   Sakai T. Dynamic Recrystallization Microstructure Under Hot Working Conditions, Journal of Materials Processing Technology, 53 (1995) 349-61.

[66]   Momeni A, Abbasi SM. Effect of hot working on flow behavior of Ti–6Al–4V alloy in single phase and two phase regions, Materials & Design, 31 (2010) 3599-604.

[67] Vitanov VI, Voutchkov II. Process parameters selection for friction surfacing applications using intelligent decision support, Journal of Materials Processing Technology, 159 (2005) 27-32.

[68] Esmaily M, Nooshin Mortazavi S, Todehfalah P, Rashidi M. Microstructural characterization and formation of α′ martensite phase in Ti–6Al–4V alloy butt joints produced by friction stir and gas tungsten arc welding processes, Materials & Design, 47 (2013) 143-50.

[69] Buffa G, Fratini L, Schneider M, Merklein M. Effect of Process Parameters on the Joint Integrity in Friction Stir Welding of Ti-6Al-4V Lap Joints, Key Engineering Materials, 554 (2013) 1083-90.

[70] Kitamura K, Fujii H, Iwata Y, Sun YS, Morisada Y. Flexible control of the microstructure and mechanical properties of friction stir welded Ti–6Al–4V joints, Materials & Design, 46 (2013) 348-54.

[71] Liu H, Nakata K, Yamamoto N, Liao J. Grain Orientation and Texture Evolution in Pure Titanium Lap Joint Produced by Friction Stir Welding, Materials Transactions, 51 (2010) 2063-8.

[72] Mironov S, Zhang Y, Sato YS, Kokawa H. Development of grain structure in β-phase field during friction stir welding of Ti–6Al–4V alloy, Scripta Materialia, 59 (2008) 27-30.

[73] Buffa G, Fratini L, Schneider M, Merklein M. Micro and macro mechanical characterization of friction stir welded Ti–6Al–4V lap joints through experiments and numerical simulation, Journal of Materials Processing Technology, 213 (2013) 2312-22.

[74] Lippold JC, Livingston JJ. Microstructure Evolution During Friction Stir Processing and Hot Torsion Simulation of Ti-6Al-4V, Metallurgical and Materials Transactions A, 44 (2013) 3815-25.

[75] Zhang Y, Sato YS, Kokawa H, Park SHC, Hirano S. Microstructural characteristics and mechanical properties of Ti–6Al–4V friction stir welds, Materials Science and Engineering: A, 485 (2008) 448-55.

[76] Mishra RS, Kumar PSN. Friction Stir Welding and Processing, Springer (2014).

[77] Buffa G, Ducato A, Fratini L. FEM based prediction of phase transformations during Friction Stir Welding of Ti6Al4V titanium alloy, Materials Science and Engineering: A, 581 (2013) 56-65.

[78] Chen CC, Coyne JE. Deformation Characteristics of Ti-6AI-4V Alloy Under Isothermal Forging Conditions, Metallurgical Transactions A, 7A (1976) 1931-76.

[79] Mishra RS, Mahoney MW. Friction Stir Welding and Processing, Springer (2007).

[80] Rao KP, Damodaram R, Rafi HK, Ram GDJ, Reddy GM, Nagalakshmi R. Friction surfaced Stellite6 coatings, Materials Characterization, 70 (2012) 111-6.

[81] Hanke S, Beyer M, dos Santos JF, Fischer A. Friction surfacing of a cold work tool steel-Microstructure and sliding wear behavior, Wear, 308 (2013) 180-5.

[82] Barnes SJ, Bhatti AR, Steuwer A, Johnson R, Altenkirch J, Withers PJ. Friction Stir Welding in HSLA-65 Steel: Part I. Influence of Weld Speed and Tool Material on

Microstructural Development, Metallurgical and Materials Transactions A, 43 (2012) 2342-55.

[83]   Seshacharyulu T, Medeiros SC, Frazier WG, Prasad YVRK. Microstructural mechanisms during hot working of commercial grade Ti-6Al-4V with lamellar starting structure, Materials Science and Engineering A, 325 (2002) 112-25.

[84]   Rosen RS, Paddon SP, Kassner ME. The variation of the yield stress of Ti alloys with strain rate at high temperatures, Journal of Materials Engineering and Performance, 8 (1999) 361-7.

[85]   Park NK, Yeom JT, Na YS. Characterization of deformation stability in hot forging of conventional Ti-6Al-4V using processing maps, Journal of Materials Processing Technology, 130 (2002) 540-5.

[86]   Meyers MA, Subhash G, Kad BK, Prasad L. Evolution of microstructure and shear-band formation in α-hcp titanium, Mechanics of Materials, 17 (1993) 175-93.

[87]   Prasad Rao K, Veera Sreenu A, Khalid Rafi H, Libin MN, Balasubramaniam K. Tool steel and copper coatings by friction surfacing – A thermography study, Journal of Materials Processing Technology, 212 (2012) 402-7.

[88]   Krohn H, Hanke S, Beyer M, dos Santos JF. Influence of external cooling configuration on friction surfacing of AA6082 T6 over AA2024 T351, Manufacturing Letters, 5 (2015) 17-20.

[89]   Donachie MJ. Titanium A Technical Guide, ASM International (2000).

[90]   Humphreys FJ, Hatherly M. Recrystallization and Related Annealing Phenomena, Elsevier Ltd. (2004).

[91]   Bachmaier A, Hafok M, Schuster R, Pippan R. Limitations in the Refinement by Severe Plastic Deformation: The Effect of Processing, Reviews on Advanced Materials Science, 25, 16-22 (2010).

[92]   Tan MJ, Zhu XJ. Microstructure evolution of CP titanium during high temperature deformation, Archives of Materials Science and Engineering, 28 (2007) 5-11.

[93]   Gey N, Humbert M. Specific analysis of EBSD data to study the texture inheritance due to the β→α phase transformation, Journal of Materials Science, 38 (2003) 1289-94.

[94]   Glavicic MG, Kobrun PA, Bieler TR, Semiatin SL. A method to determine the orientation of the high-temperature beta phase from measured EBSD data for the low-temperature alpha phase in Ti-6Al-4V, Materials Science and Engineering A, 346 (2003) 50-9.

[95]   Gey N, Humbert M. Characterization of the variant selection occurring during the alpha ->beta ->alpha phase transformations of a cold rolled titanium sheet, Acta Materialia, 50 (2002) 277-87.

[96]   Gil FJ, Planell JA. Growth Order and Activation Energies for Grain Growth of Ti-6Al-4V Alloys in ß Phase, Scripta Metallurgica et Materialia, 25 (1991) 2843-48.

[97]   Wanjara P, Jahazi M. Linear Friction Welding of Ti-6Al-4V: Processing, Microstructure, and Mechanical-Property Inter-Relationships, Metallurgical and materials transactions A, 36 (2004) 2149-64.

[98] Honarmandi P, Aghaie-Khafri M. Hot Deformation Behavior of Ti–6Al–4V Alloy in β Phase Field and Low Strain Rate, Metallography, Microstructure, and Analysis, 2 (2012) 13-20.

[99] Lee Y-L. Microstructure Evolution of Metals through Thermo-Mechanical Process (TMP), Mechanical Property of TMP Samples, and small Scale Test Samples, PhD Thesis, Michigan, The University of Michigan (2010).

[100] Abouridouane M. Bruchverhalten von Leichtmetallen unter Impact-Beanspruchung, Dissertation, Aachen, Rheinisch-Westfälische Technische Hochschule Aachen (2005).

[101] Dew-Hughes D, Robertson WD. The Mechanism of Hardening in Aged Aluminum-Copper Alloys, Acta Metallurgica, 8 (1960) 156-67.

[102] Molinari A, Musquar C, Sutter G. Adiabatic shear banding in high speed machining of Ti-6Al-4V: experiments and modeling, International Journal of Plasticity, 18 (2002) 443-59.

[103] Rittel D, Landau P, Venkert A. Dynamic recrystallization as a potential cause for adiabatic shear failure, Physical Review Letters, 101 (2008) 1-4.

[104] Pilchak AL, Williams JC. Microstructure and Texture Evolution during Friction Stir Processing of Fully Lamellar Ti-6Al-4V, Metallurgical and Materials Transactions A, 42 (2010) 773-94.

[105] Ding R, Guo ZX, Wilson A. Microstructural evolution of a Ti–6Al–4V alloy during thermomechanical processing, Materials Science and Engineering A, A327 (2002) 233-45.

[106] Valiev RZ, Alexandrov IV, Zhu YT, Lowe TC. Paradox of strength and ductility in metals processed by severe plastic deformation, Materials Research, 17 (2002) 5-8.

[107] Parker ER. Materials Data Book for Engineers and Scientists, New York, McGraw-Hill (1967).

[108] Brandes EA, Brook GB. Smithells Metals Reference Book, Butterworth-Heinemann (1992).

[109] Gunderov DV, Polyakov AV, Semenova IP, Raab GI, Churakova AA, Gimaltdinova EI, et al. Evolution of microstructure, macrotexture and mechanical properties of commercially pure Ti during ECAP-conform processing and drawing, Materials Science and Engineering: A, 562 (2013) 128-36.

[110] Semenova IP, Saitova LR, Raab GI, Korshunov A, Zhu YT, Lowe TC, et al. Microstructural Features and Mechanical Properties of the Ti-6Al-4V ELI Alloy Processed by Severe Plastic Deformation, Materials Science Forum, 503 (2006) 757-62.

[111] Hertz H. Über die Berührung fester elastischer Körper, Journal für die reine und angewandte Mathematik, 92 (1881) 156-71.

[112] Blanchard P, Colombie C, Pellerin V, Fayeulle S, Vincent L. Material Effects in Fretting Wear: Application to Iron, Titanium, and Aluminum Alloys, Metallurgical Transactions A, 22A (1990) 1535-44.

[113]   Pearson SR, Shipway PH. Is the wear coefficient dependent upon slip amplitude in fretting? Vingsbo and Söderberg revisited, Wear, 330-331 (2015) 93-102.

[114]   Bill RC. Fretting wear in titanium, monel-400, and cobalt-25 percent molybdenium using scanning electron microscopy, NASA Tech. Note TN D-6660, (National Aeronautics and Space Administration) (1972).

[115]   Bill RC. Selected Fretting-Wear-Resistant Coatings for Ti-6%Al-4%V Alloy, Wear, 106 (1985) 283-301.

[116]   Gardos MN. Magn´eli phases of anion-deficient rutile as lubricious oxides. Part I. Tribological behavior of single-crystal and polycrystalline rutile, Tribology Letters, 8 (2000) 65-78.

[117]   Gardos MN. Magn´eli phases of anion-deficient rutile as lubricious oxides. Part II. Tribological behavior of Cu-doped polycrystalline rutile, Tribology Letters, 8 (2000) 79-96.

[118]   Erdemir A. A crystal-chemical approach to lubrication by solid oxides, Tribology Letters, 8 (2000) 97-102.